ABSTRACT

Title of Dissertation: DEVELOPMENT OF LI^+ AND NA^+ CONDUCTING CERAMICS AND CERAMIC STRUCTURES FOR USE IN SOLID STATE BATTERIES

Gregory Hitz, Doctor of Philosophy, 2016

Dissertation directed by: Professor Eric Wachsman,
Department of Materials Science & Engineering

A solid state lithium metal battery based on a lithium garnet material was developed, constructed and tested. Specifically, a porous-dense-porous trilayer structure was fabricated by tape casting, a roll-to-roll technique conducive to high volume manufacturing. The high density and thin center layer (< 20 μm) effectively blocks dendrites even over hundreds of cycles. The microstructured porous layers, serving as electrode supports, are demonstrated to increase the interfacial surface area available to the electrodes and increase cathode loading. Reproducibility of flat, well sintered ceramics was achieved with consistent powderbed lattice parameter and ball milling of powderbed. Together, the resistance of the LLCZN trilayer was measured at an average of 7.6 ohm-cm^2 in a symmetric lithium cell, significantly lower than any other reported literature results. Building on these results, a full cell with a lithium metal anode, LLCZN trilayer electrolyte, and $LiCoO_2$ cathode was cycled 100 cycles without decay and an average ASR of 117 ohm-cm^2. After cycling, the cell was held

at open circuit for 24 hours without any voltage fade, demonstrating the absence of a dendrite or short-circuit of any type. Cost calculations guided the optimization of a trilayer structure predicted that resulting cells will be highly competitive in the marketplace as intrinsically safe lithium batteries with energy densities greater than 300 Wh/kg and 1000 Wh/L for under $100/kWh. Also in the pursuit of solid state batteries, an improved Na^+ superionic conductor (NASICON) composition, $Na_3Zr_2Si_2PO_{12}$, was developed with a conductivity of $1.9x10^{-3}$ S/cm. New super-lithiated lithium garnet compositions, $Li_{7.06}La_3Zr_{1.94}Y_{0.06}O_{12}$ and $Li_{7.16}La_3Zr_{1.84}Y_{0.16}O_{12}$, were developed and studied revealing insights about the mechanisms of conductivity in lithium garnets.

DEVELOPMENT OF NA^+ AND LI^+ CONDUCTING CERAMICS AND CERAMIC STRUCTURES FOR USE IN SOLID STATE BATTERIES

By

Gregory Thomas Hitz

Dissertation submitted to the Faculty of the Graduate School of the
University of Maryland, College Park, in partial fulfillment
of the requirements for the degree of
Doctor of Philosophy
2016

Advisory Committee:
Professor Eric Wachsman, Chair
Professor Liangbing Hu
Professor Isabel Lloyd
Professor Yifei Mo
Professor Peter Chung, Dean's Representative

Acknowledgements

The work in this document is representative of years of guidance, love and support from everyone in my life. I owe all my success to my family who encouraged me to pursue my kindergarten passion to be “an inventor.” They gave me a healthy approach to life and work and insisted I follow my dreams.

I’ll be forever grateful to Dr. Wachsman for supporting me through my PhD. He taught me that every ounce of effort is worthwhile when presenting my research. He is my role model for how to frame the work I’ve done, both in how I share it with others and how I think about it myself.

Dr. Thangadurai taught me what it means to be a scientist. His incredible energy and love for materials development inspired me. His work gave the world the material that serves as the basis for most of the work in this dissertation. I’ll also always remember the pride I felt the first time I indexed a lattice with his support using PROSZKI.

Dr. Hu always brought a smile to my face, pushed me to work harder on the battery and made sure we didn’t miss an opportunity to use carbon nanotubes. I’m thankful for his guidance on the ins and outs of batteries and teaching me his methods for publishing in top journals.

I would like to thank my committee for supporting me through this process. Thank you to Dr. Wachsman, Dr. Hu, Dr. Lloyd, Dr. Mo, and Dr. Chung.

Ashley Ruth and Kang Taek Lee spent countless hours teaching me what I needed to know to function in lab. They taught me about ball milling, calcining,

sintering, impedance measurement, and generally introduced me to the life of a ceramist.

I want to especially thank Kathleen Hart who earns her title every day as an "MSE grad student's best friend." It's because of her I was able to hit deadlines, meet my departmental requirements and survive as a grad student.

I'm thankful for the entire UMERC solid state battery team: Dennis McOwen, Yang Wen, Yunhui Gong, Xiaogang Han, Jiaqi Dai, Chengwei Wang, Kun Fu, Boyang Liu, Matthew Limpert, and Tanner Hamann. They put in long hours, believed in our vision, and made our team successful.

My other labmates were always there to discuss ideas, give advice and share the experience. Thank you to Colin Gore, Chris Pellegrinelli, Tom Hays, Mann Sakbodin, Adam Jolley, Yi-Lin Huang, Gil Cohn, Hussain Abdul Jabbar, Abhishek Jaiswal, Alireza Pesaran, Patrick Stanley, and Albert Painter.

Lastly, I want to thank Colleen Doyle, my best friend and fiancée for her love, support and incredible patience. She made sure every part of my life outside of work was amazing. She picked me up from work on the very late nights, organized events for when I did have free time, and took care of our dog, amongst 1,000 other things. She cares enough about me to know more about batteries than any other occupational therapist in the world. She is one of the biggest reasons I always push to be the best that I can be.

Table of Contents

List of Tables

List of Figures

Chapter 1: Introduction and Background

1.1 - Battery applications & technology

Rapidly growing markets for renewable energy, electric vehicles and personal electronic devices have driven an urgent need for better and less expensive energy storage technologies. Sales of electric vehicles (EV) in the United States grew an average of 85% per year from 2011 to 2014[1]. Wind and solar power are reaching high enough market penetration in many countries to risk destabilizing the grid without grid-attached storage[2,3]. Many applications in these markets are served by lithium ion batteries. Nearly all electric vehicles are powered with lithium ion batteries. Forbes predicts that by 2019, more than 800 MW of home battery system is intended for mass market sales. Lithium ion batteries have become an important part of society's interaction with technology, a trend which looks likely to continue.

Commercially released by Sony in 1991, lithium ion batteries represent the highest energy density batteries currently available as shown in Figure 1a[4–7]. Most lithium ion batteries consist of a metal oxide cathode, liquid organic electrolyte and a graphite intercalation anode. This provides a strong electrochemical gradient, and therefore high charged voltage of 3-5 V depending upon cathode, when the graphite is fully lithiated[3]. As depicted in Figure 1b, when an electronic load is connected, the circuit is completed and lithium ions leave the anode and move through the lithium ion conductive electrolyte to the cathode to balance the charges to the removed electrons[8]. Based on this general structure and chemistry, great strides have been made in capacity and voltage. Much of this improvement has been in the development of new cathode chemistries, such as $LiCoO_2$ (LCO), $LiNi_{1/3}Mn_{1/3}Co_{1/3}O_2$ (NMC),

$LiNi_{0.8}Co_{0.15}Al_{0.05}O_2$ (NCA), and $LiFePO_4$ (LFP)[7].

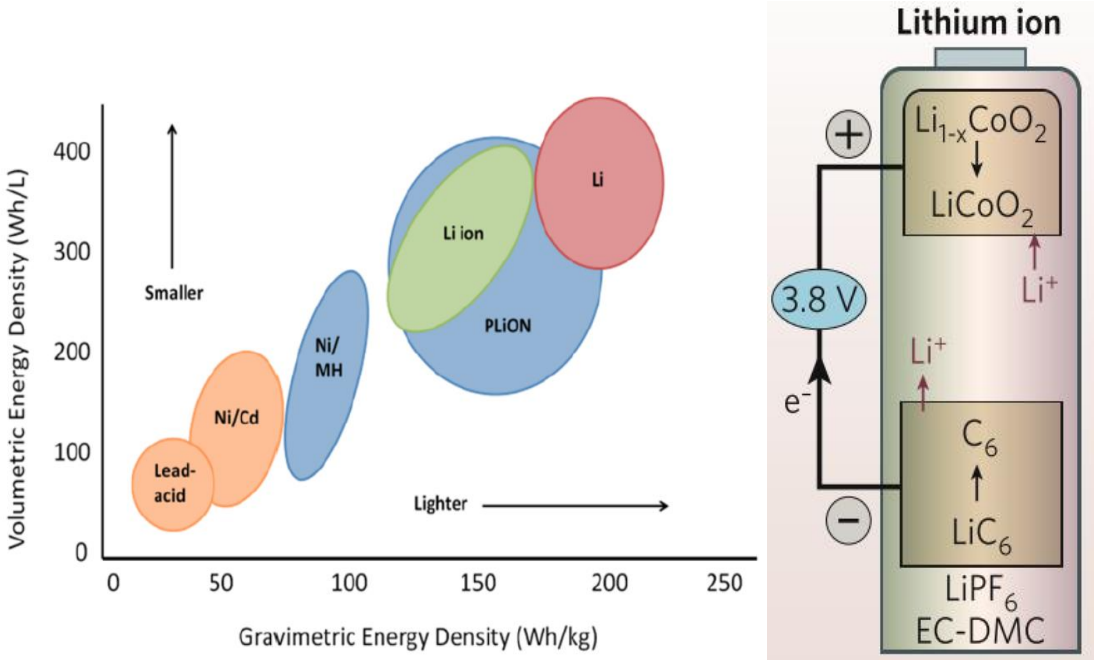

Figure 1. (a) Plot of energy densities of various battery technologies replotted from ref. 6 (b) Conceptual diagram of a lithium ion battery from ref. 8.

Despite the success of lithium ion batteries, there are several important applications which are limited by the poor safety, high cost and inadequate energy density of today's technology[9–11]. Recently released electric vehicles contain thousands of lithium ion cells and occasionally cause fires despite heavy shielding[12]. Depending on mission, soldiers need anywhere from 20-50 pounds of batteries which must be protected from shorting and hot environments to avoid a fire[13]. Grid scale storage requires costs below $100/kWh and a cycle life of at least 5,000 cycles[14], whereas current state-of-the-art manufacturing methods aim to break $200/kWh and 1,000 cycles.

Many of these limitations stem from the liquid organic electrolytes which are

flammable and unstable[5]. Organic electrolytes are commonly based on $LiPF_6$ as the ion shuttle and some carbonate such as ethylene carbonate (EC) or dimethyl carbonate (DMC) as the solvent[15–17]. Safety concerns are due to the highly flammable electrolyte, which can become explosive when vaporized due to overheating. This chemistry prevents the use of some very promising cathodes and limits the cycle life of others, because the liquid allows dissolution and diffusion of electrodes. Manganese has been shown to dissolve into carbonate-based electrolytes, causing cathode degradation when using high voltage spinel cathodes which usually contain manganese[18]. The use of sulfur cathodes would increase specific energy by ~4x at a fraction of the cost of current cathodes, but is not possible due to the high solubility of polysulfide compounds in carbonate electrolytes[19].

Another drawback related to the liquid electrolyte is an inability to use metallic lithium anodes. Energy density could be greatly increased by using a lithium metal anode, which has a capacity of 3860 mAh/g, instead of a graphite anode, which has a capacity of 372 mAh/g. As seen in Figure 1a, this would increase the volumetric and gravimetric energy density compared to current lithium ion batteries. However, a lithium metal anode in current designs would allow the formation of long fractal-like growths of lithium metal called "dendrites" through the electrolyte which would short the electrodes[5,7,8] and cause a fire.

1.2 - Promise of solid state batteries

Solid state electrolytes (SSE's) present a solution to these problems[20]. SSE's are ionically conductive solids which can be used to shuttle ions between anode and

cathode. Many SSE's are inherently non-flammable, strong enough to prevent dendrite formation, and some are stable to metallic lithium[21]. Solid state batteries provide the opportunity to completely redesign the battery, enabling safe, high energy density cells incorporating lithium metal anodes.

The simplest and most common design of a solid state battery is shown in Figure 2. This is a simple planar structure with an electrolyte in between two electrodes and current collectors. This design generally lends itself to very thin cells, with reports of areal capacity[22] in the low range of 10-100 $\mu Ah/cm^2$. In this case, the solid electrolyte separates the electrodes, preventing short circuits and diffusion of the electrodes. This configuration with a dense solid electrolyte opens the possibility of using a sulfur cathode, lithium anode, or high voltage spinels, as long as the electrolyte material chosen is stable in those conditions.

Figure 2. Diagram of a planar solid state battery from ref. 22.

An Arrhenius plot comparing the conductivities of several common solid electrolytes, as well as a traditional liquid organic electrolyte, is shown in Figure 3. The conductivity of solid electrolytes has recently been approaching that of liquid electrolytes, though more work is required to reach parity. The most conductive of the current solid electrolytes are $Li_7La_3Zr_2O_{12}$ (lithium garnet) and Li-β-Al_2O_3, though

Li-β-Al_2O_3 is significantly more sensitive to impurities due to its 2D conduction pathways.

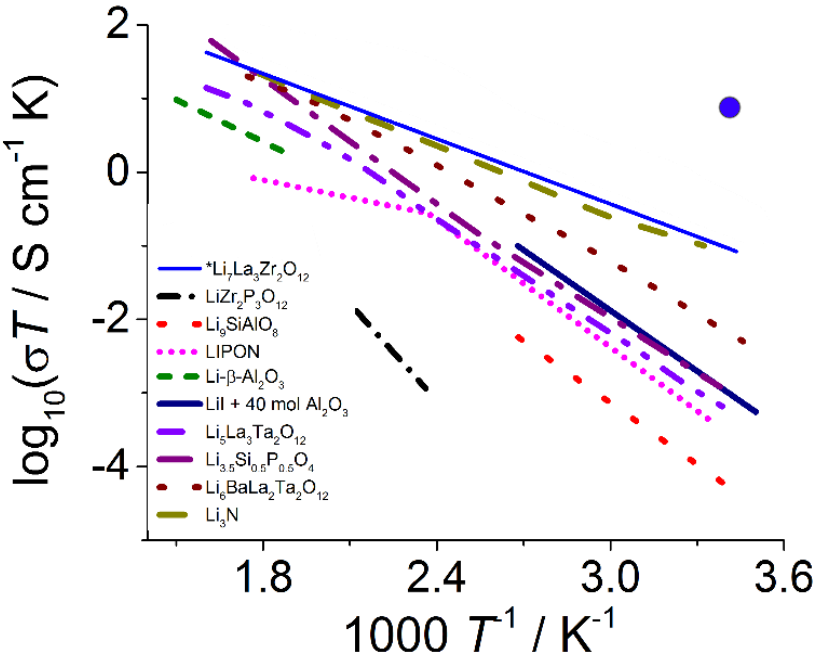

Figure 3. Arrhenius plot of various solid electrolytes and 1 M $LiPF_6$ in EC-PC (blue circle), replotted from ref. 21.

1.3 - Lithium garnet development

Lithium garnets are one of the most promising classes of SSE's. Lithium-ion conducting garnets were discovered in 2003 by Venkataraman Thangadurai, Heiko Kaack, and Werner Weppner. Based on the parent composition, $Li_7La_3Zr_2O_{12}$ (LLZ), lithium garnets are high conductivity, stable to lithium metal and can be synthesized and used to fabricate cells with economic, scalable techniques[21,23–25]. The high conductivity lithium garnet phase is a cubic lattice of space group $Ia\underline{3}d$ with many lithium sites which leads to high Li^+ mobility through the lattice. A rendering of this crystal structure is drawn with VESTA[26] in Figure 4. The lithium sites shown in

yellow are short ion-hopping distances apart and have 3-dimensional pathways with large openings between ZrO_6 and LaO_8 polyhedral groups. This creates high mobility pathways for the lithium ions, leading to outstanding conductivity.

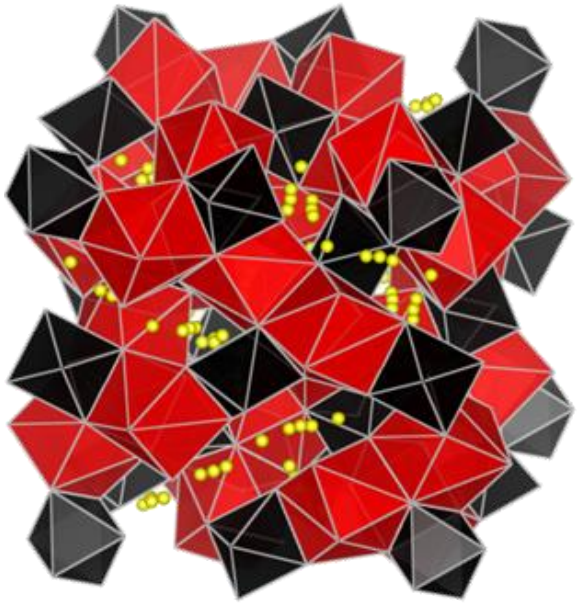

Figure 4. Drawing of lithium garnet unit cell, showing lithium sites (yellow spheres), ZrO_6 octahedra (black) and LaO_8 (red).

As shown in Figure 3, the conductivity of cubic garnet LLZ surpasses that of most SSE's and nearly rivals that of organic electrolytes. As shown in Figure 5, lithium garnet can also crystallize in a much lower conductivity tetragonal phase. It is not entirely understood why cubic phase forms versus tetragonal. Stabilization of the high conductivity cubic phase has been linked to higher calcining temperatures and aluminum contamination from crucibles[27–29]. The inset shows a representative X-Ray diffraction pattern of cubic lithium garnet.

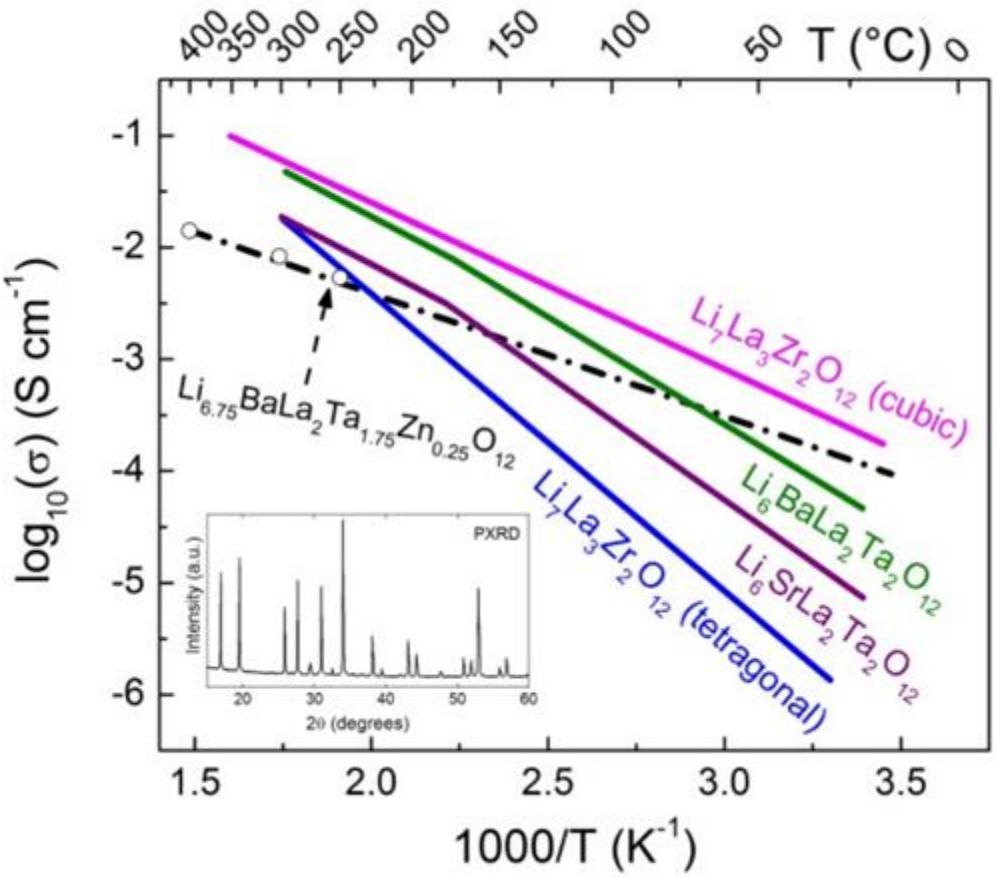

Figure 5. Ionic conductivity of Li-garnets developed by Thangadurai and co-workers with Li7-garnet data extracted from ref. 21.

Maintaining high conductivity in garnet is also linked to specific lithium content. Figure 6 shows an analysis of data published by Goodenough[25,30] which links lithium occupancy of each site to bulk conductivity of the material. As total lithium content is increased through doping, lithium moves from the tetrahedral site to the octahedral site, causing a peak conductivity at around 6.4 lithium atoms per formula unit.

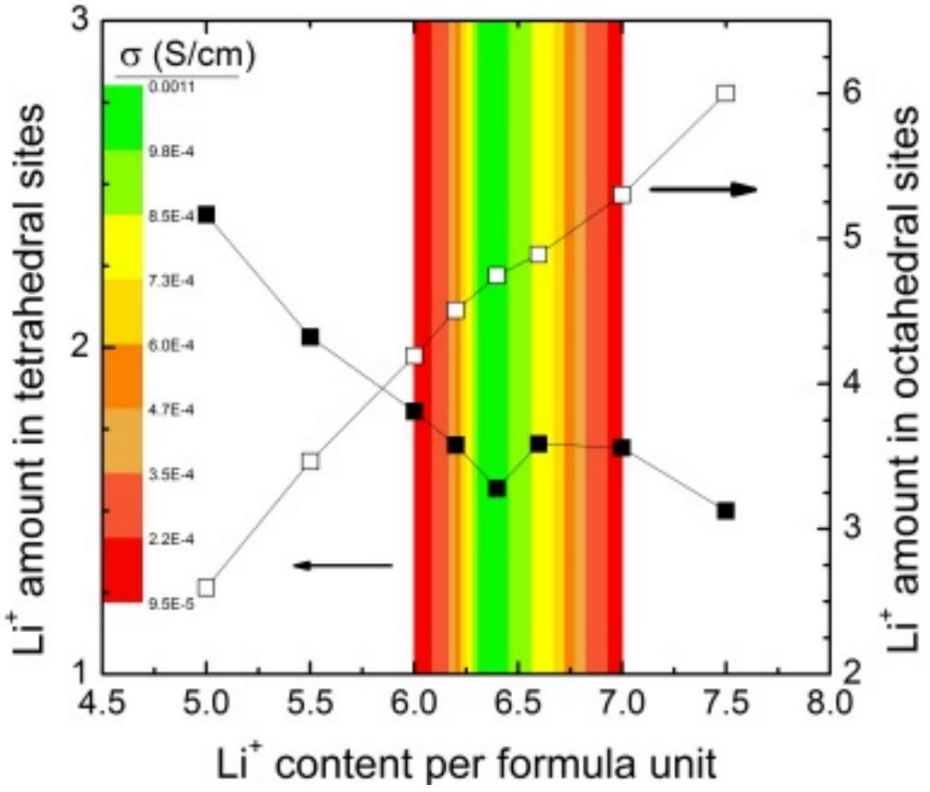

Figure 6. Effect of Li^+ site occupancy on conductivity with data extracted from refs. 25 and 30.

LLZ has nearly no electronic conductivity and is stable to high voltages, beyond the voltage of any known cathodes. This is demonstrated with a cyclic voltammetry curve in Figure 7, showing no current passing through a garnet pellet up

to 7 volts[30]. The high stability helps increase compatibility with cathodes and stability to lithium metal.

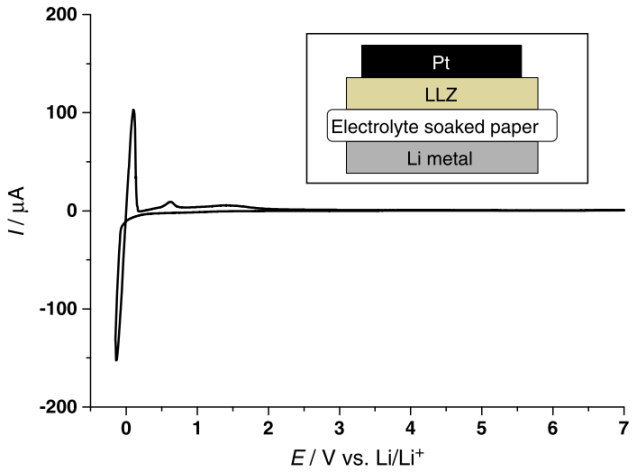

Figure 7. Cyclic voltammetry of LLZ from ref. 30.

1.4 - Solid state sodium batteries

Solid state technology can also be extended to chemistries beyond lithium. There is significant interest in non-lithium chemistries due to the high price of lithium[31] ($66/kg as of March 2015) and the concern that lithium resources will not be enough to meet the need of the rapidly expanding lithium battery market. Lithium-containing battery materials can instead be made with other alkaline or even alkaline earth metals such as sodium, potassium, and magnesium. Much recent work has been directed towards sodium batteries due to the high availability and low cost of sodium[31] ($3/kg as of March 2015). This could dramatically decrease cell costs, as around 49% of the cell cost for a lithium ion battery is materials cost (Figure 8)[32].

This significantly less expensive cell would be ideal for grid storage or any application where cost is paramount.

Figure 8. BatPaC model for lithium ion battery cost breakdown from ref. 32.

These batteries operate on the same principles as lithium batteries, though they sacrifice some voltage due to the weaker metal oxide bonding strength. A comparison between voltages of otherwise identical cathode materials reveals about a 0.53 volt decrease with sodium versus lithium[33], as shown in Figure 9. Specific capacity is also sacrificed due to the larger sodium ion. For example, the theoretical energy density of $LiCoO_2$ is 140 mAh/g whereas that of $NaCoO_2$ is only 120 mAh/g due only to the change in mass of alkaline ion. On the anode side, sodium metal has a specific capacity of 1166 mAh/g, compared to lithium metal's 3860 mAh/g.

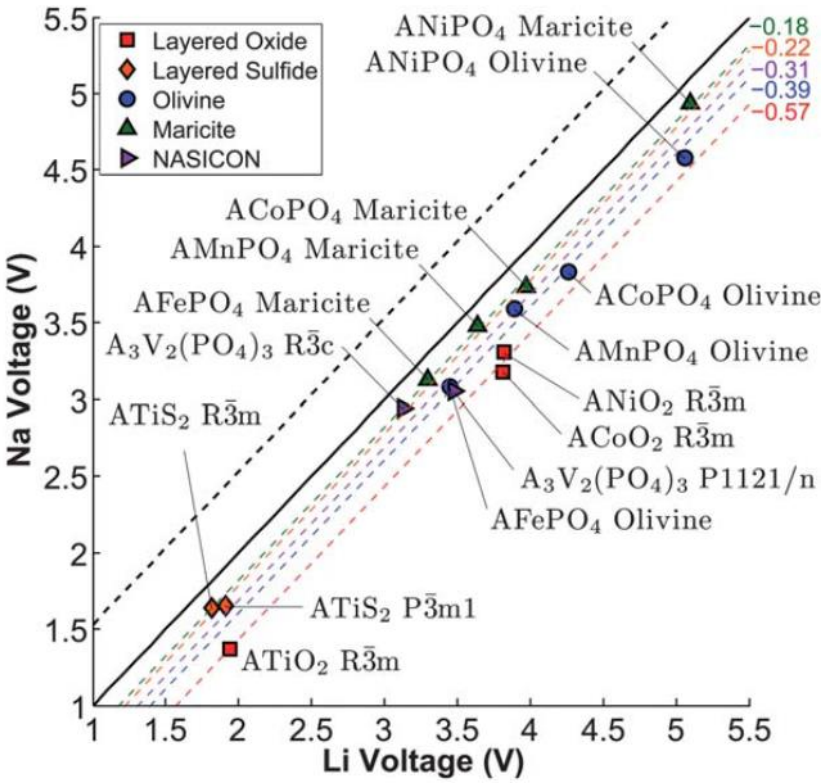

Figure 9. Plot of cathode voltage vs. metal with either sodium or lithium as alkaline component from ref 33.

The conductivity of solid state sodium ion conductors is equivalent to or better than the conductivity of solid state lithium ion conductors. This may be due to the weaker Na-O bond than Li-O bond, which allows Na^+ ions to move more freely. Figure 10 shows a summary chart of two of the top Na^+ conductors, Na-β-Al_2O_3 and Na+ superionic conductor (NASICON) compared to gel and polymer electrolytes[34]. While single crystal Na-β-Al_2O_3 has the highest bulk conductivity, commercial fabrication of single crystals is expensive and not suitable for inexpensive scalable manufacturing. Therefore, it can be seen that NASICON is the best material for a practical room temperature solid state battery.

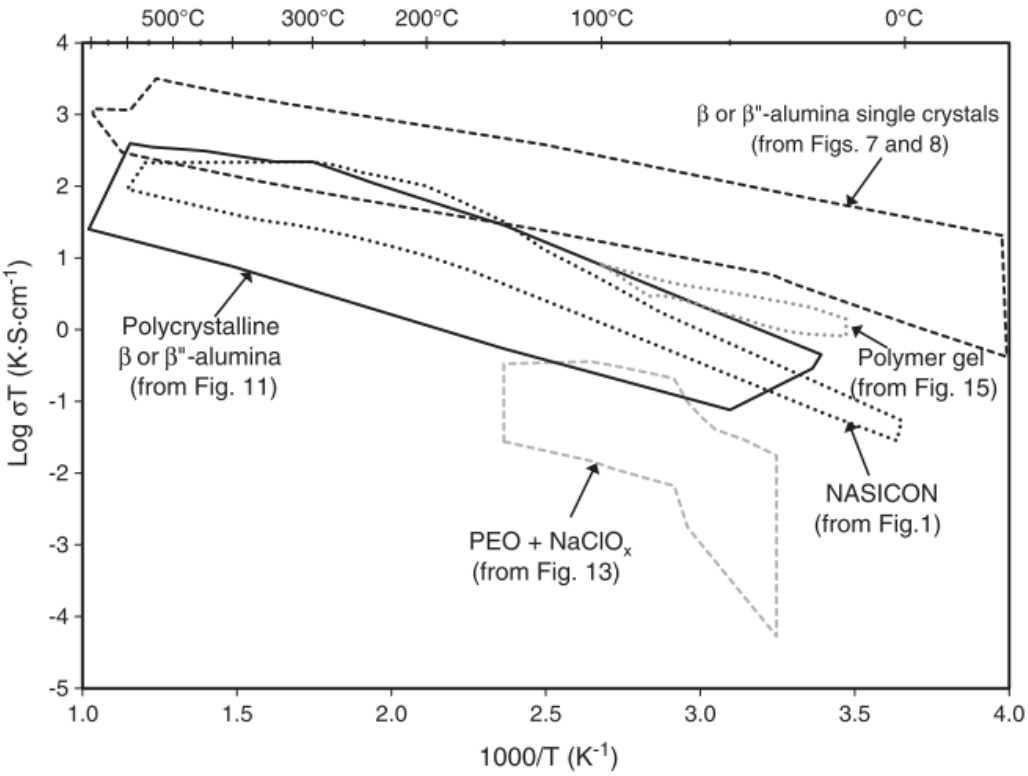

Figure 10. Arrhenius plot of various Na+ conductors from ref. 34.

1.5 - NASICON development

NASICON was developed in 1976 by Drs. Hong, Kafalas and Goodenough as an attempt to improve on the fast Na^+ transport of Na-β-Al_2O_3, with the chemical composition of $Na_{1+x}Zr_2Si_xP_{3-x}O_{12}$ chosen because zirconium oxides are not reduced by molten sodium[35,36]. The most conductive member of this family is the x=2 member, $Na_3Zr_2Si_2PO_{12}$, which crystallizes in the monoclinic phase at room temperature and has a phase transition to a lower activation energy rhombohedral phase at around 160 ºC[37,38]. Figure 11 below shows a diagram of the crystal structure of this high temperature rhombohedral phase[5].

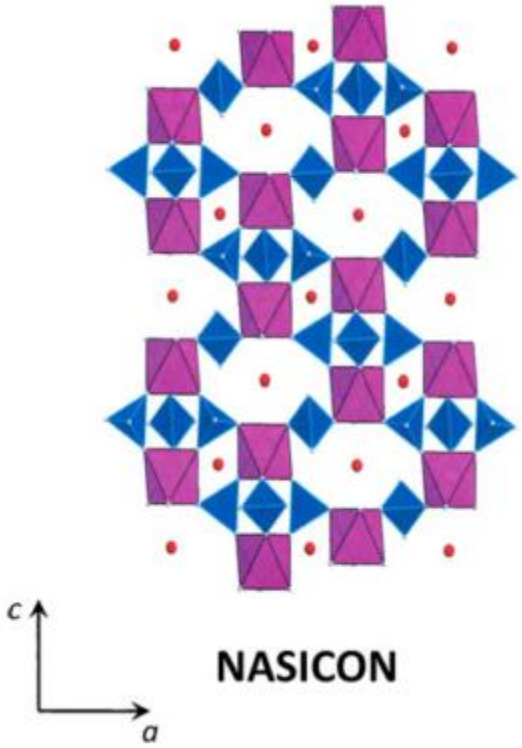

Figure 11. Drawing of rhombohedral NASICON structure from ref. 5.

Significant work has since focused on improving the conductivity of NASICON[39–44]. As shown in Figure 12a, many studies have doped the Zr-site with other elements in order to change the local site potentials around the main conduction path shown in Figure 12b. The base composition of this study, $Na_{1.5}M_{0.5}Zr_{1.5}(PO_4)_3$, as well as the materials used for many other studies of NASICON doping use a silicon-free NASICON with significantly lower conductivity than the originally discovered NASICON. This helps simplify the system for studies to discover valuable information about the effects of changes to the lattice. However, less information is available about how doping affects the $Na_3Zr_2Si_2PO_{12}$ lattice. Zr-site doping on the silicon-free member consistently produces higher conductivity than the base

composition, though it normally produces conductivity just below that of the high conductivity $Na_3Zr_2Si_2PO_{12}$.

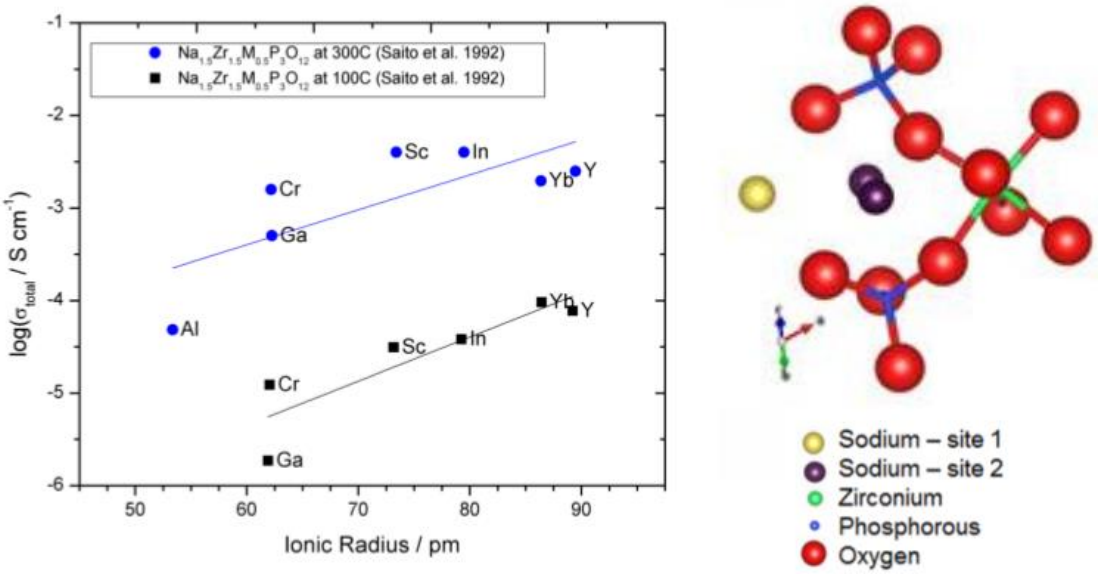

Figure 12. Doping of Zr-site on $Na_{1.5}M_{0.5}Zr_{1.5}(PO_4)_3$ showing (a) conductivity vs ionic radius of dopant at 100 ºC (black) and 300 ºC (blue) replotted from ref. 45 and (b) VESTA drawing of majority lithium conductivity pathway.

Attempts to fabricate solid state batteries based on NASICON electrolytes usually use the NASICON-structured $Na_3V_2(PO_4)_3$ (NVP) as cathode and anode due to its two voltage plateaus at 1.6 V and 3.4 V[46–48]. The selection of NVP is likely to increase chemical compatibility and decrease interfacial resistance with the NASICON electrolyte. More work is necessary to prove the potential of NASICON in room temperature solid state sodium batteries, as there are only several reported attempts in literature.

1.6 - Shortcomings of solid state batteries

Solid state batteries represent a promising future for batteries and electrolyte development has produced highly conductive materials with competitive

performance. However, further development is necessary to produce market-ready batteries due to performance, cost and cycle life limitations of current solid state battery designs.

Solid state electrolytes have shown improvements in conductivity but are still an order of magnitude lower conductivity than liquid electrolytes. All else equal, lower conductivity leads to a higher area specific resistance (ASR) which limits the maximum practical current density, ultimately limiting the output power of the battery. This necessitates design decisions to compensate for the low conductivity and allow high performance.

Another major contributor to ASR in solid state batteries is interfacial resistance between electrode and electrolyte[49,50]. This resistance can be orders of magnitude higher than the bulk resistance of the electrolyte. Figure 13 shows a Nyquist plot of electrochemical impedance data for two lithium garnet pellets with lithium metal electrodes on either side[49]. The first arc represents bulk resistance and the second arc represents a large interfacial resistance. In lithium garnet, this is in part due to a lithium carbonate layer which forms in air and prevents lithium wetting, decreasing actual interfacial contact area[50]. There are efforts to prevent this interfacial impedance such as the authors in Figure 13 did by polishing the surface in argon before wetting with lithium. A more recent effort has drastically decreased the interfacial resistance by applying an Al_2O_3 coating using atomic layer deposition to prevent carbonate formation[50]. Regardless, this is a concern which must be considered when developing solid state batteries.

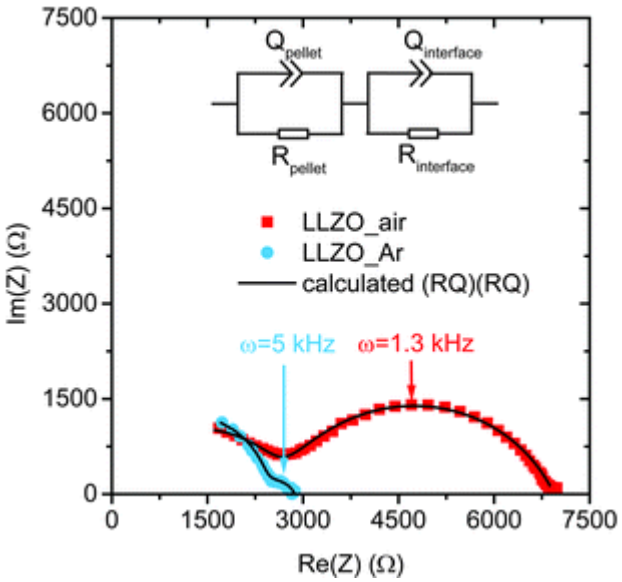

Figure 13. Nyquist plot of electrochemical impedance of lithium garnet pellets with lithium metal electrodes prepared in air (red) or argon (blue) from ref. 49.

Solid state batteries have been shown to allow dendrite penetration through the dense solid electrolyte separator layer at high current densities when using a lithium metal anode. For lithium garnet, some[51–53] have put this limit at around 50-100 μA/cm^2, which is too low for many battery applications. This is likely a function of poor lithium wetting causing point contact between electrode and electrolyte, causing incredibly high currents and resulting fields through the point contacts. A recent study[50] has shown dendrite-free cycling at up to 300 μA/cm^2 by improving lithium wetting, which indicates that actual interfacial current density is more important than external current density. If this is true, external current density can be increased by designing structures to increase electrode-electrolyte interfacial surface area per projected cell area.

A major drawback to existing solid state batteries is their extremely low cathode loading. In a planar configuration, cathode loading must be low to allow short conduction paths for ions and electrons. Ions from the electrolyte and electrons from the current collector enter the electrode from opposite sides. Redox reactions can only happen when both the electron and ion meet within the cathode, which tends to be a poor conductor of ions and electrons. A thick cathode would create high resistance, necessitating that the cathode be very thin. As mentioned previously, solid state batteries in this configuration generally have cathode loadings on the order of 10-100 $\mu Ah/cm^2$ compared to traditional commercial cells which are 1-3 mAh/cm^2. Solid state cells can be wired together to increase the system capacity, but increasing the number of cells produced like this dramatically increases manufacturing and packaging costs. A new solid state cell design is likely required to bring solid state batteries to a point of commercial viability.

Cell designs intended to increase cathode loading and decrease ASR have been developed[22], as demonstrated in Figure 14. However, many of these designs rely on deposition-on-substrate techniques to produce such structures, which is expensive and produces cells with low energy density once the substrate considered. For solid state batteries to achieve meaningful traction, structures must be developed which can be fabricated both scalably and without a substrate.

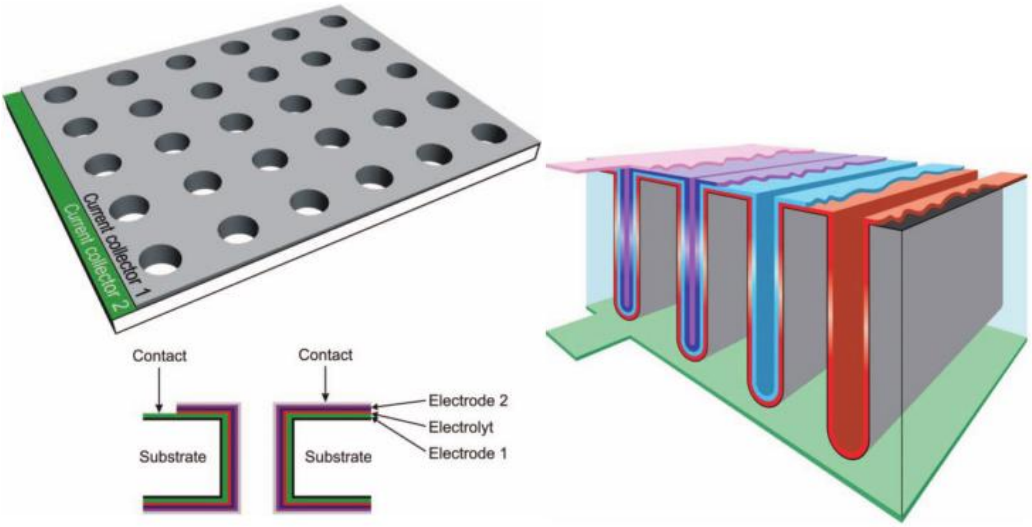

Figure 14. Various 3D solid state battery designs from ref. 22.

Chapter 2: Development of Higher Conductivity NASICON

2.1 - Introduction

The development of high voltage, high power, and low cost electrochemical batteries will help to catalyze the coming renewable energy revolution. Renewable energy sources such as wind and solar power promise clean, unlimited power. However, the transient nature of wind and sun increases the difficulty of implementing these solutions. Inexpensive, high performance grid-scale batteries could load level inconsistent energy production, delivering power as needed and cost-effectively integrating renewables into the grid.

Sodium-ion batteries offer a significantly lower cost alternative to the more prevalent lithium-ion batteries[10,54]. Moreover, conventional lithium-ion batteries suffer drawbacks due to their organic liquid electrolyte, including dissolution of electrodes into the electrolyte and complex decomposition side-reactions with the electrodes, which cause the degradation of the battery performance[16,17,55,56]. Further, the voltage stability window of liquid electrolytes is generally between -3V to 4V[55–57] and liquid organic electrolytes have been shown to out-gas and explode, thus limiting the operating voltage and temperature of the battery[9,58–60].

All-solid-state sodium-ion batteries promise a cheap, safe alternative to current battery chemistries[61]. Solid state ceramic electrolytes show no electrode dissolution or SEI formation[62], have been shown to be stable beyond 5V[63,64], and are safe to use at high temperatures due to the intrinsic stability of ceramics. However, the room temperature conductivities of ceramic Na^+ electrolytes are usually several orders of magnitude lower than their organic counterparts[34,65,66].

NASICON, $Na_3Zr_2Si_2PO_{12}$, is one of the most promising and widely studied solid Na^+ electrolytes[35,36,67–69]. However, NASICON provides insufficient conductivity at room temperature as the high-conductivity, high-temperature rhombohedral phase (Figure 15a) is typically not stable at room temperature. Several studies have been published attempting to improve the ionic conductivity of the electrolyte through substitutional doping[42,44,45,70,71]. It has been demonstrated that ionic conductivity increases with increasing transition metal radius doped at the octahedral zirconium site[42,45]. However, the evidence for this trend was drawn from the silicon-free, and much less conductive, $NaZr_2P_3O_{12}$ compositional end member. Unlike $NaZr_2P_3O_{12}$, which is stable in the rhombohedral structure to room temperature, $Na_3Zr_2Si_2PO_{12}$ shows a transition to a low temperature monoclinic phase around 175 ^oC[38,72,73]. As would be expected, the monoclinic modification (Figure 15b) exhibits a higher activation energy (E_A) than the rhombohedral phase, limiting the room temperature conductivity.

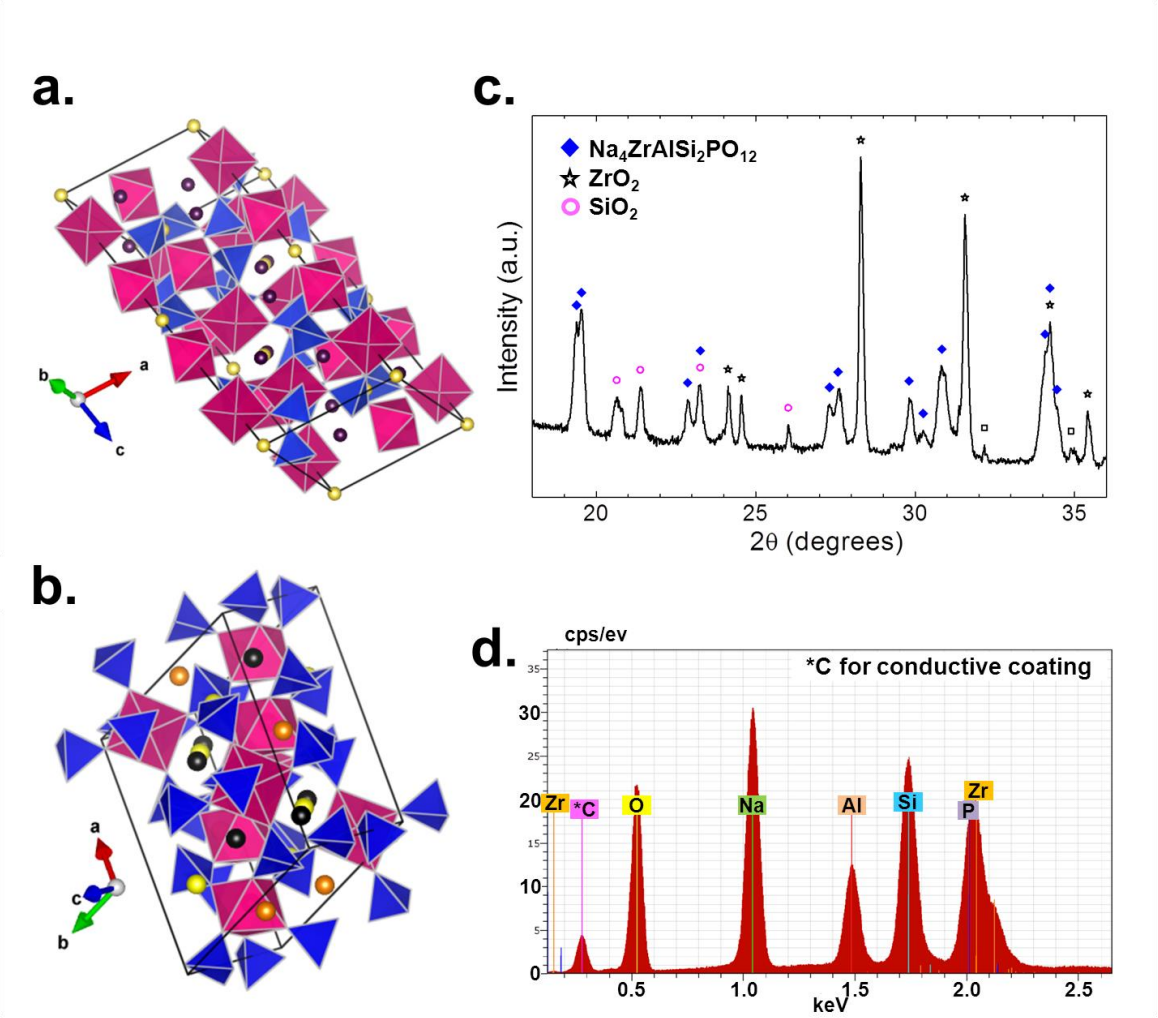

Figure 15. Unit cell structures of (a) highly conductive, high temperature rhombohedral phase and (b) the less conductive, low temperature monoclinic phase. The octahedra (pink) and tetrahedra (blue) represent ZrO6 and SiO4 (or PO4), respectively. The different colored spheres show the different sodium sites. The unit cell is outlined as a guide. (c) XRD pattern of $Na_4ZrAlSi_2PO_{12}$. Monoclinic NASICON, SiO_2, ZrO_2, and unidentified peaks are labeled as diamonds, circles, stars, and squares, respectively. (d) EDS spectra of $Na_4ZrAlSi_2PO_{12}$.

This study details the development of a higher performance solid-state Na^+ conducting electrolyte by doping trivalent transition metals of varying radius in the octahedral site of a NASICON-type structure. We investigated the dopant effect on

ionic conductivity and transference number, and analyzed the relationship between the dopant radius, lattice structure, and ionic conductivity. The prepared electrolyte with the smallest trivalent ion (Al^{3+}) showed high Na^+ conductivity of 1.9×10^{-3} S/cm at room temperature.

2.2 - Results and Discussion

The room temperature powder X-ray diffraction (XRD) pattern for $Na_4ZrAlSi_2PO_4$ is shown in Figure 15c and spectra for all other doped samples are shown in Figure 16. XRD pattern indexing reveals the monoclinic symmetry (space group C2/c) low temperature NASICON phase (Figure 15b) with common impurities of free monoclinic ZrO_2, and a lesser amount of SiO_2. These impurities are typical for NASICON, which is inherently difficult to prepare as a phase pure material[69,74,75]. These impurity phases are non-conductive and do not contribute to the measured conductivity. Thus the conductivities reported in this study are an underestimate, and higher purity materials should result in higher conductivity. Moreover, there is no evidence of Al-containing impurities, such as Al_2O_3, or $AlPO_4$, suggesting the Al dopant is in the NASICON lattice. XRD of other dopant samples are shown in Figure 16. In addition, energy dispersive X-ray spectroscopy (EDS) of $Na_4ZrAlSi_2PO_4$ confirmed that all the components (e.g., Na, Zr, Si, P, and Al) are present as shown in Figure 15d and given quantitatively in Table 1. After sintering, densities of all samples estimated by Archimedes' principle were over 90% of theoretical, though the ideal sintering temperature was lower with the doped NASICONs (1150 °C versus 1230 °C) as shown in Table 2.

Element	Series	Normal C (wt%)	Atom C (at. %)	Error	Normalized to NASICON cell
C	K	6.87	11.56	0.9	-
O	K	48.26	60.94	5.3	-
Na	K	14.52	12.76	0.9	4.18
Al	K	4.39	3.29	0.2	1.08
Si	K	7.71	5.55	0.3	1.82
P	K	4.3	2.81	0.2	0.92
Zr	L	13.94	3.09	0.6	1.01

Table 1. SEM EDS of $Na_4ZrAlSi_2PO_{12}$. High levels of oxygen and carbon content are due to biological materials in the SEM and on the surface of the NASICON and were not included in the normalization

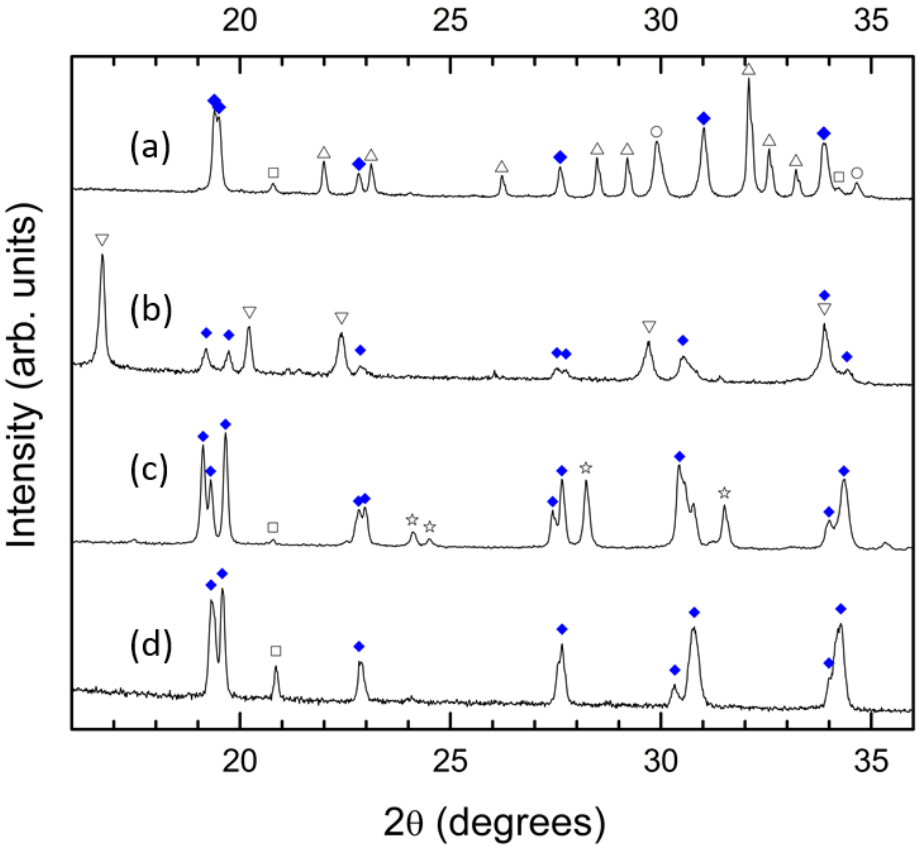

Figure 16. XRD spectra of (a) $Na_4ZrDySi_2PO_{12}$ (b) $Na_4ZrSbSi_2PO_{12}$ (c) $Na_3Zr_{1.94}Y_{0.06}Si_2PO_{12}$ (d) $Na_4ZrFeSi_2PO_{12}$. Phases present are monoclinic NASICON (blue diamonds), monoclinic ZrO_2 (open stars), $NaSbO_3$ (open downward triangles), $Dy_{4.67}(SiO_4)_3O$ (upward open triangles), $Dy_{0.2}Zr_{0.8}O_{1.9}$ (open circles), and unidentified peaks (open squares). All NASICON samples show strong monoclinic NASICON peaks, along with secondary products of $Dy_{4.67}(SiO_4)_3O$ and

$Dy_{0.2}Zr_{0.8}O_{1.9}$ for $Na_4ZrDySi_2PO_{12}$, $NaSbO_3$ for $Na_4ZrSbSi_2PO_{12}$, and monoclinic ZrO_2 for $Na_3Zr_{1.94}Y_{0.06}Si_2PO_{12}$. There are also two small unidentified peaks around 20.8° and 34.2°. Among these secondary phases, only $NaSbO_3$ is somewhat conductive, however, its reported conductivity is ~ 3 X 10^{-4} S/cm lower than that of our $Na_4ZrSbSi_2PO_{12}$ (e.g., 3.1 X 10^{-6} S/cm vs 10^{-2} S/cm at 300 °C), thus negligible ref. 76.

Material	Calcining Temperature (°C)	Sintering Temperature (°C)
$Na_3Zr_{1.94}Y_{0.06}Si_2PO_{12}$	1100	1230
$Na_4ZrAlSi_2PO_{12}$	1100	1150
$Na_4ZrFeSi_2PO_{12}$	900	1150
$Na_4ZrSbSi_2PO_{12}$	900	1050
$Na_4ZrDySi_2PO_{12}$	1100	1150

Table 2. Calcining and sintering temperatures required for various NASICON compositions.

Total conductivity was investigated by electrochemical impedance spectroscopy. Figure 17a shows the resultant Nyquist plots for $Na_4ZrAlSi_2PO_4$, from 25 – 300 °C. The spectra were deconvoluted by Z-plot software using a simple equivalent circuit as shown in Figure 18. In this circuit, L, R_o, R_1, CPE_1, and W represent inductance, bulk resistance, grain boundary resistance, constant phase element, and Warburg element for electrode, respectively. For grain boundary resistance (R_1), the arcs are clearly shown at low temperature (e.g., < 75 °C) but disappear at higher temperature (e.g., > 75 °C). Thus, at high temperatures, the grain boundary resistance is suppressed by the high frequency intercept. The fitting curves are overlapped with experimental data in Figure 17a. From the fitting results, the total

conductivity was calculated by the sum of bulk and grain boundary resistances (R_o + R_1) normalized for sample geometry.

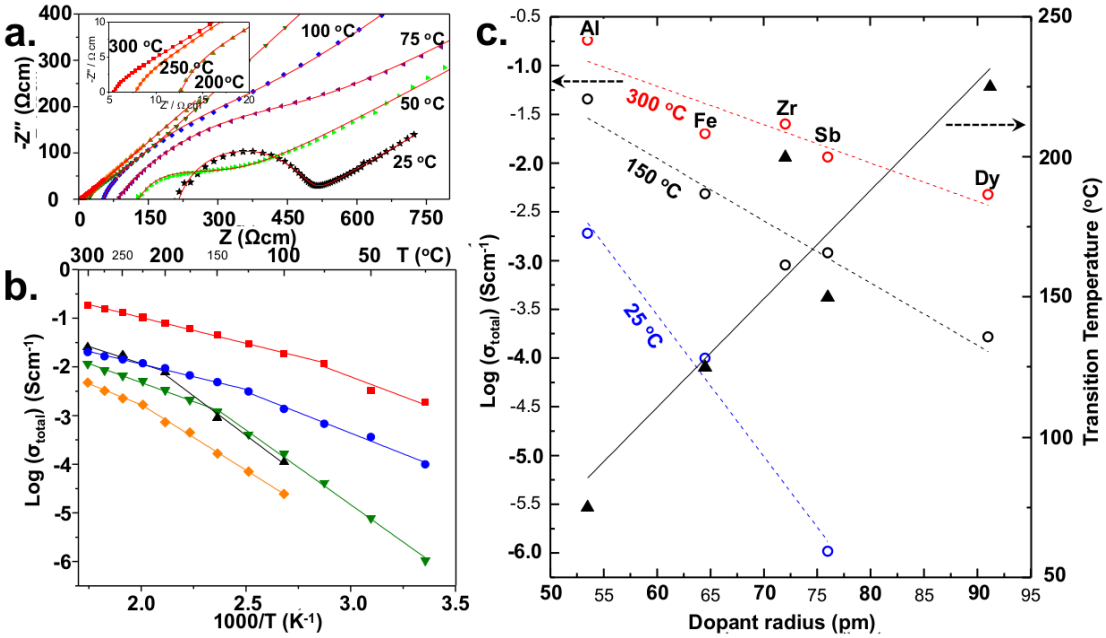

Figure 17. (a) Nyquist plots of $Na_4ZrAlSi_2PO_{12}$ measured from 25 to 300 °C. (b) Arrhenius plots of conductivity of $Na_4ZrAlSi_2PO_{12}$ (red square), $Na_4ZrFeSi_2PO_{12}$ (blue circle), $Na_3Zr_{1.94}Y_{0.06}Si_2PO_{12}$ (black upward triangle), $Na_4ZrSbSi_2PO_{12}$ (green downward triangle), and $Na_4ZrDySi_2PO_{12}$ (orange diamond). (c) Dependence of conductivity (left Y-axis, open symbols) for three isotherms: 300 °C (red), 150 °C (black), and 25 °C (blue) and transition temperature (right Y-axis, solid triangle) on dopant radius. Smaller radius dopants show a lower transition temperature. Due to the shift in transition temperature, the dependence of conductivity on radius is stronger at lower temperatures, producing a steeper slope.

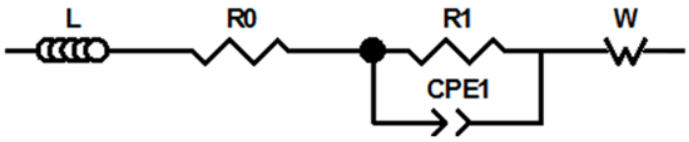

Figure 18. Equivalent circuit for NASICON, with R0 representing bulk resistance and R1 representing grain boundary resistance.

In addition, we measured the ionic transport number of doped NASICONs using 2 point DC conductivity measurement in the temperature range 25 – 300 °C. The results for the Fe- and Al-doped NASICONs at 25 °C are plotted in Figure 19.

The sharp current drop upon initial polarization shows the electronic conductivities of both doped NASICONs are negligible at all measured temperatures. For instance, the electronic conductivities of $Na_4ZrAlSi_2PO_4$ were 4.58×10^{-6} and 1.37×10^{-4} S/cm at 25 and 300 °C, respectively, while the ionic conductivities of the same sample were 1.90×10^{-3} and 1.82×10^{-1} S/cm at 25 and 300 °C, respectively, resulting in ionic transport numbers of > 0.999. Thus, demonstrating total conductivity values from AC impedance spectroscopy of doped NASICON samples are attributable to Na^+, and not electronic, conductivity.

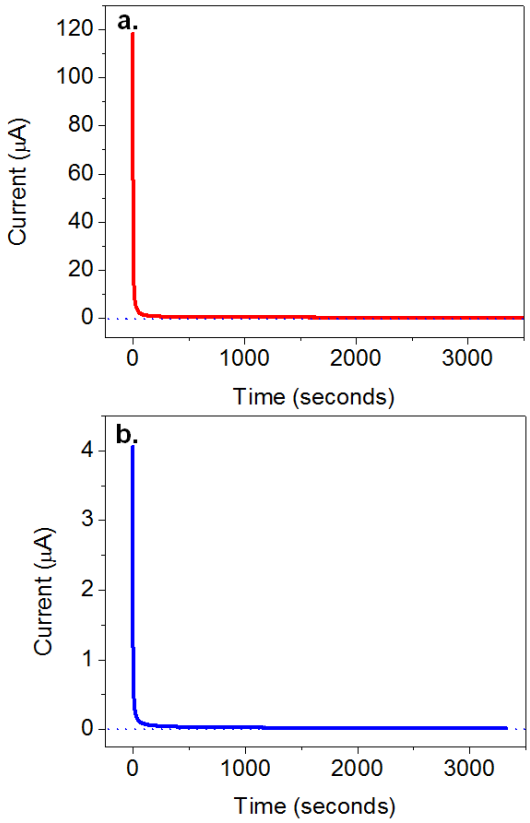

Figure 19. DC polarization experiments for (a, red) $Na_4ZrAlSi_2PO_4$ and (b, blue) $Na_4ZrFeSi_2PO_4$.

The ionic conductivity as a function of inverse temperature for the NASICON samples with trivalent dopants (of radius): Al(54pm), Fe(65pm), Sb(76pm) and

Dy(91pm); and the conventional NASICON (Zr(72pm)) are plotted in Figure 17b. The ionic conductivity for all samples exhibit a change in E_A, with a lower E_A above and a higher E_A below the transition temperature. This change in conductivity E_A is typical of NASICON and usually attributed to a phase transition from the rhombohedral (high temperature) to the monoclinic (low temperature) structure [29].

The conductivity and conductivity-E_A transition temperature dependence on ionic radii are plotted in Figure 17c. The conductivity transition temperature (right Y-axis) decreases linearly with decreasing dopant radii. The transition temperature of NASICON with Al doping (75 ^{o}C) is ~150 ^{o}C less than with Dy (225 ^{o}C), and ~125 °C less than the reference Zr (~200 °C). Moreover, this indicates a potential approach to stabilize the more conductive rhombohedral phase down to room temperature.

Further, the conductivity increases significantly with decreasing dopant radii. Figure 17c (left Y-axis) plots the dependence of conductivity radius for three isotherms; 300, 150, and 25 ^{o}C. Due to the shift in transition temperature, the dependence of conductivity on dopant radius is stronger at lower temperatures, producing a steeper slope. Thus, $Na_4ZrAlSi_2PO_4$ with the smallest dopant shows dramatically improved conductivity at all measured temperatures by 10 – 100 times compared to the conventional NASICON (e.g., 1.88×10^{-2} vs 1.11×10^{-4} S/cm at 100 ^{o}C). Charge balance with the lower valent dopants provides for more Na^+ in the lattice compared to the higher valence host ($Na_4ZrAlSi_2PO_{12}$ vs. $Na_3Zr_2Si_2PO_{12}$). Therefore, the superior Na^+ conductivity of Al-doped NASICON might be attributed to a synergetic effect of both transition temperature shift and enhanced Na^+ transport along with an increase in carrier density. Indeed, the fact that Zr fits the conductivity -

dopant radii trends (Figure 17c) so well is surprising given that Zr is tetravalent while the dopants are all trivalent. These results imply that the octahedral site dopant radius in the NASICON structure plays an important role in determining both the phase transition temperature and controlling the Na^+ transport mechanism, thus tailoring Na^+ conductivity. This higher Na^+ conductivity with smaller radius dopants can be explained in terms of modification of the ionic conduction pathways. One of the main conduction pathways in monoclinic NASICON is shown schematically in Figure 20a, based on the study by Mazza et al.[77]. In this ionic conduction pathway, which has a larger radius than that of Na^+, hopping occurs from one Na^+[1] site (yellow) to a Na^+[2] site (orange) through alternating silicate or phosphate tetrahedra and transition metal octahedra.

When smaller radii Al^{3+} are substituted into octahedral Zr^{4+} sites, the decreased bonding distance between the metal ion and its associated oxygen ions will shrink the size of the octahedra. If this reduction in octahedra size were to reduce lattice parameter/volume, the radii of the conduction pathways would also decrease corresponding to an expected decrease in conductivity. However, XRD results reveal a more complicated shift in lattice parameters, with *a* and *c* increasing while *b* decreases with decreasing dopant radii (Figure 20c). Thus, counterintuitively the resulting unit cell volume increases with decreasing dopant radius (Figure 20d). This implies there is an accommodating expansion of adjacent tetrahedral sites, by extended Si-O or P-O bonding lengths, resulting in a more open local structure for Na^+ conduction path as shown schematically in Figure 20b. This hypothesis will be

confirmed in future studies with neutron diffraction and solid state nuclear magnetic resonance.

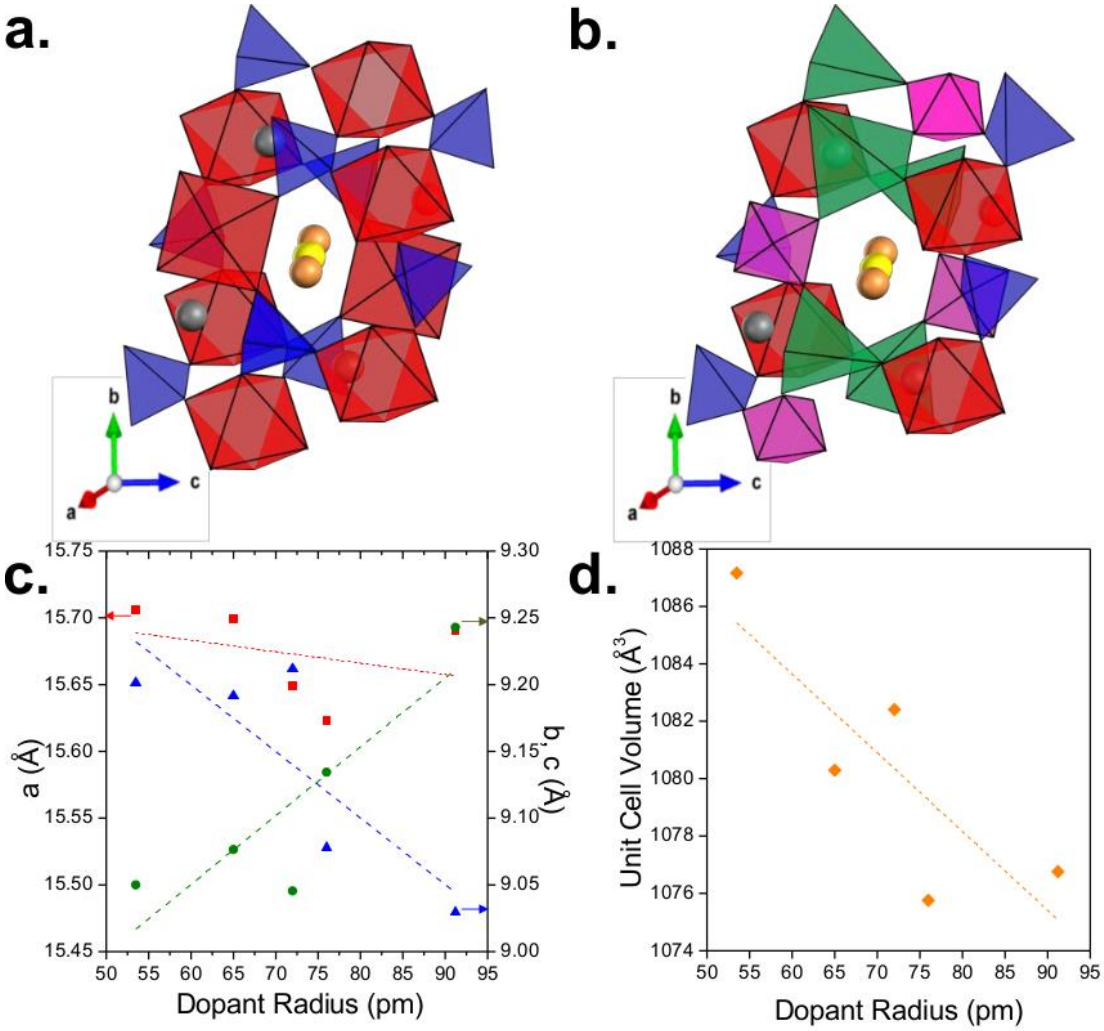

Figure 20. (a) Schematic diagram of one of the major conduction pathways for monoclinic phase NASICON consisting of ZrO_6 octahedra (red), SiO_4 or PO_4 tetrahedra (blue), Na[1] sites (yellow), Na[2] sites (orange), Na[3] sites (black). In this path, hopping occurs from Na[1] to Na[2]. (b) Hypothetical monoclinic structure with Al^{3+} incorporation in the octahedral sites (pink) and expanded tetrahedral sites (green), resulting in more open local structure for Na^+ conduction pathway. (c) Calculated lattice parameters with different dopant radius. Square (red), circle (green), and triangle (blue) represent a, b, and c lattice parameters, respectively. Dashed lines show linear fit of the measured data points. The result shows that a, c lattice parameters increase with smaller dopant radius, while b decreases as the dopant radius increases. (d) Estimated unit cell volume based on calculated lattice parameters in (c), showing that smaller sized dopant expands unit cell volume.

Figure 21 compares the total conductivity of $Na_4ZrAlSi_2PO_{12}$ with state-of-the-art solid and liquid electrolytes for Na^+ and Li^+ batteries. The Al-doped NASICON has superior conductivity to most other solid Na^+ and Li^+ electrolytes, and similar conductivity to the highest reported values of polycrystalline Na-ß-alumina and $Na_3Zr_{1.94}Y_{0.06}Si_2PO_{12}$[78]. It should be noted that single crystal Na-ß-alumina has 1-2 orders of magnitude higher conductivity than the polycrystalline form, but with limited practical applications due to its anisotropic nature[79].

The literature reports a wide range of total conductivity for NASICON even for the same composition by the same group (as shown in Figure 21 for $Na_3Zr_{1.94}Y_{0.06}Si_2PO_{12}$ by Fuentes et al[80,81]) due to difficulty of avoiding secondary (e.g., ZrO_2) and glassy phase formation. Because of this the total conductivity of our reference $Na_3Zr_{1.94}Y_{0.06}Si_2PO_{12}$ is significantly less than the highest reported value for the same material studied by Fuentes et al[80,81]; however, as noted there is a wide range of values reported for this composition and NASICONs[44,75,82,83] in general. Thus, further optimization of the synthesis process to reduce the amount of non-conducting secondary phases could increase the conductivity of $Na_4ZrAlSi_2PO_{12}$ over 1-2 orders of magnitude.

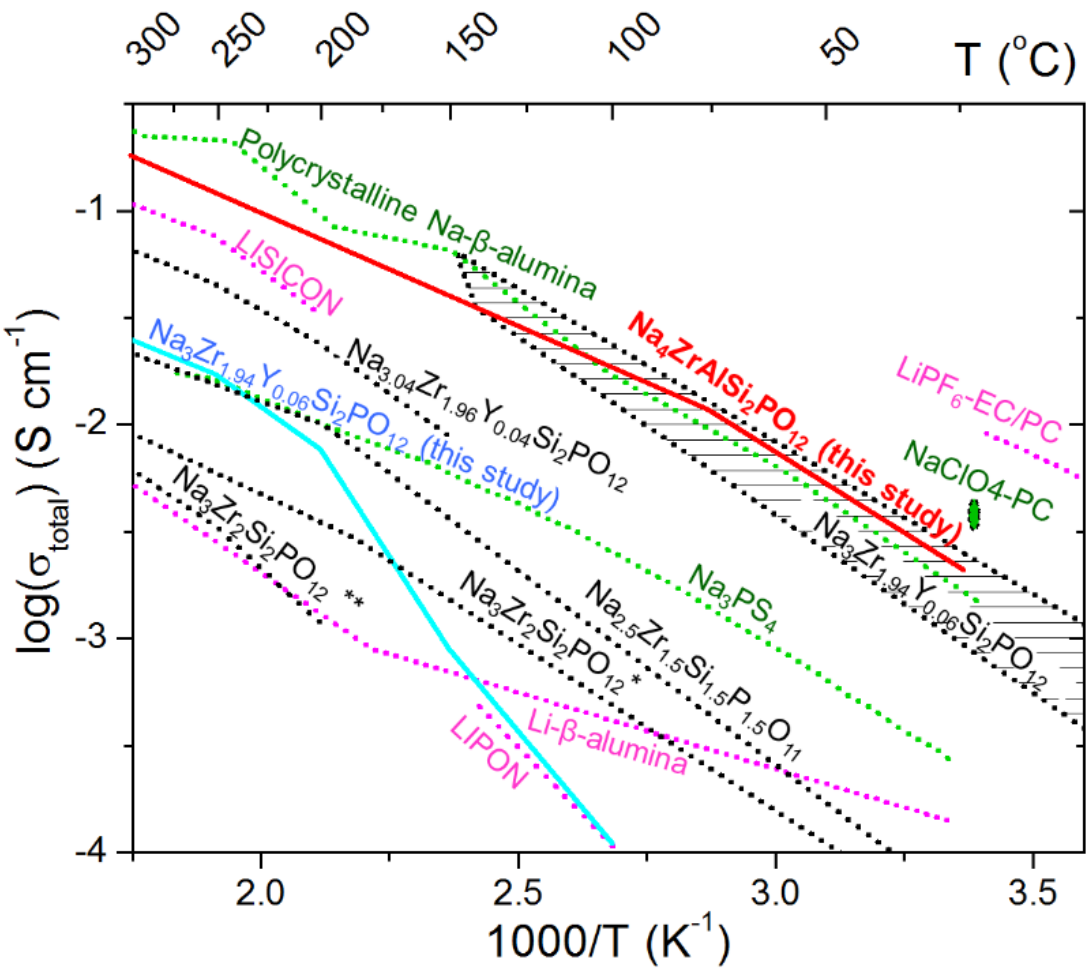

Figure 21. Temperature dependence of Na+ and Li+ ion conductivities of various electrolytes for rechargeable battery applications from room temperature (~25 °C) to 300 °C. Conductivity of $Na_4ZrAlSi_2PO_{12}$ and $Na_3Zr_{1.94}Y_{0.06}Si_2O_{12}$ solid electrolytes (solid lines) from this study are compared with that of Na-β-alumina (polycrystalline)[34], $Na_3Zr_{1.94}Y_{0.06}Si_2O_{12}$ (range from Fuentes et al. indicated by the patterned area)[80,81], $Na_{3.04}Zr_{1.96}Y_{0.04}Si_2O_{12}$[44], $Na_3Zr_2Si_2PO_{12}$[75,82], $Na_{2.5}Zr_{1.5}Si_{1.5}P_{1.5}O_{11}$[83], Na_3PS_4[63], LISICON[78], Li-β-alumina[78], LIPON[78], and liquid organic electrolytes (LiPF6 in ethylene carbonate (EC) / polyethylene carbonate (PC)[65] or $NaClO_4$ in PC[66]) from literature (dotted lines).

Regardless, the current conductivity of $Na_4ZrAlSi_2PO_{12}$ rivals that of liquid organic electrolytes, such as $LiPF_6$ in ethylene carbonate (EC) / polyethylene carbonate (PC) or $NaClO_4$ in PC. Moreover, the Na-ion transport number of $Na_4ZrAlSi_2PO_{12}$ is over 0.999, thus increasing battery charge-discharge cycle

efficiency compared to liquid organic electrolytes which typically have a transport number below 0.5.

It was demonstrated that Na^+ conductivity of NASICON type solid electrolytes is enhanced with smaller radius trivalent dopants in the octahedral site which resulted in a novel Na^+ solid electrolyte, $Na_4ZrAlSi_2PO_{12}$. Room temperature Na^+ conductivities of 1.9×10^{-3} Scm^{-1} are comparable to those of organic liquid electrolytes, thus opening the door for truly high performance, inexpensive all-solid-state Na^+ batteries. Moreover, the strategies employed in this work present the opportunity for a wide range of fundamental studies on ionic mobility in the bulk material and enhancement of ionic conductivity of solid electrolytes for utility scale energy storage and other electrochemical devices that require high performance and safety at a low cost.

This work was further extended and improved upon by Adam Jolley with my assistance. Using the same strategy but varying the lattice parameter and oxidation state of the dopant, we were able to improve this conductivity to 3.75×10^{-3} Scm^{-1} at room temperature with $Na_{3.4}Zr_{1.8}Zn_{0.2}Si_2PO_{12}$. These results are shown in Figure 22. These samples were also confirmed to be pure ionic conductors using DC polarization experiments.

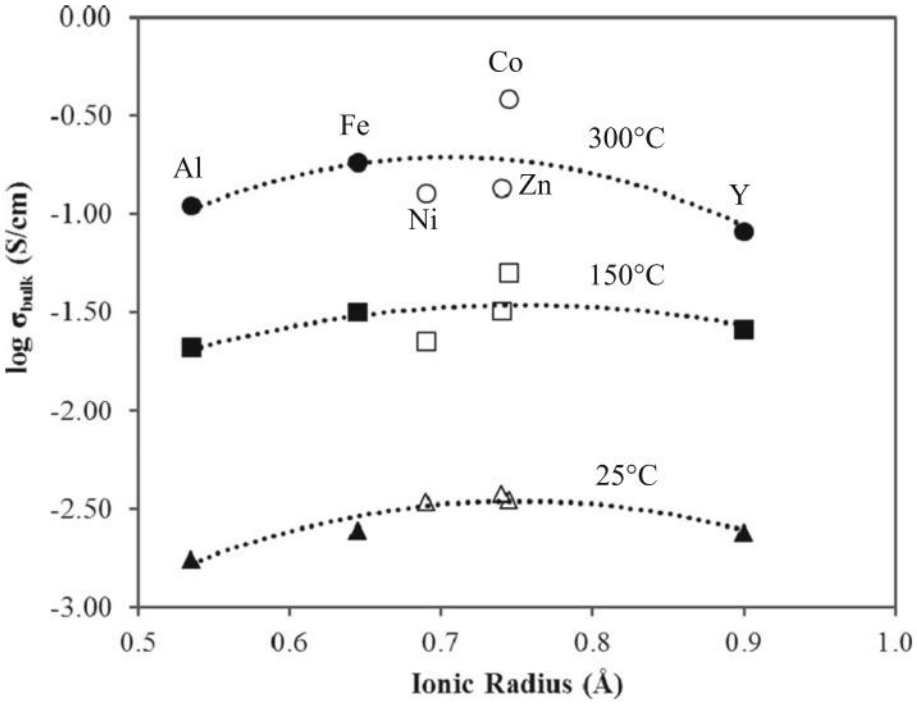

Figure 22. Bulk conductivity of doped NASICON vs. the ionic radius of the dopant. Circles represent conductivity at 300 ºC, squares represent conductivity at 150 ºC and triangles represent conductivity at 25 ºC. Black shaded shapes represent +3 oxidation state dopants, and while shapes are +2 oxidation state dopants. A polynomial fit was used to describe the best fit line.

2.3 - Methods

2.3.1 - Material Preparation

$Na_{3+x}Zr_{2-x}M_xSi_2PO_{12}$ ($M=Al^{3+}$, Fe^{3+}, Sb^{3+}, Dy^{3+}) was synthesized with a conventional solid state reaction for the compositions x=0 (un-doped) and x=1 (doped). The starting materials used were Na_2CO_3 (Sigma-Aldrich, 99.95-100.05%), amorphous SiO_2 (Aldrich, 99.80%), $NH_4H_2PO_4$ (Aldrich, 99.999%), and different zirconium sources for undoped and doped samples. For reference samples, 3% yttria-doped tetragonal zirconia polycrystal (Tosoh Corporation, TZ-3Y) was used as the zirconium source. It has been shown that this zirconium source produces a more pure

NASICON phase[37-38]. Nanocrystalline ZrO_2 (Inframat Advanced Materials, 99.9%) was used as the zirconium source for all doped compositions.

Starting materials were mixed in stoichiometric proportions and ball milled overnight in ethanol. After drying at 100°C, the material was calcined for 8 hours in an alumina crucible at temperatures given in Table 2. The calcined powder was again ball milled overnight then dried at 100°C. Sample powder was pressed uniaxially into a pellet with a pressure of 200 MPa in an 8mm diameter steel die and was sintered for 16 hours in an alumina crucible at temperatures given in Table 2.

2.3.2 - Characterization

X-ray diffraction patterns of sintered and ground pellets were collected at room temperature using a Bruker D8 Advance diffractometer with CuKα radiation and a LynxEye detector. Patterns were recorded between 10° and 60° (2θ) with a 0.015° step size and 0.5 second count time. Quantitative elemental analysis of $Na_4ZrAlSi_2PO_{12}$ was conducted by energy-dispersive X-ray spectroscopy (EDS) using a Hitachi SU-70 scanning electron microscope (SEM).

Electrochemical characterizations were made with pressed and sintered pellets. Electrodes were coated on opposite pellet faces with silver paste and heated at 750°C for 1 hour in air. Silver mesh was attached to platinum leads embedded in the silver paste prior to sintering.

Impedance was measured with a Solartron 1260 from 10 Hz to 30 MHz between room temperature and 300° C in ambient air. Total conductivity was determined by fitting the equivalent circuit shown in Figure 18 with Scribner Z-Plot

software and normalizing the resistance by pellet thickness and area.

DC measurements were made at room temperature and 300°C in air and normalized by pellet thickness and area. The same pellets tested for impedance were tested for relative ionic and electronic conductivity by current interrupt. Pellets were connected to the positive and negative outputs of a Keithley 2400 Broad Purpose SourceMeter. A 100 mV bias was applied and measurements were continued until the current stabilized after decay.

Chapter 3: Development of a Super-lithiated Garnet

3.1 - Introduction

Solid Li ion electrolytes exhibiting conductivity in the order of 1 – 10 $mScm^{-1}$ or higher at battery operating temperature, high electrochemical stability (up to ≥ 6/Li), chemically inert to side reactions with elemental Li and Li-metal alloy anodes and high voltage Li cathodes (e.g., $LiCoO_2$, $LiMPO_4$ (M = Co, Ni, Fe) and $Li_2(Fe,Co)Mn_3O_8$) are being considered as an ideal replacement for combustible organic polymers and $LiPF_6$ electrolytes in current Li^+ ion batteries. Unlike polymer electrolytes, ceramic Li^+ ion electrolytes conduct charge solely due to Li^+ ions (transference number for Li ions ≈ 1) while anions (e.g., O^{2-}, S^{2-} and N^{3-}), host framework cations, and electrons do not contribute significantly to total ionic conductivity[4]. Therefore, a successful solid ceramic Li^+ ion conducting electrolyte will overcome long-standing issues in safety and energy density of existing batteries used in electric vehicle (EV) applications.

To this end, several inorganic crystalline and amorphous solid Li^+ ion electrolytes such as A-cation deficient perovskite-type $La_{(2/3)-x}Li_{3x}\square_{(1/3)-2x}TiO_3$ (□ = vacancy) sodium superionic conducting $Na_3Zr_2Si_2PO_{12}$ (NASICON)-type structure $LiTi_2P_3O_{12}$, Li-beta alumina, Li_3N, Li_4SiO_4-Li_3PO_4 and $Li_{10}GeP_2S_{12}$ are being developed[78,84–90]. However, Ti and S based solid electrolytes are generally reactive with elemental Li and sensitive to moisture, which makes them impractical for battery membrane applications. Li-stable layered structured Li_3N and Li-beta-alumina are

also not suitable for practical application due to their low electrochemical stability window (e.g., decomposition voltage of Li_3N at room temperature is ~ 440 mV) and anisotropic conductivity.

Unlike other known ceramic electrolytes, recently developed garnet-type structured Li- stuffed metal oxides of the nominal chemical formulae $Li_5La_3M_2O_{12}$ (M = Nb, Ta), $Li_6ALa_2M_2O_{12}$ (A = alkaline earth ions) and $Li_7La_3C_2O_{12}$ (C = Sn, Zr) exhibit total (bulk + grain-boundary) conductivity in the range of ~ 10^{-8} - 10^{-4} Scm^{-1} at room temperature[21,23,24,27,28,30,91–95]. The chemical stability of Zr-based garnets against reaction with elemental Li and $LiCoO_2$ cathode and their high electrochemical stability (up to 6 V/Li at room temperature) make them attractive candidate for the development of high power and energy density all-solid state Li^+ ion secondary batteries. However, the ionic conductivity of cubic Li_7-Zr phase, $Li_7La_3Zr_2O_{12,}$ turns out to depend on synthesis conditions, including sintering temperature and nature of the crucible used[28]. It has been suggested that Al-doping from the reaction container seems to stabilize the high conducting cubic phase[27,30], while low-temperature cubic Li_7-Zr phase prepared by wet chemical methods show about 2-3 orders of magnitude lower electrical conductivity[96] due to poor density of the electrolyte. In this paper, we report highly conducting cubic Li rich Li_7-Zr phase prepared at 950 °C, which enabled us to avoid Al doping (commonly observed with higher temperature sintering[27,30]) and conductivity was found to be comparable to literature.

3.2 - Experimental Aspects

Li-Stuffed $Li_{7.06}La_3Zr_{1.94}Y_{0.06}O_{12}$ and $Li_{7.16}La_3Zr_{1.84}Y_{0.16}O_{12}$ were prepared in air by ceramic methods using stoichiometric amounts of La_2O_3 (99.9 % Aldrich) (pre-dried in air at 800 °C for several hours), $LiNO_3$ (99.9 % Aldrich) (10 wt.% excess was added to compensate potential loss of Li during the sintering), and 3 or 8 mol% Y-doped ZrO_2 (YSZ) (TOSOH Corporation, TZ-3Y or TZ-8Y). The selected compositions were based on commercially available YSZ samples. The precursor powders were ball-milled for 10-24 h hours using zirconia balls and iso-propanol. The samples were sieved and dried in a 100 °C air oven for couple of hours. The resultant samples were transferred into clean alumina crucibles and heated to 700 °C for 12 h (5 °C/min). After pre-calcination, the resultant samples were again ball-milled for 24 h and dried before being pressed into pellets (uni-axial pressure at 113MPa) and sintered at 950 °C for 12 h and 1100 °C for 12 h. Pellets were fully surrounded with their powdered material to avoid any potential contamination with the reaction vessel and to suppress the loss of lithium during the sintering. All the samples were characterized using powder X-ray diffraction (D8 powder X-ray diffractometer, 40 kV, 40 mA) and scanning electron microscopy (SEM) (Hitachi SU-70) combined with elemental mapping analysis (Bruker silicon drift detector). The electrical conductivity was measured in air using Ag electrodes (Fuel Cell Materials, cured at 600 °C in air for 30 mins, prior to measurement) and measurements were performed while sample was cooling after stabilization at each temperature. Raman spectroscopy was performed with a 532 nm laser using a Horiba LabRAM ARAMIS Raman microscope. The microscope settings used included a

grating of 1800 mm^{-1} and a D2 filter (100x intensity reduction). Results were measured between wavenumbers from 25 cm^{-1} to 1300 cm^{-1}.

3.3 - Results and Discussion

Figure 23 shows powder XRD patterns of as-prepared Li-Stuffed $Li_{7.06}La_3Zr_{1.94}Y_{0.06}O_{12}$ and $Li_{7.16}La_3Zr_{1.84}Y_{0.16}O_{12}$ at 950 and 1100 °C in air. Interestingly, we see the cubic garnet-type phase was stabilized at the lower temperature using solid state reactions, and increasing temperature above 950 °C decomposes into several Li containing phases. We also noticed a similar decomposition of the garnet-type phase if we hold it long period of time (over 48 h) at 950 °C in air. This could be attributed due to evaporation of lithium. Impurity peaks due to phases iso-structural with "$Li_{19}Nd_{36}Fe_7O_{76}$" (Joint Committee on Powder Diffraction Standards (JCPDS) 46-1250), "$Li_2Fe_3SbO_8$" (JCPDS 76-1082), and unknown phases are marked as squares, stars and diamonds, respectively. We could index all the main garnet-associated diffraction peaks of 950 °C (12h) samples on a cubic cell constant 12.974(3) Å and 12.995(2) Å for $Li_{7.06}La_3Zr_{1.94}Y_{0.06}O_{12}$ and $Li_{7.16}La_3Zr_{1.84}Y_{0.16}O_{12}$, respectively. Table 3 lists cell constants of Li-stuffed Li_7 phases reported in the literature together with present research[21,27,30,94,96]. A slight increase in cell constant can be explained by substitution of larger Y ions (ionic radius at six-fold coordination number is 0.9 Å) for smaller Zr ions (ionic radius at six-fold coordination number is 0.72 Å) at the octahedral coordination[97]. Table 4 shows the indexed PXRD patterns of $Li_{7.06}La_3Zr_{1.94}Y_{0.06}O_{12}$ and $Li_{7.16}La_3Zr_{1.84}Y_{0.16}O_{12}$ at 950 °C. The indexing was performed using a PROSZKI program[98].

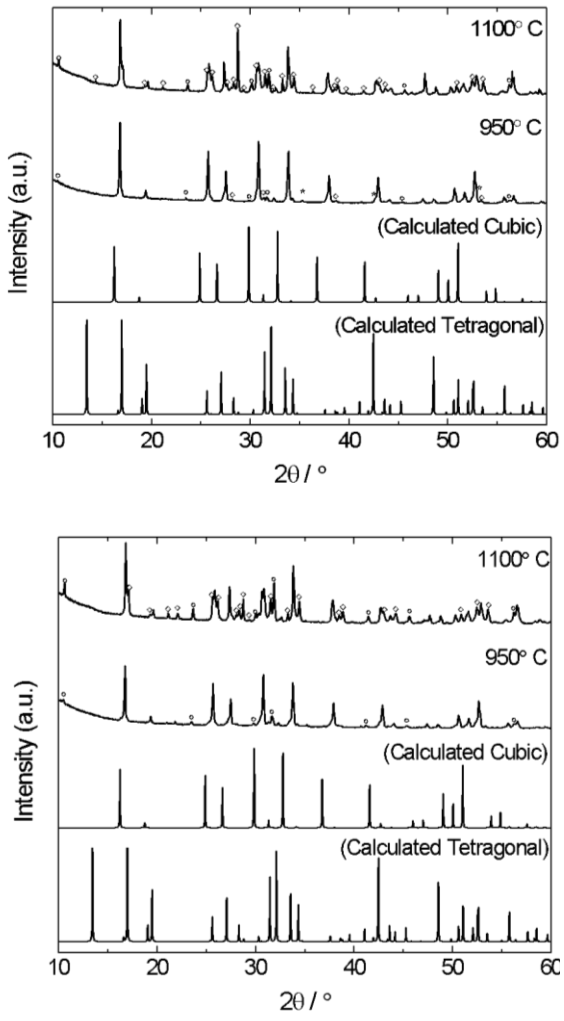

Figure 23. PXRD showing the formation of cubic garnet-type (a) 3 mol% YSZ–doped $Li_{7.06}La_3Zr_{1.94}Y_{0.06}O_{12}$ and (b) 8 mol % YSZ–doped $Li_{7.16}La_3Zr_{1.84}Y_{0.16}O_{12}$ at 950 °C in air and cubic phase was retained at 1100 °C. Calculated PXRD patterns for cubic and tetragonal garnet-type structures are shown for comparison. Impurity peaks due to phases iso-structural with $Li_{19}Nd_{36}Fe_7O_{76}$ (JCPDS 46-1250) and $Li_2Fe_3SbO_8$ (JCPDS 76-1082) are marked as squares and stars, respectively. Unidentified peaks are marked with diamonds.

Compound	Synthesis	*a* (Å)	μ (cm^2/V s)	D (cm^2/s)	Reference
$Li_{7.06}La_3Zr_{1.94}Y_{0.06}O_{12}$	Ceramic	12.974(3) (PXRD)	3×10^{-10}	7×10^{-12}	Present work
$Li_{7.16}La_3Zr_{1.84}Y_{0.16}O_{12}$	Ceramic	12.995(2) (PXRD)	2×10^{-10}	5×10^{-12}	Present work
$Li_7La_3Zr_2O_{12}$	Ceramic	12.94927(17) (ND)	-	-	21
$Li_7La_3Zr_2O_{12}$	Ceramic	12.9720 (PND)	3×10^{-8}	9×10^{-10}	19
$Li_{6.6}La_3Zr_{1.5}Ta_{0.5}O_{12}$	Ceramic	12.9450 (PND)	2×10^{-3}	4×10^{-7}	19
$Li_7La_3Zr_2O_{12}$	Ceramic	12.9751(1) (Single crystal XRD)	3×10^{-10}	9×10^{-12}	16
$Li_7La_3Zr_2O_{12}$	Sol-gel	13.002(1) (PXRD)	5×10^{-11}	1×10^{-12}	22
$Li_7La_3Zr_2O_{12}$	Ceramic	12.9682(6) (PXRD)	4×10^{-8}	1×10^{-9}	14

PXRD = Powder X-ray diffraction; PND- Powder neutron diffraction.

Table 3. Comparison of cell constant (a), synthesis method, room temperature electrical mobility (μ), diffusion coefficient (D) of $Li_{7.06}La_3Zr_{1.94}Y_{0.06}O_{12}$ and $Li_{7.16}La_3Zr_{1.84}Y_{0.16}O_{12}$ with other lithium garnets reported in the literature.

			$Li_{7.06}La_3Zr_{1.94}Y_{0.06}O_{12}$			$Li_{7.16}La_3Zr_{1.84}Y_{0.16}O_{12}$		
h	*k*	*l*	$d_{(obs.)}$ Å	$d_{(cal.)}$ Å	$I_{(obs)}$%	$d_{(obs.)}$ Å	$d_{(cal.)}$ Å	$I_{(obs)}$%
2	1	1	5.274	5.297	100	5.292	5.305	100
2	2	0	4.571	4.587	19	4.582	4.594	22
3	2	1	3.461	3.467	66	3.468	3.473	73
4	0	0	3.238	3.244	41	3.246	3.249	49
4	2	0	2.898	2.901	78	2.904	2.906	87
4	2	2	2.646	2.649	66	2.651	2.653	75
5	2	1	2.367	2.369	36	2.372	2.373	43
6	1	1	2.105	2.105	34	2.107	2.109	39
6	3	1	1.913	1.913	8	1.916	1.916	11
4	4	4	1.872	1.873	8	1.876	1.876	10
6	4	0	1.800	1.800	22	1.802	1.802	25
7	2	1	1.766	1.766	17	1.769	1.768	19
6	4	2	1.735	1.734	42	1.737	1.737	46
6	5	1	1.648	1.648	10	1.651	1.650	12
8	0	0	1.623	1.622	12	1.625	1.624	15
Cell constant (a) (Å)				12.974		12.995		
a error (Å)				0.003		0.002		
Cell volume (V) ($Å^3$)				2183.79		2194.87		
V error ($Å^3$)				1.53		1.00		
Average 2- theta diff.				0.03		0.02		
FM value				8		13		

Table 4. Indexed PXRD of $Li_{7.06}La_3Zr_{1.94}Y_{0.06}O_{12}$ and $Li_{7.16}La_3Zr_{1.84}Y_{0.16}O_{12}$.

SEM was used to study the microstructure and formation of potential secondary phases in the investigated Y-doped garnets. Secondary electron and backscattered electron images were recorded at different magnifications (1k, 6k and 10k). Figure 24Figure 27 show the typical SEM images as-prepared $Li_{7.06}La_3Zr_{1.94}Y_{0.06}O_{12}$ and $Li_{7.16}La_3Zr_{1.84}Y_{0.16}O_{12}$ pellets. As anticipated, the crystallite size increases with increasing final sintering temperature. At a fixed temperature, the samples show rather uniform distribution of crystallite in the range of 2 microns and Y content seems not to affect the particle size. The backscattered images of 950 °C samples do not show distinct regions of light color contrast, confirming a uniform atomic distribution associated with a single-phase garnet-type

structure. However, the 1100 °C sintered samples show regions with different contrast indicating multiphase samples, in agreement with PXRD data (Figure 23). All the investigated samples show high porosity, measured to be around 54% of theoretical density (obtained using mass/geometric volume ratio).

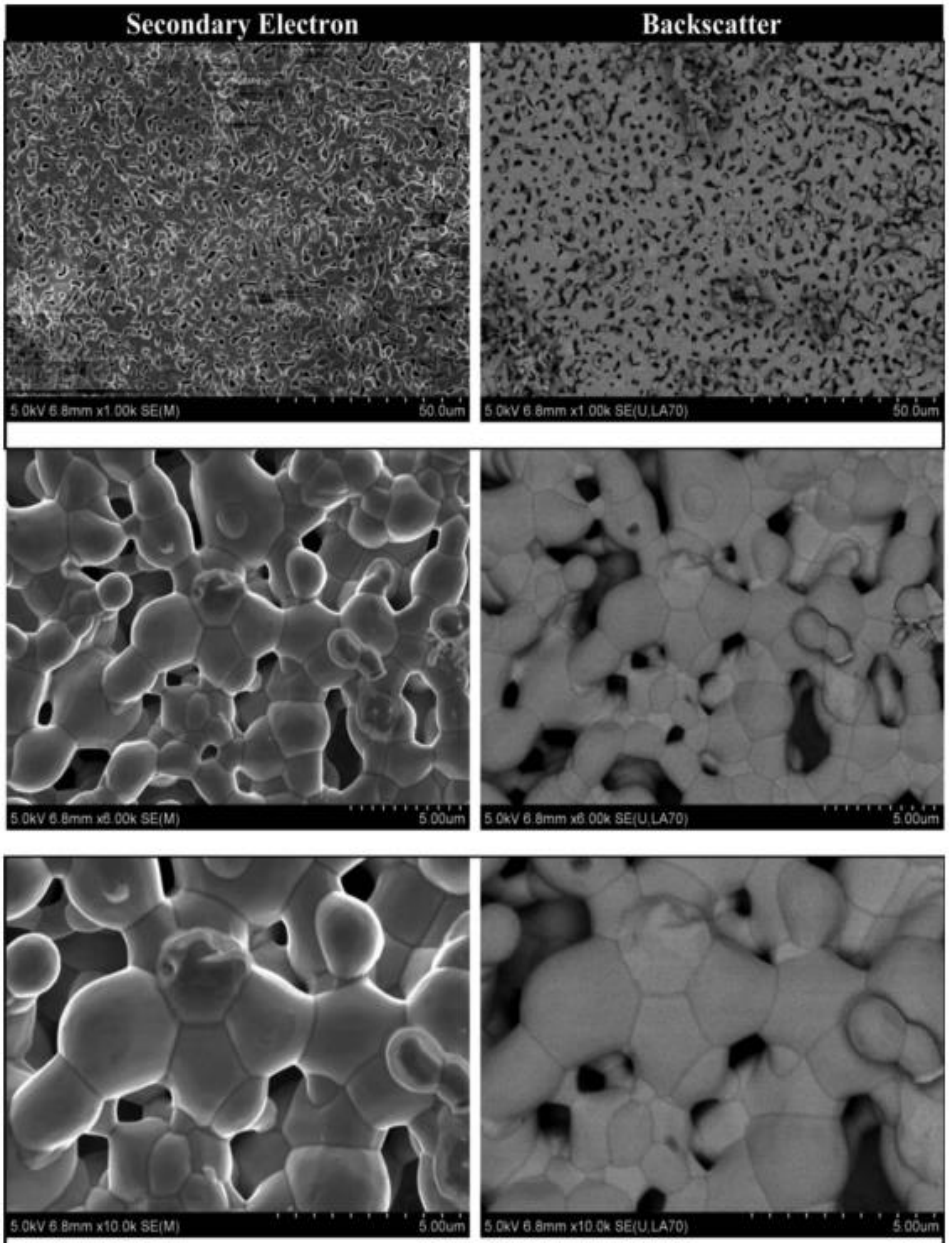

Figure 24. Typical SEM images of cubic garnet-type 3 mol% YSZ–doped $Li_{7.06}La_3Zr_{1.94}Y_{0.06}O_{12}$ prepared at 950 °C in air. The back scattered SEM images indicate no direct evidence for second phase formation at 950 °C.

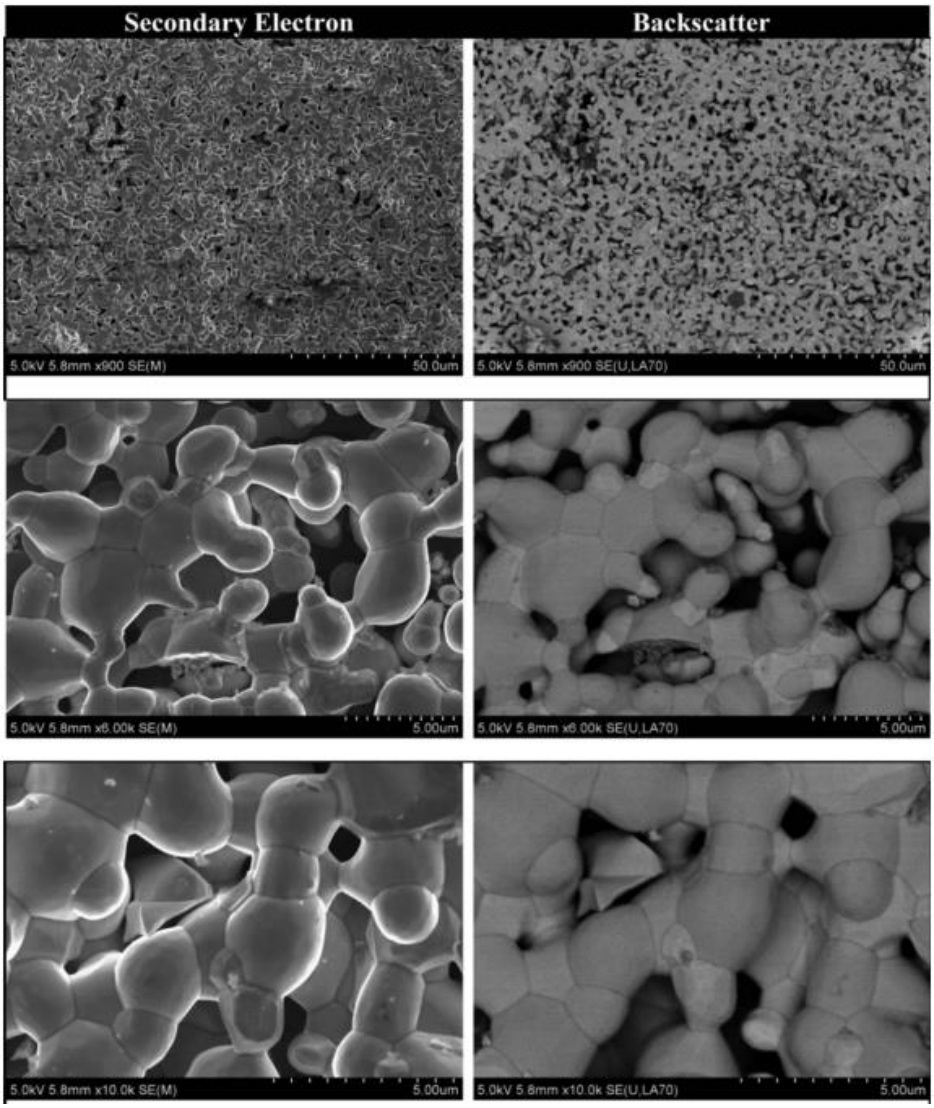

Figure 25. Typical SEM images of cubic garnet-type 8 mol % YSZ–doped $Li_{7.16}La_3Zr_{1.84}Y_{0.16}O_{12}$ prepared at 950 °C in air. The back scattered SEM images indicate no evidence for second phase formation.

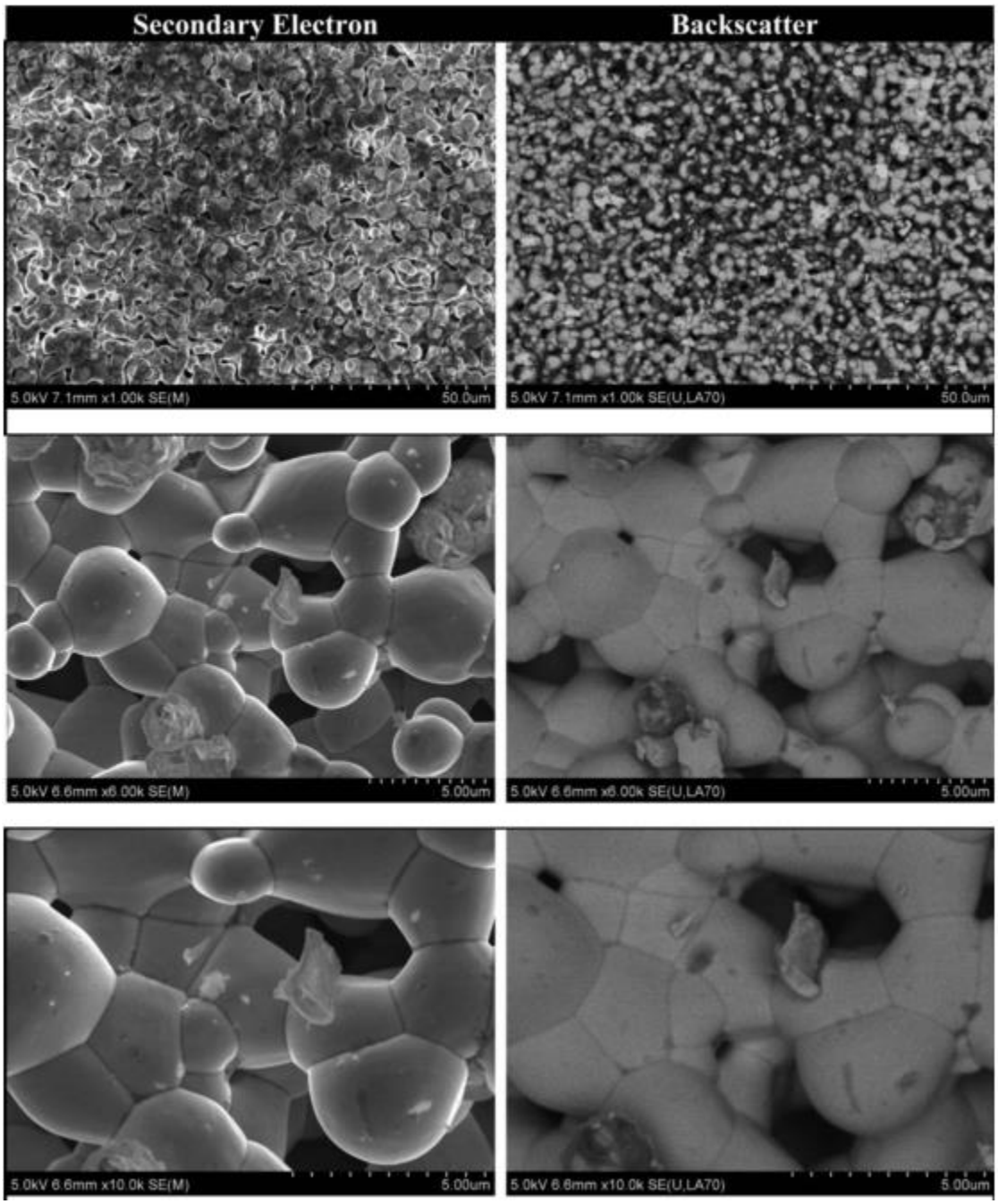

Figure 26. Typical SEM images of cubic garnet-type 3 mol% YSZ–doped $Li_{7.06}La_3Zr_{1.94}Y_{0.06}O_{12}$ prepared at 1100 °C in air. The back scattered SEM images indicate direct evidence for second phase formation.

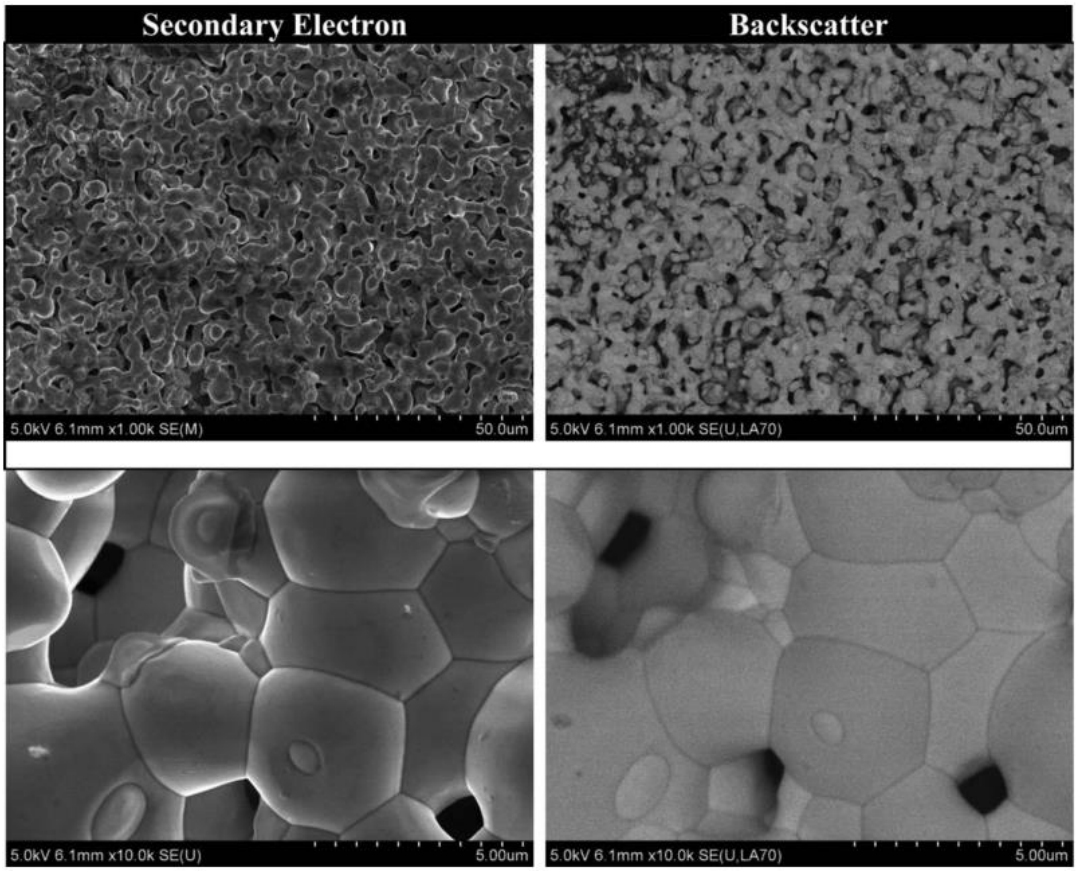

Figure 27. Typical SEM images of cubic garnet-type 8 mol % YSZ–doped $Li_{7.16}La_3Zr_{1.84}Y_{0.16}O_{12}$ prepared at 1100 °C in air. The back scattered SEM images indicate direct evidence for second phase formation.

Figure 28 and Figure 29 are elemental mappings of higher atomic elements in $Li_{7.06}La_3Zr_{1.94}Y_{0.06}O_{12}$ and $Li_{7.16}La_3Zr_{1.84}Y_{0.16}O_{12}$ synthesized at 950 °C. We see a uniform distribution of atoms over the couple of hundred microns with no apparent enrichment of Y at the grain- boundaries. SEM images overlaid with EDS mappings of Al content in $Li_{7.06}La_3Y_{0.06}Zr_{1.94}O_{12}$ and $Li_{7.16}La_3Y_{0.16}Zr_{1.84}O_{12}$ sintered at 1100 °C are shown in Figure 30. These images indicate there is no Al segregation to the grain-boundaries,19 rather uniform distribution of Al signal was observed compared to 950 °C samples (Figure 28 and Figure 29). Al contamination from the crucible is commonly observed in the preparation of garnet-type metal oxides and we did not see

evidence of Al segregation at the grain-boundaries, as reported for Ta-doped $Li_7La_3Zr_2O_{12}$.19 In the present study, SEM-EDS shows no evidence of Al segregation at the grain boundaries, though this technique may not have sufficient resolution to show low concentrations which do not stand above the noise of the EDS. Furthermore, we also did not see any potential Al-containing impurity phases in the PXRD (Figure 23). While this does not prove the absence of Al contamination or segregation to grain boundaries, it can be considered a significant improvement from the high Al segregation shown by the same techniques in Li et al.19

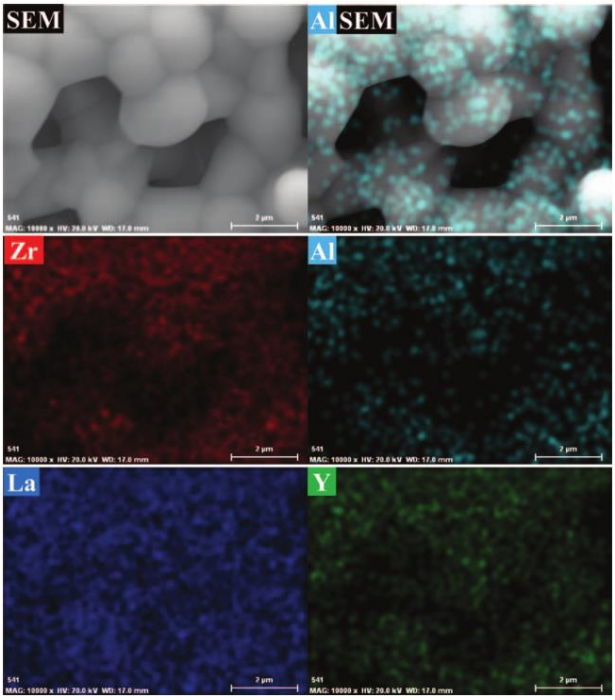

Figure 28. Elemental mapping of garnet-type 3 mol% YSZ–doped $Li_{7.06}La_3Zr_{1.94}Y_{0.06}O_{12}$ prepared at 950 °C in air.

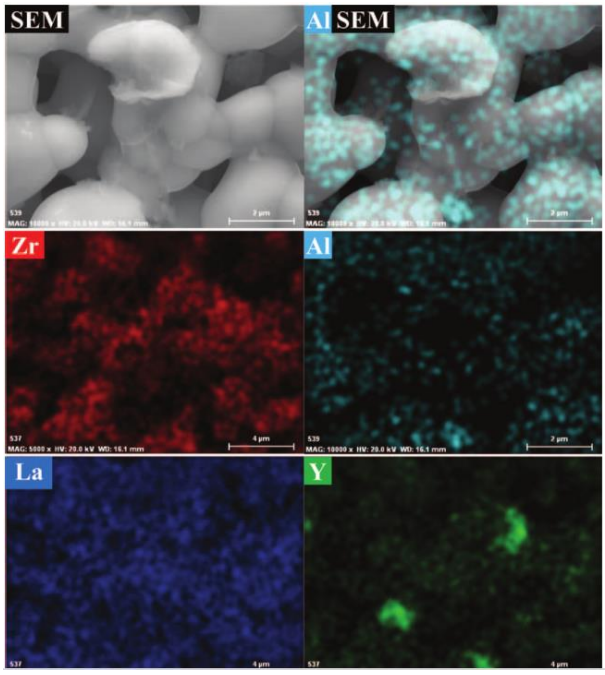

Figure 29. Elemental mapping of garnet-type 8 mol % YSZ–doped $Li_{7.16}La_3Zr_{1.84}Y_{0.16}O_{12}$ prepared at 950 °C in air.

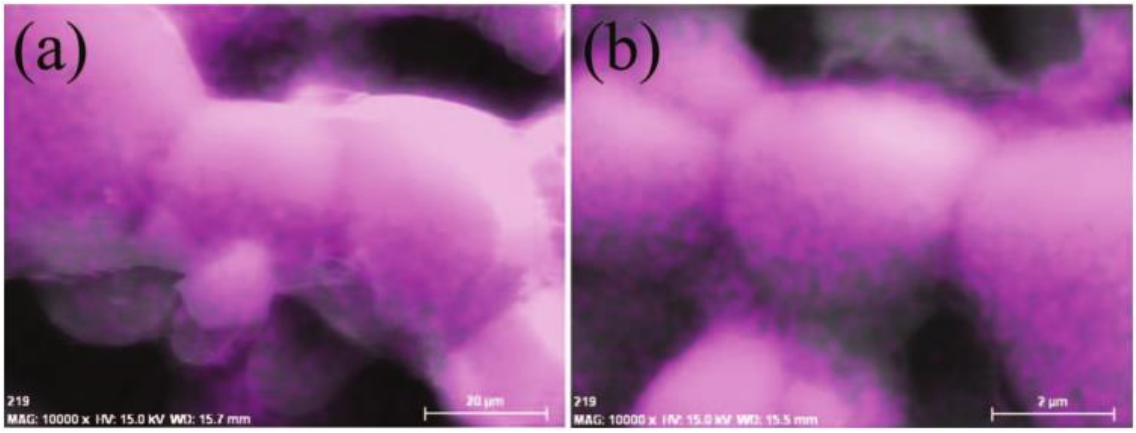

Figure 30. SEM images overlaid with EDS mappings of (a) $Li_{7.06}La_3Y_{0.06}Zr_{1.94}O_{12}$ (b) $Li_{7.16}La_3Y_{0.16}Zr_{1.84}O_{12}$ sintered at 1100 °C. These images show no evidence of Al segregation to the grain boundaries, however, rather uniform and more intense distribution of Al signal was observed compared to 950 ºC samples.

Typical AC impedance plots obtained at 100 °C in air using Ag electrodes are shown in Figure 31. At low temperature impedance plots can be resolved into bulk (R_{bulk}), grain-boundary (R_{gb}), and electrode ($R_{electrode}$) contribution to the total

conductivity. However, at high temperatures, we see mainly the bulk part and an electrode contribution. The presence of a low-frequency tail indicates that electrode and electrode interface is blocking for ions and electrons since Ag is a reversible electrode for electrons and blocking for Li ions. We have used a high-frequency intercept or minimum to real axis (R) to determine the electrical conductivity (σ) using the relationship: $\sigma = (1/R)(l/a)$ where l and a represent thickness and area of the investigated Li-stuffed samples, respectively.

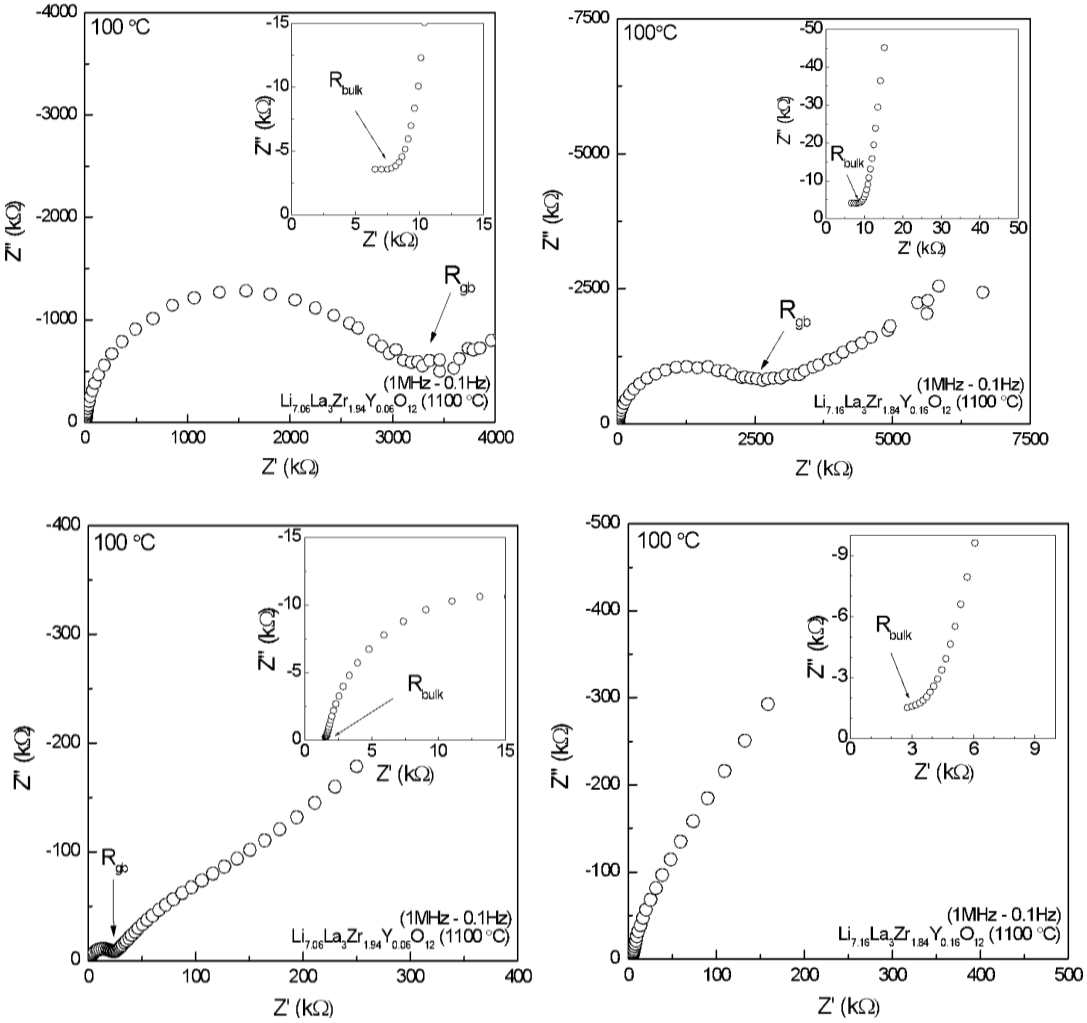

Figure 31. Typical AC impedance plots obtained at 100 °C in air using Ag electrodes (0.1 Hz to 1 MHz) for cubic garnet-type 3 mol% YSZ–doped

$Li_{7.06}La_3Zr_{1.94}Y_{0.06}O_{12}$, and 8 mol % YSZ–doped $Li_{7.16}La_3Zr_{1.94}Y_{0.06}O_{12}$. The inset shows the expanded high-frequency regime.

Figure 32 shows the electrical conductivity of $Li_{7.06}La_3Zr_{1.94}Y_{0.06}O_{12}$ (○) and $Li_{7.16}La_3Zr_{1.84}Y_{0.16}O_{12}$ (□), suggesting that Y-dopant does not play a major role on ionic conductivity. For comparison, we have included electrical conductivity of $Li_7La_3Zr_2O_{12}$ prepared by ceramic and wet-chemical methods in the literature[21,27,92,99–101]. Also, we measured the electrical conductivity of $Li_6La_2SrTa_2O_{12}$ (◊) prepared by the same ceramic method, as described in ref. 34, using Ag electrodes. The electrical conductivity of the $Li_6La_2SrTa_2O_{12}$ is found to be highly reproducible with Ag or Au electrodes, indicating no effect on Li ion conductivity due to the nature of the current collectors. Presently, investigated Li-stuffed Y-doped samples $Li_{7.06}La_3Zr_{1.94}Y_{0.06}O_{12}$ and $Li_{7.16}La_3Zr_{1.84}Y_{0.16}O_{12}$ show conductivity comparable to that of tetragonal polymorph (t-phase) of $Li_7La_3Zr_2O_{12}$ and activation energy for electrical conduction was found to be 0.47 eV and is consistent with low conducting t-phase. The electrical mobility and diffusion constant were calculated for Li^+ ions and listed in Table 3 together with other $Li_7La_3Zr_2O_{12}$ materials from literature. The calculated room temperature motilities are in the range of 10^{-8} – 10^{-11} cm^2/Vs for $Li_7La_3Zr_2O_{12}$ and diffusion constants are in the range of 10^{-9}-10^{-12} cm^2/Vs.

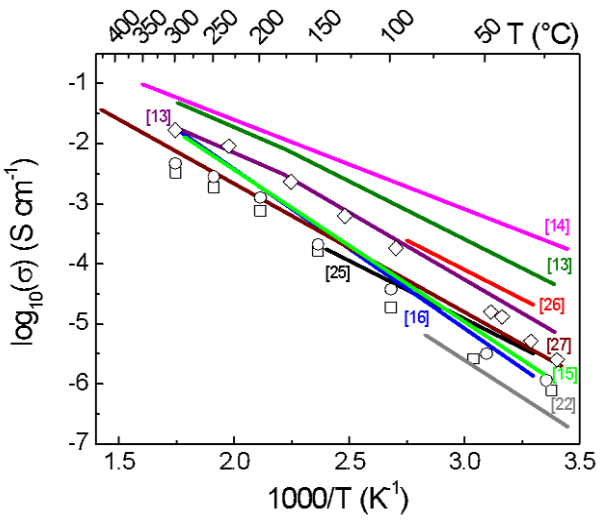

Figure 32. Arrhenius plots for Li ion conductivity of 3 mol% YSZ–doped $Li_{7.06}La_3Zr_{1.94}Y_{0.06}O_{12}$ (○) (present work), 8 mol % YSZ–doped $Li_{7.16}La_3Zr_{1.94}Y_{0.06}O_{12}$ (□) (present work), and $Li_6SrLa_2Ta_2O_{12}$ (◊) (present work). For comparison, we included ionic conductivity of cubic $Li_7La_3Zr_2O_{12}$ from refs. [21,96,99,101]***, tetragonal $Li_7La_3Zr_2O_{12}$ from refs. 27 and 92 and $Li_6ALa_2Ta_2O_{12}$ (A = Sr, Ba) from ref. 23. We see that low temperature prepared cubic $Li_7La_3Zr_2O_{12}$ shows about 2 orders of magnitude lower conductivity than the high temperature cubic phase.***

The electrical conductivity (σ) of solids can be expressed as $\sigma = nq\mu$, where n, q and μ represent concentration of mobile charge carriers, elementary charge, and electrical mobility respectively, and the latter depends on structure and disorder of the mobile ion sublattice[102]. As the charge carriers, the Li ions in the garnet-type structure are distributed at tetrahedral (24d), octahedral (48g) and distorted octahedral (96h) sites in the cubic space group, *Ia-3d* [30,103]. None of these Li ion sites are completely filled for any known Li-stuffed garnets, including $Li_5La_3M_2O_{12}$ (M = Nb, Ta), $Li_6ALa_2M_2O_{12}$ (A = alkaline earth ions; M = Nb,Ta) and $Li_7La_3C_2O_{12}$ (C = Sn, Zr). Hence, all of these Li sites can contribute to ionic conduction, and relative contribution from each site is not yet known. Several authors observed that the ionic

conductivity increases with increasing Li content in Li-stuffed garnets and excess Li ions seems to populate the octahedral sites. The optimum concentration of Li for high ionic conduction was found to be close to 6.4[30]. However, the effect of particle size, lattice parameter and polymorph cannot be eliminated using this empirical approach. For example, cubic $Li_7La_3Zr_2O_{12}$ prepared at low temperatures shows about two to three orders of magnitude lower conductivity than high temperature cubic phase which seems to be related to poor density of the low-temperature modification[27]. It has been reported that bulk ionic conductivity of $Li_7La_3Zr_2O_{12}$ can vary about two orders of magnitude due to sample density between 60 and 98% theoretical[100]. Future work will focus on densifying Y-substituted Li-garnets, $Li_{7.06}La_3Zr_{1.94}Y_{0.06}O_{12}$ and $Li_{7.16}La_3Zr_{1.84}Y_{0.16}O_{12,}$ to improve conductivity.

In order to further understand the low ionic conductivity of cubic $Li_{7.06}La_3Zr_{1.94}Y_{0.06}O_{12}$ and $Li_{7.16}La_3Zr_{1.84}Y_{0.16}O_{12}$, we performed Raman spectroscopy and results are shown in Figure 33. The Raman spectra for the Y-doped garnets prepared at 1100 °C show very similar patterns to the pattern given in literature for cubic $Li_7La_3Zr_2O_{12}$[28]. Samples synthesized at 950 °C show splitting of the cubic peaks, and are similar to the literature for tetragonal $Li_7La_3Zr_2O_{12}$[28]. However, X-ray diffraction shows $Li_{7.06}La_3Zr_{1.94}Y_{0.06}O_{12}$ and $Li_{7.16}La_3Zr_{1.84}Y_{0.16}O_{12}$ to be cubic while Raman spectra seem to show an ordered tetragonal $Li_7La_3Zr_2O_{12}$. Further investigation of this phenomenon may help to understand the lower conductivity of cubic $Li_7La_3Zr_2O_{12}$ processed at low temperatures in the literature[96,99].

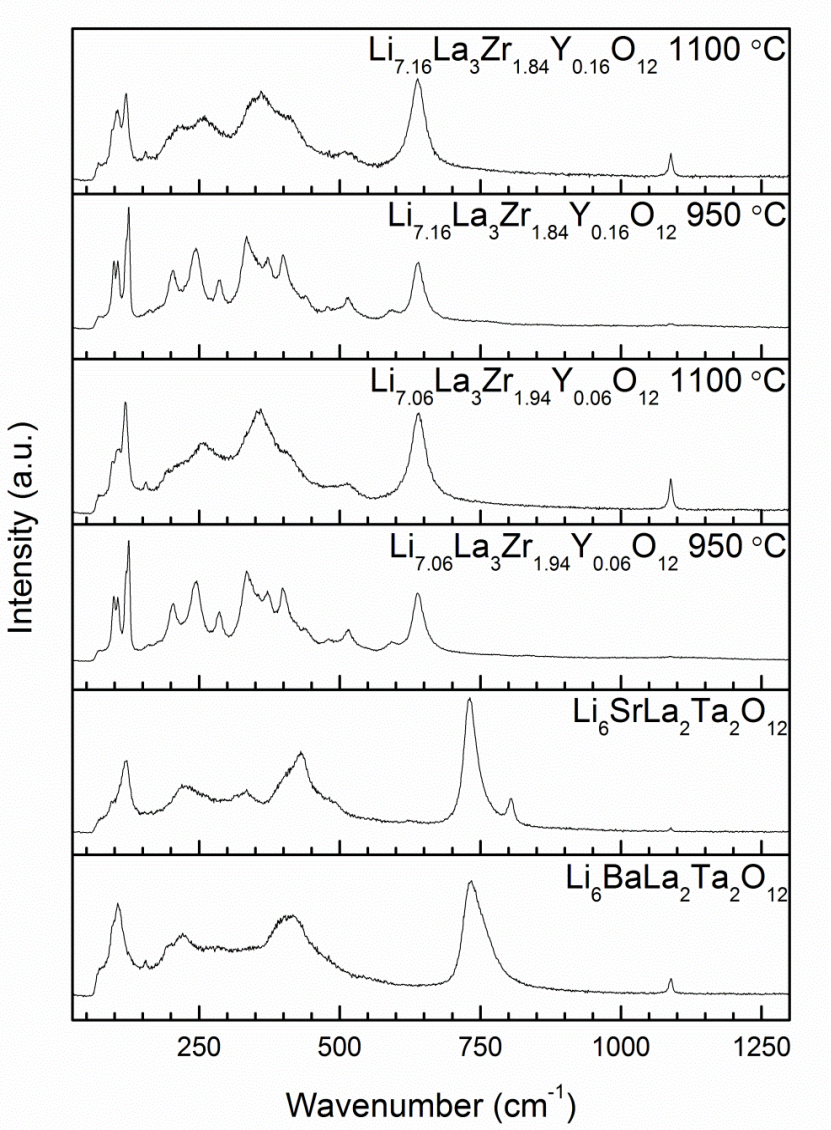

Figure 33. Raman spectra for as-prepared powdered 3 mol % YSZ–doped $Li_{7.06}La_3Zr_{1.94}Y_{0.06}O_{12}$, and 8 mol % YSZ–doped $Li_{7.16}La_3Zr_{1.84}Y_{0.16}O_{12}$. For comparison, we also included Raman spectra of highly conducting cubic garnet-type $Li_6La_2ATa_2O_{12}$ (A = Sr, Ba).

3.4 - Conclusions

In summary, single-phase garnet Li-stuffed metal oxides with nominal chemical formulae of $Li_{7.06}La_3Zr_{1.94}Y_{0.06}O_{12}$ and $Li_{7.16}La_3Zr_{1.84}Y_{0.16}O_{12}$ was prepared by ceramic reaction at 950 °C in air. A garnet-type cubic cell constant of 12.974(3) Å and 12.995(2) Å was obtained from PXRD for $Li_{7.06}La_3Zr_{1.94}Y_{0.06}O_{12}$ and $Li_{7.16}La_3Zr_{1.84}Y_{0.16}O_{12}$, respectively. An increase in cubic cell constant is consistent with Y-substitution for Zr in $Li_7La_3Zr_2O_{12}$. SEM studies showed an average crystallite size in the range of 2-5µm, and particle size increases with increasing sintering temperature and backscattered SEM and energy dispersive spectroscopy (EDS) elemental mapping show single homogenous distribution of electron density and homogeneous distribution of elements, respectively, for samples prepared at 950 °C. Electrochemical AC impedance spectra exhibit mainly bulk contribution at temperatures higher than 150 °C, and at low temperature we see contributions from bulk and grain-boundary resistance. The bulk electrical conductivity of the sample was found to comparable to those of the high temperature tetragonal phase. The electrical conductivity of both Y members investigated in the present work were 10^{-6} S/cm at room temperature with an activation energy of 0.47 eV. The lower conductivity of this garnet-type phase was explained using the Raman spectra. The Raman spectrum of cubic garnet seems to match with the tetragonal spectra for $Li_7La_3Zr_2O_{12}$.

Chapter 4: Design of a Solid State Battery

As discussed in the introduction, lithium metal battery technology has the highest volumetric and gravimetric energy density compared to all other rechargeable batteries (Figure 1a), making it the prime candidate for a wide range of applications, from portable electronics to electric vehicles (EVs). However, true deployment of this technology requires the use of scalable, high cathode loading solid state batteries.

Due to the ceramic powder nature of Li-garnets, solid state batteries can be fabricated using conventional solid oxide fuel cell (SOFC) fabrication techniques. This has tremendous advantages in terms of both cost and performance. All the fabrication processes can be done with conventional ceramic processing equipment in ambient air without the need of dry rooms, vacuum deposition, or glove boxes, dramatically reducing cost of manufacturing.

As mentioned in the introduction, all of the solid state batteries investigated to date suffer from high interfacial impedance due to their low surface area, planar electrode/electrolyte interfaces. This problem was previously addressed in the development of higher power density SOFCs. Low ASR cathodes and anodes are now common in state-of-the-art SOFCs and were achieved by integration of electronic and ionic conducting phases to increase triple-phase boundary area and extend the electrochemically active region farther from the electrolyte/electrode planar interface. Dr. Wachsman has done extensive work in this area[104–107] and by simple modification of the microstructure of the electrolyte/electrode interface have been able to reduce overall cell ASR by 3X and increase exchange current density by

4X, resulting in a 4X increase in SOFC power density for identical composition and layer thickness cells[104].

These same advances can be applied to solid state batteries to decrease solid state battery interfacial impedance. Tape casting can be used for low-cost, high-speed, scalable multi-layer ceramic processing to fabricate supported thin-film (~10μm) SSEs on tailored microstructured electrode scaffolds. Layers can be tape cast between 10 and several hundred μm with microstructural features tailored to meet design parameters for surface area, porosity, and cathode loading. After tape casting, layers are laminated, cut to size and sintered. Electrodes can be filled in to create the final battery structure. All of these methods are roll-to-roll processes which are already scaled up for other systems.

4.1 - Battery Design

The structure shown in Figure 34 allows for significant loading of active cathode material and a high interfacial surface area. Porogen content, size and distribution can be optimized to the cathode size and capacity. Electrode layer thickness will allow electrode capacity matching.

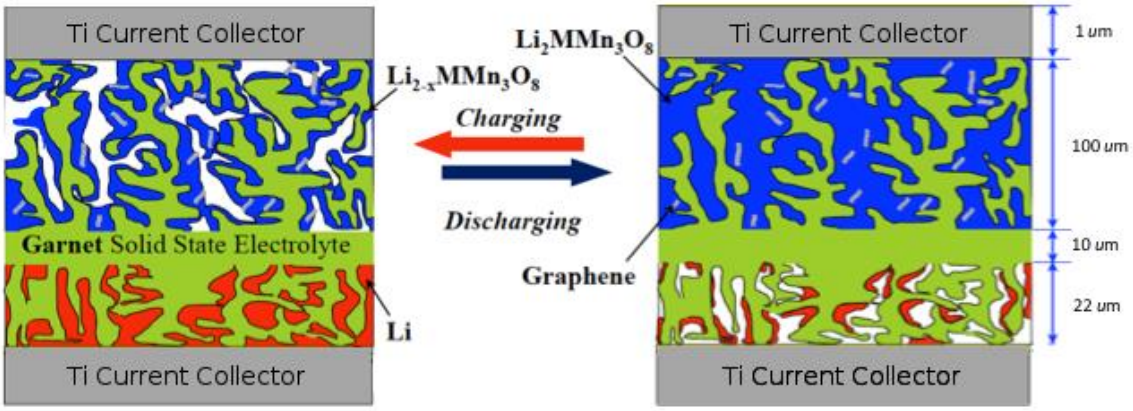

Figure 34. Diagram of designed battery structure.

A major advantage of this structure is that charge/discharge cycles will involve filling/emptying of the SSE scaffold pores, rather than intercalating and expanding carbon anode powders/fibers. As a result there will be no change external dimensions between charged and discharged state. This will remove both cycle fatigue and limitations on depth of discharge, the former allowing for greater cycle life and the later for greater actual battery capacity.

Moreover, the zero external expansion allows for the batteries to be stacked as a structural unit. Light-weight, Li-impervious titanium will serve as current collectors. It can be deposited in a thin layer for maximum energy density or a Ti foil (20-4o0 μm thick) can be used to provide mechanical strength. A thick stack of titanium and garnet ceramic will create a strong structure. EV motors require high voltage input (Tesla's Model S requires 375V), which would be somewhat thicker than a 1 cm stack of these cells. Such a strong, thick stack could be used as protective or structural components of a vehicle, as depicted in Figure 35.

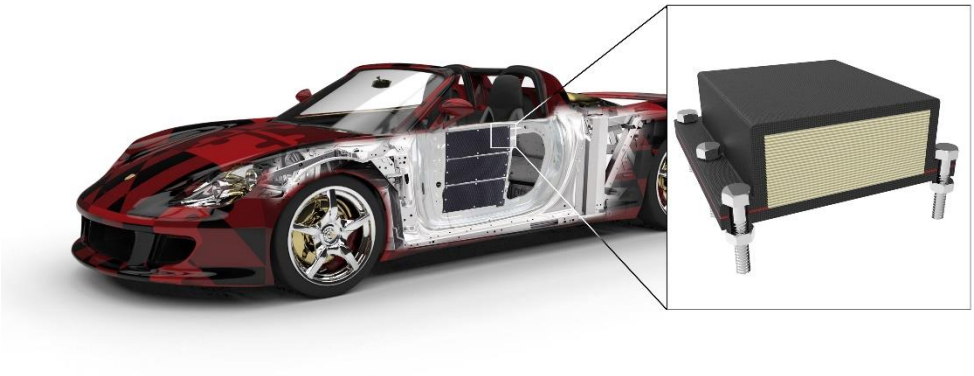

Figure 35. Artist's rendition of lithium-garnet batteries as protective component in an electric vehicle.

For this all solid-state battery with no SEI or other performance degradation mechanisms inherent in liquid electrolyte cells, the calendar life could greatly exceed current state-of-art Li-batteries. This general structure is advantageous independent of material set. This system was designed for use with a lithium garnet electrolyte, lithium metal anode, and a lithium transition-metal oxide cathode. Other electrode chemistries such as a sulfur cathode or graphite anode also benefit from the zero external expansion, low self-discharge of the electrolyte, intrinsic safety, and high inherent strength. Other electrolyte materials can also be used, such as a NASICON electrolyte for use with sodium-based electrodes, adding these advantages to a low cost sodium-based materials set.

For energy density predictions, a voltage of 4.55 V is being used, which is the average of the 5.0 V and 4.1 V plateaus measured in UMERC's current state-of-the-art $Li_2FeMn_3O_8$ cathode with a measured capacity of 135 mAh/g. The energy density calculations resulting from this structure are summarized in Table 5 and will be

calculated in the following section.

Average cell voltage	4.55 V
Specific capacity	65.9 Ah/kg
Volumetric	237.0 Ah/L
Energy density (mass)	300.0 Wh/kg
Energy density (volume)	1,078.3 Wh/L

Table 5. Energy density calculations.

4.2 Material Cost Estimation

In order to predict the cost of the device it is necessary to calculate the required materials per kWh and establish an expected bulk price of raw materials. Bulk material prices for the required elements were researched and are given in Table 6. The prices in this chart assume large orders and will be achievable only after production scale-up. These prices do not include ancillary materials such as milling media for grinding or isopropanol and toluene for tapecasting, as the use of these materials would not scale linearly with higher production.

Material	Purity	Price per kg	Vendor/source
$CaCO_3$	99.5 %	$2.50	Baicheng Chemical Co.
Carbon additive	-	$2.40	SidRichardson Carbon & Energy Co.
Fe_2O_3	99.5 %	$0.99	Wanshida Chemical Co.
La_2O_3	99.5 %	$5.10	Anhui Herrman Impex Co.
Li_2CO_3	99.5 %	$7.25	Baijierui Advanced Materials Corporation
Li metal	-	$66.61 (market price)	metalprices.com
MnO_2	99.9 %	$2.00	Xiamen Tob New Energy Technology Co.
Nb_2O_5	99.5 %	$36.00	Hefei Toplus Impex Co.
Sulfur	99.9%	$0.16	Hezhou City Yaolong Trade Co.
Ti metal	-	$4.30 (market price)	metalprices.com
ZrO_2	99.5 %	$6.00	Changsha Zhonglong Chemical Co.

Table 6. Table showing bulk prices and suppliers for the materials required in the fabrication of a lithium garnet solid state battery.

These materials will be used to form the main starting materials of the battery: $Li_2FeMn_3O_8$ (LFMO) for cathode and $Li_7La_{2.75}Ca_{0.25}Zr_{1.75}Nb_{0.25}O_{12}$ (LLCZN) for electrolyte. Table 7 shows the cost calculation of the raw materials required for the synthesis of LLCZN, without regard for equipment costs, power usage, or any other associated costs. The calculation scales the stoichiometry of the material to 1 kg of final product using the molar mass, 815.5 g/mol. The proper amount of starting material is calculated and converted to mass with the molar masses of the starting materials. This is then multiplied by the price per kg found previously and a raw material price per kg is found. These prices sum to the total cost of raw materials to synthesize 1 kg of LLCZN, $7.74/kg. This calculation does not take into account excess lithium added to compensate for loss during sintering. With the current procedure of adding 10% excess Li_2CO_3, this would add $0.18 per kg of LLCZN. Other than lithium, all materials are assumed to remain in the final product at 100% yield.

	Stoich. (mol)	Scaled to 1 kg LLCZN (mol)	Rawmat	Rawmat moles (mol)	Molar mass	Rawmat mass (g)	Price of rawmat ($/kg)	Price for 1 kg LLCZN ($/kg)
Li	7	8.58	Li_2CO_3	4.29	73.89	317.13	$5.71	$1.81
La	2.75	3.37	La_2O_3	1.69	325.82	549.38	$5.10	$2.80
Ca	0.25	0.31	$CaCO_3$	0.31	100.09	30.68	$2.50	$0.08
Zr	1.75	2.15	ZrO_2	2.15	123.22	264.44	$6.00	$1.59
Nb	0.25	0.31	Nb_2O_5	0.15	265.81	40.75	$36.00	$1.47
O	12	-	-	-	-	-	-	-
							Total	$7.74

Table 7. Table showing the calculation of material costs for synthesis of 1 kg of $Li_7La_{2.75}Ca_{0.25}Zr_{1.75}Nb_{0.25}O_{12}$.

The same calculation is performed in Table 8 for LFMO which has a molar mass of 362.5 g/mol. While in reality, LFMO is currently produced via glycine nitrate combustion requiring metal nitrates, this calculation is performed using the initial oxides as reasonable analogues. Oxides were used in this calculation due to difficulty in finding prices of bulk scale nitrates at sufficient purity. With this calculation, the expected cost of LFMO is $6.86/kg.

	Stoich. (mol)	Scaled to 1 kg LFMO (mol)	Rawmat	Rawmat moles (mol)	Molar mass	Rawmat mass (g)	Price of rawmat ($/kg)	Price for 1 kg LLCZN ($/kg)
Li	2	5.52	Li_2CO_3	5.52	3.89	407.62	$5.71	$2.33
Fe	1	2.76	Fe_2O_3	1.38	159.69	220.24	$0.99	$0.22
Mn	3	8.28	MnO_2	24.83	86.94	2158.23	$2.00	$4.32
O	8	-	-	-	-	-	-	-
							Total	$6.86

Table 8. Table showing the calculation of material costs for synthesis of 1 kg of $Li_2FeMn_3O_8$

The cell design will determine the amount of each material required in the fabrication of the device. Table 9 shows the calculation for the energy density and mass of materials required for a single 10x10 cm cell. While a 10x10cm may not be the ultimate cell size, the stored energy and materials required will scale with area and the size of an individual cell will cancel out when determining the cost of 1 kWh.

	Material	Volume ratio	Volume (cm^3)	Density (g/cm^3)	Mass (g)	Specific Capacity (mAh/g)	Capacity (mAh)
Cathode	Garnet	30%	0.300	4.97	1.491	0	0.0
100 um	LFMO	65%	0.650	3.59	2.334	135	315.0
	Carbon	5%	0.050	1.7	0.085	0	0.0
	Empty	0%	0.000	0	0.000	0	0.0
Electrolyte	Garnet	100%	0.100	4.97	0.497	0	0.0
10 um							
Anode	Garnet	30%	0.066	4.97	0.327	0	0.0
21.9 um	Lithium	0%	0.000	0.54	0.000	3,800	0.0
	Empty	70%	0.154	0	0.000	0	0.0
Current collector	Titanium	100%	0.010	4.5	0.045	0	0.0
1 um							
		Totals:	1.329		4.78		315.0
						Energy	300.0 Wh/kg
						Density	1,078.3 Wh/L

Table 9. Cell design for Li-LFMO battery showing the required mass for each component.

At an average voltage of 4.55 V (with a plateau at 5.0V and 4.1V), this cell will have 1.43 Wh/cell. This system will require 698 cells to store 1 kWh. Table 10 shows the calculation for the total device cost for a 1 kWh system, excluding packaging and associated costs.

Material	Mass per 10 x 10 cm cell (g)	Mass for 1 kWh (kg)	Unit Cost ($/kg)	Price per kWh ($)
SSE - LLCZN	2.32	1.60	$7.92	$12.80
Cathode - LFMO	2.33	1.63	$6.86	$11.17
Conductive Carbon	0.09	0.06	$2.40	$0.14
Ti	0.05	0.03	$4.30	$0.14
Total	4.8	3.34		$24.25

Table 10. Cost calculation for Li-LFMO cell.

The versatility of our new scaffold also opens the possibility for other cathodes to be used. A lithium-sulfur system was also modeled with the same calculations as above and is shown in Table 11. Empty space was given for expansion of the sulfur cathode upon discharging, as well as extra conductive additive to compensate for the low electronic conductivity of sulfur. Because sulfur is not a lithium source, lithium metal is also included as a starting component.

	Material	Volume ratio	Volume (cm^3)	Density (g/cm^3)	Mass (g)	Specific Capacity (mAh/g)	Capacity (mAh)
Cathode	Garnet	30%	0.300	4.97	1.491	0	0.0
100 um	Sulfur	40%	0.400	1.96	0.784	1,675	1,313.2
	Carbon	10%	0.100	1.7	0.170	0	0.0
	Empty	20%	0.200	0	0.000	0	0.0
Electrolyte	Garnet	100%	0.100	4.97	0.497	0	0.0
10 um							
Anode	Garnet	30%	0.274	4.97	1.363	0	0.0
91.4 um	Lithium	70%	0.640	0.54	0.346	3,800	1,313.2
	Empty	0%	0.000	0	0.000	0	0.0
Current collector	Titanium	100%	0.010	4.5	0.045	0	0.0
1 um							
		Totals:	2.024		4.70		1,313.2
						Energy	587.3 Wh/kg
						Density	1,362.4 Wh/L

Table 11. Cell design for Li-S battery showing the required mass for each component.

At an average voltage of 2.1 V, this cell will have 2.76 Wh/cell. This system will require 363 cells to store 1 kWh. Table 12 shows the calculation for the total device cost for a 1 kWh system, excluding packaging and associated costs.

Material	Mass per 10 x 10 cm cell (g)	Mass for 1 kWh (kg)	Unit Cost ($/kg)	Price per kWh ($)
SSE - LLCZN	3.35	1.22	$7.52	$9.63
Li metal	0.35	0.13	$66.60	$8.35
Cathode -Sulfur	0.78	0.28	$0.16	$0.05
Conductive Carbon	0.17	0.06	$2.40	$0.15
Ti	0.05	0.02	$4.30	$0.07
Total	4.70	1.70		$18.25

Table 12. Cost calculation for Li-S cell.

On a raw materials-basis, Garnet batteries will easily achieve the $100/kWh goal set by ARPA-e. Li-LFMO and Li-S batteries based on this technology will cost $24.25 and $18.25, respectively. While this does not including packaging or processing costs, it does allow a significant amount of room, more than quadrupling the desired economic energy density.

4.3 - Selection of commercially available cathodes

In the Li-LFMO cell, we showed that the cathode comprises nearly 46% of the total cost of the cell ($11.17 cathode cost out of $24.25/kWh). This indicates that the overall cost of the battery will be very sensitive to the cost and performance of the cathode. Potential cathodes investigated include $LiCoO_2$ (LCO), $LiNi_{1/3}Mn_{1/3}Co_{1/3}O_2$ (NMC), and $LiNi_{0.8}Co_{0.15}Al_{0.05}O_2$ (NCA). Shown in Table 13, cathode capacities and voltages used in energy density calculations were taken from Chapter 2 of "Batteries for Sustainability" written by Marca Doeff published in 2013.

Material	Purity	Price per kg	Vendor/source	Voltage (V)	Capacity (mAh/g)
$LiCoO_2$	> 98%	$15.00	Linyi Gelon LIB	3.9	140
$LiNi_{1/3}Mn_{1/3}Co_{1/3}O_2$	-	$20.00	Xiamen Tob New Energy Technology	3.8	170
$LiNi_{0.8}Co_{0.15}Al_{0.05}O_2$	99.9 %	$30.00	Linyi Gelon LIB	3.8	200

Table 13. Table showing bulk prices and suppliers for commercially available cathodes for use in a lithium garnet solid state battery.

Energy density and cost calculations were performed according to the same procedures as above for LFMO and sulfur. As with sulfur and LFMO, a cathode layer thickness of 100 um was chosen to enable high performance and anode thickness was calculated to match the capacity. It is possible that this thickness can be increased significantly beyond this for higher energy density, but optimization of layer thickness is required before making this determination. Table 14 shows the energy density calculation for a Li-LCO cell.

	Material	Volume ratio	Volume (cm^3)	Density (g/cm^3)	Mass (g)	Specific Capacity (mAh/g)	Capacity (mAh)
Cathode	Garnet	30%	0.300	4.97	1.491	0	0.0
100 um	LCO	65%	0.650	3.59	2.334	140	326.7
	CNT	5%	0.050	1.7	0.085	0	0.0
	Empty	0%	0.000	0	0.000	0	0.0
Electrolyte	Garnet	100%	0.100	4.97	0.497	0	0.0
10 um							
Anode	Garnet	30%	0.068	4.97	0.339	0	0.0
22.7 um	Lithium	0%	0.000	0.54	0.000	3,800	0.0
	Empty	70%	0.159	0	0.000	0	0.0
Current collector	Titanium	100%	0.010	4.5	0.045	0	0.0
1 um							
		Totals:	1.337		4.79		326.7
						Energy	266.0 Wh/kg
						Density	952.6 Wh/L

Table 14. Cell design for Li-LCO battery showing the required mass for each component.

At a voltage of 3.9 V, this cell will have 1.27 Wh/cell. This system will require 785 cells to store 1 kWh. Table 15 shows the calculation for the total device cost for a 1 kWh system, excluding packaging and associated costs.

Material	Mass per 10 x 10 cm cell (g)	Mass for 1 kWh (kg)	Unit Cost ($/kg)	Price per kWh ($)
SSE - LLCZN	2.33	1.83	$7.92	$14.47
Cathode - LCO	2.33	1.83	$15.00	$27.48
Conductive Carbon	0.09	0.07	$2.40	$0.16
Ti	0.05	0.04	$4.30	$0.15
Total	4.8	3.76		$42.26

Table 15. Cost calculation for a Li-LCO cell.

The cell design for a Li-NMC cell is given in Table 16.

	Material	Volume ratio	Volume (cm3)	Density (g/cm3)	Mass (g)	Specific Capacity (mAh/g)	Capacity (mAh)
Cathode	Garnet	30%	0.300	4.97	1.491	0	0.0
100 um	NMC	65%	0.650	3.59	2.334	170	396.7
	CNT	5%	0.050	1.7	0.085	0	0.0
	Empty	0%	0.000	0	0.000	0	0.0
Electrolyte	Garnet	100%	0.100	4.97	0.497	0	0.0
10 um							
Anode	Garnet	30%	0.083	4.97	0.412	0	0.0
27.6 um	Lithium	0%	0.000	0.54	0.000	3,800	0.0
	Empty	70%	0.193	0	0.000	0	0.0
Current collector	Titanium	100%	0.010	4.5	0.045	0	0.0
1 um							
		Totals:	1.386		4.86		396.7
						Energy	310.0 Wh/kg
						Density	1,087.5 Wh/L

Table 16. Cell design for Li-NMC battery showing the required mass for each component.

At a voltage of 3.8 V, this cell will have 1.51 Wh/cell. This system will require 664 cells to store 1 kWh. Table 17 shows the calculation for the total device cost for a 1 kWh system, excluding packaging and associated costs.

Material	Mass per 10 x 10 cm cell (g)	Mass for 1 kWh (kg)	Unit Cost ($/kg)	Price per kWh ($)
SSE - LLCZN	2.40	1.59	$7.92	$12.62
Cathode - NMC	2.33	1.55	$20.00	$30.99
Conductive Carbon	0.09	0.06	$2.40	$0.14
Ti	0.05	0.03	$4.30	$0.13
Total	4.9	3.23		$43.87

Table 17. Cost calculation for a Li-NMC cell.

The cell design for a Li-NCA cell is given in Table 18.

	Material	Volume ratio	Volume (cm^3)	Density (g/cm^3)	Mass (g)	Specific Capacity (mAh/g)	Capacity (mAh)
Cathode	Garnet	30%	0.300	4.97	1.491	0	0.0
100 um	NCA	65%	0.650	3.59	2.334	200	466.7
	CNT	5%	0.050	1.7	0.085	0	0.0
	Empty	0%	0.000	0	0.000	0	0.0
Electrolyte	Garnet	100%	0.100	4.97	0.497	0	0.0
10 um							
Anode	Garnet	30%	0.097	4.97	0.484	0	0.0
32.5 um	Lithium	0%	0.000	0.54	0.000	3,800	0.0
	Empty	70%	0.227	0	0.000	0	0.0
Current collector	Titanium	100%	0.010	4.5	0.045	0	0.0
1 um							
		Totals:	1.435		4.94		466.7
						Energy	359.3 Wh/kg
						Density	1,235.9 Wh/L

Table 18. Cell design for Li-NCA battery showing the required mass for each component.

At a voltage of 3.8 V, this cell will have 1.77 Wh/cell. This system will require 564 cells to store 1 kWh. Table 19 shows the calculation for the total device cost for a 1 kWh system, excluding packaging and associated costs.

Material	Mass per 10 x 10 cm cell (g)	Mass for 1 kWh (kg)	Unit Cost ($/kg)	Price per kWh ($)
SSE - LLCZN	2.47	1.39	$7.92	$11.04
Cathode - NCA	2.33	1.32	$30.00	$39.48
Conductive Carbon	0.09	0.05	$2.40	$0.12
Ti	0.05	0.03	$4.30	$0.11
Total	4.9	2.78		$50.75

Table 19. Cost calculation for a Li-NCA cell.

4.4 - Process Timeline

The time required for each step within each operation in the process is given in Figure 36. Operations are shown vertically and are proportional to their total time. Operations A and B, in red, are materials synthesis steps. This process diagram describes the solid state synthesis of garnet and the glycine nitrate synthesis of LFMO cathode. Operations C and D, shown in green, detail the steps required for tapecasting. Operation E, in blue, is the preparation of the tapes for sintering. Operation F, in orange, details the sintering conditions for the garnet. Fabrication of the cell occurs in operation G, shown in pink. Expanded from the operations are the individual steps. The step sizes are proportional to other steps within an operation, depending on the time required for completion. Steps within an operation are shown from the first step at top to the last step at bottom, matching up with the steps listed under the operation heading.

A. Electrolyte material synthesis (73 hr)

A1. Mix materials (1 hr)
A2. Ball mill in IPA (24 hr)
A3. Dry milled material (6 hr)
A4. Calcine 900 °C, 5 °C/min ramp (12 hr)
A5. Ball mill in IPA (24 hr)
A6. Dry milled material (6 hr)

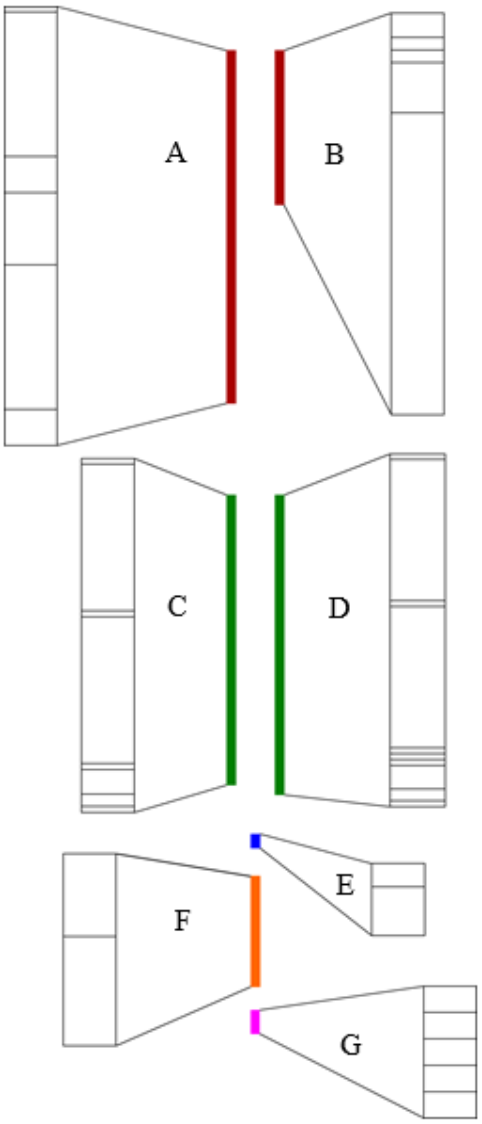

Figure 36. Operations diagram for lithium garnet battery fabrication.

B. Cathode material synthesis (32 hr)

B1. Mix and dissolve reactants in H_2O (1 hr)
B2. Heat solution to 300 °C until ignition (2 hr)
B3. Collect product and move to crucible (1 hr)
B4. Anneal material 700 °C, 10 °C/min ramp (4 hr)
B5. Ball mill in IPA (24 hr)

C. Dense tape fabrication (58 hr)

C1. Mix tape Day 1 materials (1 hr)
C2. Ball mill in IPA (24 hr)
C3. Mix tape Day 2 materials (1 hr)
C4. Ball mill in IPA (24 hr)
C5. Remove slurry for tapecasting (1 hr)
C6. De-gas slurry (4 hr)
C7. Tapecast slurry (2 hr)
C8. Tape drying and storage (1 hr)

D. Porous tape fabrication (60 hr)

D1. Mix tape Day 1 materials (1 hr)
D2. Ball mill in IPA (24 hr)
D3. Mix tape Day 2 materials (1 hr)
D4. Ball mill in IPA (24 hr)
D5. Add PMMA pore former (1 hr)
D6. Ball mill 1 hour (1 hr)
D7. Remove slurry for tapecasting (1 hr)
D8. De-gas slurry (4 hr)
D9. Tapecast slurry (2 hr)
D10. Tape drying and storage (1 hr)

E. Tape lamination

E1. Press 3 layers of tape at 3 metric tons for 30 minutes (1 hr)
E2. Punch button cells (2 hr)

F. Fabrication of SSE

F1. Pre-sinter on Al_2O_3 plate in O_2 – 200C (30 min), 450C (30 min), 650C (4 hr) ramping at 3C/min (10 hr)
F2. Place pre-sintered cells in powderbed in alumina crucible then sinter at 950C (5 hr) ramping at 3C/min (13 hr)

G. Fabrication of cell

G1. Infiltrate cathode and CNTs (1 hr)
G2. ALD of Al_2O_3 to protect interface (1 hr)
G3. Electron beam deposition of Ti current collector onto cathode side (1 hr)
G4. Melt lithium into anode side with slight excess of lithium (1 hr)
G5. Make stack by melting excess lithium on anode side to Ti on cathode side 300 °C (1 hr)

For the purposes of estimating a completion time for the entire cell, many of these operations can be performed simultaneously. The flow diagram in Figure 37 shows which operations, labeled with the same letter as in Figure 36, depend upon the completion of others and which can be completed simultaneously.

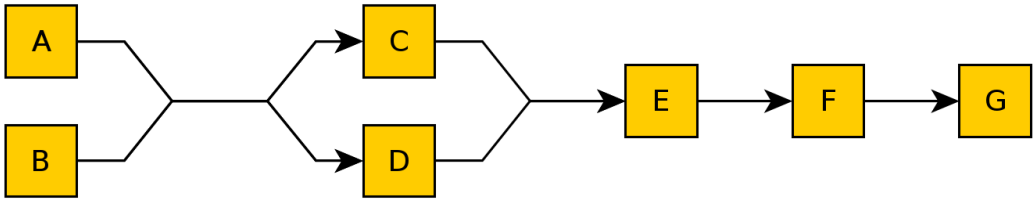

Figure 37. Flow diagram of operations showing which can be accomplished in parallel or series. Operations are A. Electrolyte material synthesis, B. Cathode material synthesis, C. Dense tape fabrication, D. Porous tape fabrication, E. Preparation of triple layer green tape, F. Fabrication of SSE, G. Fabrication of cell.

The total time to complete a batch of cells is the sum of the longest operation in each stage, operations A, D, E, F, and G. This indicates a required time of 167 hours to complete a batch of cells. A significant fraction of this time (48 hours) is ball milling of materials, which may be able to be reduced via future studies of high energy milling or nanopowder synthesis.

4.5 - Process Cost Estimation

In the effort to estimate process costs at scale, previous work in solid oxide fuel cells (SOFC's) is especially useful. The process of SOFC production is very similar to that of our batteries. SOFC unit operations in common with battery

fabrication include powder prep, tape casting, calendering/lamination, sintering, and quality control. Additionally, our battery fabrication includes cathode infiltration, ALD, Li infiltration, and packaging. Costs for all operations will be estimated.

Process cost is very dependent upon scale. For the purpose of this calculation, a scale of 5 million 10x10cm cells (equating to a total of 7.55 MWh) per year is used. This scale is chosen to correspond to an equivalent surface area of ceramic production as is used in Arthur D. Little's SOFC cost analysis (http://www.netl.doe.gov/publications/proceedings/01/seca/adlstack.pdf). Little's analysis includes manufacturing externalities such as worker wages, price of production space, cost of electricity and machinery depreciation. Little's initial assumptions are given in Table 20. Because Little's numbers are used for unit operation costs in many of our operations, these also represent our assumptions. While this analysis offers some estimate for scaled process cost, a yearly production of 7.55 MWh represents only moderate production levels of around 100 battery systems for Tesla Model S vehicles. For perspective, to benefit fully from economy of scale, the new Tesla Gigafactory will produce 35 GWh/year, about 4600 times this production rate.

Production Volume	250	MW/year
Designed Fuel Cell Output	25	kW
Size of Tile	100	cm^2
% Active Area per Tile	100%	
Power Density	500	mW/cm^2
Tile Pitch	5	Tiles/inch
Ceramic Furnace Packing Factor	5%	
Interconnect Brazing Packing Factor	80%	
Indirect Salary	35000	$/year
Direct Wages	14	$/hour
Benefits on Wage and Salary	35%	
Indirect:Direct Labor Ratio	1	
Working Days per Year	300	
Working Hours per Day	24	
Capital Recovery Rate	15%	
Working Capital Period	3	months
Price of Production Space	580	$\$/m^2$
Price of Electricity	$0.08	/kWh
Auxiliary Equipment Cost	80%	
Equipment Installation Cost	80%	
Maintenance Cost	4%	
Product Life	10	yrs
Tool Life	10	yrs
Equipment Recovery Period	10	yrs
Building Recovery Period	20	yrs

Table 20. Arthur D. Little baseline manufacturing assumptions.

The costs for each unit operation including overhead in Little's SOFC analysis and the estimated cost for battery production are given in Figure 38. Little normalizes costs to square meters of cells produced, which is a convenient metric as, for the most part, the cost involved in these processes is not material or application dependent. That means for a similar process, Little's analysis holds for solid state battery production as well. The costs for each unit op will be discussed in more detail. For any operations in which cathode type is important, an NCA cathode has been assumed.

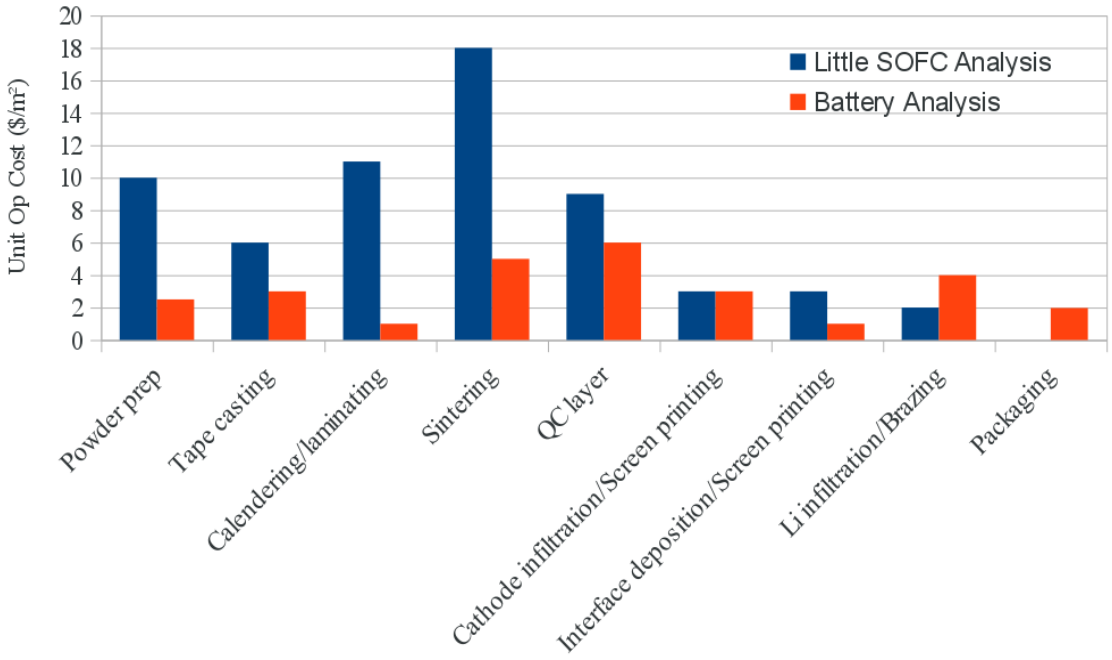

Figure 38. Cost estimate of unit ops for SOFC and battery production.

4.5.1 - Powder preparation

(Unit Op Cost: $2.5/m^2)

Powder preparation should be a similar cost between SOFC's and batteries per gram. While the calcination temperature for SOFC materials is usually somewhat higher than batteries, the overall procedure is quite similar. However, because SOFC's are less porous than our batteries and about three times thicker (~500 um vs ~150 um), less than one third of the powder is required per square meter. Therefore a little less than one third of Little's $10/m^2 price is used, $2.5/m^2.

4.5.2 - Tape casting

(Unit Op Cost: $3/m^2)

The tape casting process is very similar between SOFC's and batteries. However, SOFC's often consist of 4-5 layers: cathode, electrolyte bilayer, anode functional layer and anode mechanical support layer. Our cells currently require 2-3 layers (bilayer or trilayer). SOFC electrode tapes are also significantly thicker and require longer drying times. For this reason, $3/m^2 is used instead of Little's $6/m^2.

4.5.3 - Calendering/laminating

(Unit Op Cost: $1/m^2)

In anecdotal experience based on work in the Wachsman lab, lamination of SOFC tapes requires significantly longer times than lamination of garnet tapes. This is possibly because different tape recipes are used, because the garnet tapes are so much thinner, or because there are fewer layers in a garnet tape. Instead of an 8 hour press, garnet tapes can be pressed for 30 minutes total. At this timescale, lamination could be a nearly continuous roll-to-roll process, which could feed into in-line cell stamping and sintering. Lamination is somewhat similar to a screen printing operating (pressing for a specified amount of time), though with higher pressure, so Little's $3/m^2 can be used as a starting point. However, changing to a continuous process and removal of a spray nozzle maintenance would dramatically decrease the price. A price of $1/m^2 is used.

4.5.4 - Sintering

(Unit Op Cost: $5/m^2)

SOFC materials generally sinter well above 1000 °C (For example, gadolinia doped ceria sinters at 1450 °C for 4-6 hours). Our garnet cells have been sintering at 1050 °C for 20 minutes or 950 °C for 5 hours. The 1050 °C profile represents at least a 10 fold reduction in sintering time and a 400 °C decrease in temperature. This saves a significant amount of energy and processing time. Furthermore, less expensive nichrome heating elements can be used below 1100 °C, instead of the more expensive molybdenum disilicide elements which require frequent replacement. However, some time must still be allowed for burnout. The burnout currently used is three stages for 30 minutes each. Assuming a similar burnout for SOFC's, a more accurate time comparison would be 110 minutes (90 minute burnout + 20 minute sintering hold) for batteries and 330 minutes (90 minute burnout + 240 minute hold) for SOFC's. Another factor increasing cost for lithium garnet is the requirement to provide a lithium rich atmosphere. It is hard to predict the cost requirement for this, as the final manufacturing may involve holding relatively small amount of lithium carbonate in the furnace, compared to the use of lithium garnet powderbed now. Based purely on time and temperature, Little's $18/m^2 could be cut to $3-4 to account for one third the sintering time and a much lower temperature. A conservative total cost of $5 is used to account for lithium atmosphere costs.

4.5.5 - QC layer

(Unit Op Cost: $6/m^2)

Quality control for SOFC's requires gas permeability testing, which is a complex and time intensive procedure and likely makes the the bulk of the cost of QC. For our cells, electrolyte integrity can be determined via electrical tests after active materials are added, as in most cases, pinholes will allow short to form at the time of assembly. Otherwise, quality control for sintered cells should be very similar between SOFC's and batteries. Specifically planned tests for our batteries are electrochemical impedance tests on the sintered trilayer scaffolds and cell flatness tests. Nondestructive impedance tests usually take several minutes per measurement. However, it may be possible to determine a single representative frequency or several frequencies which can be probed within seconds. This practice is used in traditional batteries (http://www.nrl.navy.mil/techtransfer/available-technologies/sensors/SOH-monitoring-lithium-ion-batteries). The flatness tests can be done using laser scanning in-line without slowing down production. The overall time and complexity of these test is significantly lower than SOFC test. Still, due to the importance of quality control Little's $\$9/m^2$ is only reduced to $\$6/m^2$.

4.5.6 - Cathode Infiltration

(Unit Op Cost: $\$3/m^2$)

The current method used for cathode infiltration requires the deposition of a volatile, inviscid slurry, followed by a short drying time. While this is not discussed in Little's analysis, the liquid deposition could be spray coated which is an in-line technique. Multiple passes may be necessary to achieve high cathode loading. A rough estimate of cost can be found in Little's cost estimate for screen printing. Spray

coating is a shorter, less work intensive technique than screen printing but the spray coating's extra passes will likely counter this. Little's estimate of $\$3/m^2$ for screen printing on top of sintered cells was used as the cathode infiltration cost..

4.5.7 - Interface Deposition

(Unit Op Cost: $\$1/m^2$)

Atomic Layer Deposition (ALD) is currently used to deposit a thin Al_2O_3 interface on the garnet. ALD is generally considered to be a slow process. However, due to the very thin layer deposited, our ALD procedure on a Beneq TFS 500 takes under two minutes per batch once under vacuum and at temperature. For a 10x10cm cell, roughly 1 mg of Al_2O_3 would be deposited per porous layer using the current protocol. Continuous operation ALD systems are a possibility such as that developed by Picosun. Given the right system, throughput could be very high and precursor usage could be quite low. Though this process is not likely to be a bottleneck, the machine cost and precursor are expensive and are being investigated.

It is also likely that ALD is not necessary and that a solution based process could achieve the same outcome. With this development, a spray coating could be applied in one pass because a very thin layer is desired. A cost of $\$1/m^2$ is used to account for a single pass spray deposition.

4.5.8 - Lithium infiltration

(Unit Op Cost: $\$4/m^2$ for Li-deficient cathodes, \$0 for Li-rich cathodes)

Lithium infiltration is performed by applying light pressure to lithium metal

and the sintered trilayer, heating to 300 °C, then cooling. This is similar to brazing, which Little gives a price of $2/m^2. However, because lithium metal is used, this must be performed in a dry or inert environment. To account for the increased infrastructure needed a total price of $4/m^2 may be appropriate.

It should be noted that this procedure will only be necessary for lithium deficient cathodes such as sulfur. Most oxide cathodes will not require this and only require some electronic conducting phase to be present. This may be achieved through mixed ionic-electronic conductors (MIEC's) developed by Dr. Thangadurai's current research, which would not add to processing costs. If this technology is not available conductive carbon can be infiltrated similar to the cathode at $3/m^2. In the final calculation, a cost of $0/m^2 is used as it is likely some appropriate MIEC can be found and a Li-rich NCA cathode has been assumed for these calculations.

4.5.9 - Stacking/Packaging

(Unit Op Cost: $1.97/m^2)

Packaging is an area where SOFC's and batteries diverge entirely and Little's analysis was not used. An initial estimate can be developed by determining the cost for manual stacking. If each cell must be stacked with an interlayer sheet and each layer requires 2 seconds to position, it will require 1000 seconds to stack 1 m^2 of cells. It can be assumed that 564 cells (1 kWh using an NCA cathode) are stacked per package and it requires 10 minutes to seal the package and check that the seal is good. Using Little's assumed $14/hr labor rate and a conservative 1:1 ratio for Direct:Indirect labor, the total cost to package cells is $3.94/m^2. This cost would be

significantly lower with an industrial plate stacker such as a Wirtz PS-23-50. As a conservative estimate, we can guess than the plate stacker would cut total assembly time in half, giving a cost of $1.97/m^2.

4.5.10 - Converting cost from $/m^2 to $/kWh

These costs must converted to the metric in which batteries are actually sold, $/kWh. To convert, kWh/m^2 is needed, which is dependent on cathode selection, cathode loading, and cell thickness. Using the NCA-cathode cell design in Table 18, achieving 1 kWh requires 564 10x10cm cells, or 5.64 m^2 of cells. Therefore, the total processing and overhead cost is the sum of the operations above multiplied by 5.64. For this procedure at this scale, this gives a total cost of $132/kWh. This cost is highly sensitive to the number of cells per kWh, which is directly dependent upon energy density and electrode layer thickness. This dependence upon energy density can be seen in Figure 39 in the summary.

Summary of medium scale cost estimation

The performance and cost metrics of commercially available LCO, NMC, and NCA are compared alongside LFMO and sulfur in Table 21. This process cost considers a scale of 7.55 MWh/yr, which a shorter term goal and does not fully benefit from economies of scale.

Cathode	Cathode material price ($/kg)	Cell specific energy (Wh/kg)	Cell volumetric energy density (Wh/L)	Material cost ($/kWh)	Processing cost at 7.55 MWh/yr ($/kWh)	Total cost ($/kWh)
$LiCoO_2$	$15.00	266.0	952.6	$42	$184	$226
$LiNi_{1/3}Mn_{1/3}Co_{1/3}O_2$	$20.00	310.0	1087.5	$44	$156	$200
$Li_2FeMn_3O_8$	$6.86	300.0	1,078.3	$24	$164	$188
$LiNi_{0.8}Co_{0.15}Al_{0.05}O_2$	$30.00	359.3	1,235.9	$51	$132	$183
Sulfur	$0.16	587.3	1,362.4	$18	$99	$117

Table 21. Cell chemistry dependence of cost and energy densities.

A comparison of these oxide cathodes shows that while the costs and energy densities of the cathodes vary, the cell material cost is roughly as sensitive to cathode cost as it is to cathode energy density. LFMO and Li-LFMO cells are significantly less expensive than the commercially available cathodes and corresponding cells. While this is partially due to the omission of processing costs in the calculated cost of LFMO, it is also expected due to the exclusion of the more expensive elements nickel and cobalt.

The material cost of sulfur is orders of magnitude lower cost than the oxide cathodes. However, sulfur does not contain lithium and therefore also requires lithium metal to be filled which adds to the cell cost. While the capacity of sulfur is 10x higher than the oxide cathodes, it expands during cycling and requires empty space in the pores. Sulfur also operates at roughly half the voltage as the oxide cathodes. Overall, the benefits still greatly outweigh the limitations, making a Li-S cell double the specific energy and half the cost of oxide cathodes.

Total cell cost is very sensitive to energy density due mostly to processing costs, as seen in Figure 39. This is because cells that are more energy dense have more energy per area and processing cost is mostly dependent upon cell area. Another way

to increase energy per area, and thus drive down costs, is to increase the thickness of the cells. It will be important to measure cell performance at varying electrode thicknesses to ensure the maximum electrode thickness is used for a given power requirement. Based on the low ASR of Li/Li symmetric cycling in a trilayer cell with two 55 um electrode layers, it seems likely that 100 um is not an upper limit for high performance. The use of thicker electrodes increases energy density and decreases the number of cells that have to be produced per kWh. This would lead to lower processing costs than the calculations in this document suggest.

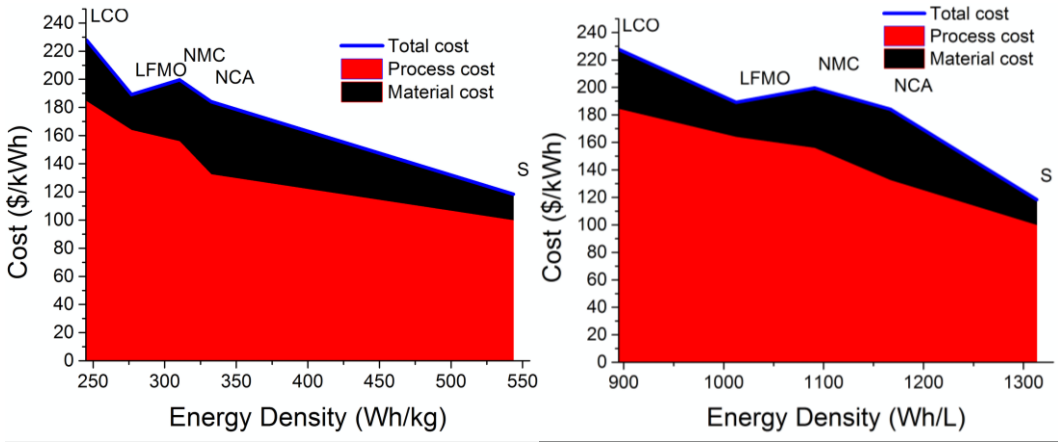

Figure 39. Dependence of total cell cost on energy density at a scale of 7550 kWh/year

While sulfur offers higher energy density at half the cost, moving forward with commercially available cathodes will meet the desired performance goals of 300 Wh/kg and $100/kWh on a materials basis. Cell material costs are at or below $50/kWh when using commercially available cathodes. Processing costs are highly dependent upon energy per cell and need to be calculated for a larger scale to estimate costs at full scale production.

Cost reductions with further scaling and development

ARPA-E models for existing battery technologies have estimated that scaling up from 7.5 MWh/year manufacturing to 7 GWh/year manufacturing results in ~66% decrease in overall pack price. Further scaling from 7 GWh/year to 35 GWh/year leads to another ~22% decrease in overall pack price. Estimated costs for scaled cells are listed in Table 22.

Cathode	Total cell cost at 7.5MWh/year ($/kWh)	Total cell cost at 7GWh/year ($/kWh)	Total cell cost at 35GWh/year ($/kWh)
$LiCoO_2$	$226	$77	$60
$LiNi_{1/3}Mn_{1/3}Co_{1/3}O_2$	$200	$68	$53
$Li_2FeMn_3O_8$	$188	$64	$50
$LiNi_{0.8}Co_{0.15}Al_{0.05}O_2$	$183	$62	$49
Sulfur	$117	$40	$31

Table 22. Battery cost by cathode and scale.

4.6 – Design Implications of Cost Analysis

To target lower total cell costs, focus should be on decreasing per kWh processing costs, which constitute 72% ($LiNi_{0.8}Co_{0.15}Al_{0.05}O_2$ cells) to 87% ($Li_2FeMn_3O_8$ cells) of the total. According to Figure 38, no single unit operation is an overall driver of processing cost. Therefore, the most direct strategy to decrease cost per kWh is to produce higher energy cells, which would lead to fewer cells needing to be manufactured per kWh. A design decision to double the electrode loading (likely through doubling the thickness of the porous layers) would cut processing costs in half. For the analysis in this chapter, 100 μm was chosen as an upper limit for electrode thickness. However, this is number was a rough estimate based on the 50-250 μm thickness of a cathode film for a liquid cell and should be studied in further detail.

As electrode thickness increases, ASR will increase. This may possibly decrease the maximum cell current if electrolyte conductivity is the limiting factor in current. It may also be the case that interfacial resistance or cathode kinetics are more limiting at 100 μm electrode thickness, in which case an increase in electrode thickness will not hinder performance. This can be tailored to application demands, whether performance or price is more important.

Chapter 5: Fabrication of Solid Electrolyte Structures

The starting point for making these cells is the synthesis of LLZ and the fabrication of the triple layer SSE. Beyond the general difficulties in adapting synthesis and fabrication procedures from literature, lithium garnets poses extra challenges in this application. Lithium garnets tend to sinter poorly and sinter at temperatures that cause significant lithium volatility in the furnace[91,101,108,109]. This increases the difficulty of achieving a pore-free dense center membrane for full separation of electrodes. Furthermore, lithium garnets exist in a high conductivity cubic phase, as well as a lower conductivity tetragonal phase. While there is literature on the phenomena that favor the formation of one phase over another, many factors influence phase formation such as furnace time and temperature, crucible material selection, lithium content and garnet composition[25,27,28,101].

LLZ was synthesized by solid state reaction. The precursors, LiOH, La_2O_3, and ZrO_2 were mixed together in stoichiometric ratios, with an excess of 10% LiOH to compensate for lithium loss during heating. LiOH and La_2O_3 were dried at 100 °C and 800 °C, respectively, for 24 hours prior to weighing. After milling for 24 hours in isopropanol then drying at 100 °C, the raw materials were calcined in an Al_2O_3 crucible at 900C for 12h to produce the proper cubic garnet phase. Another 24 hours milling in isopropanol was used to break up agglomerates after calcining and produce smaller particles. Powder X-ray diffraction (XRD) was performed on a Bruker D8 in the University of Maryland X-ray Crystallography Center in order to confirm garnet phase. Lattice parameter was fit using Rietveld refinement in the Bruker DIFFRAC.SUITE Topas software. It can be seen in Figure 40 that this synthesis

procedure led to the cubic garnet phase. Rietveld refinement of this pattern revealed a lattice parameter of 12.96905 Å, right in the expected range of about 12.9 – 13.1 for published lithium garnets[25].

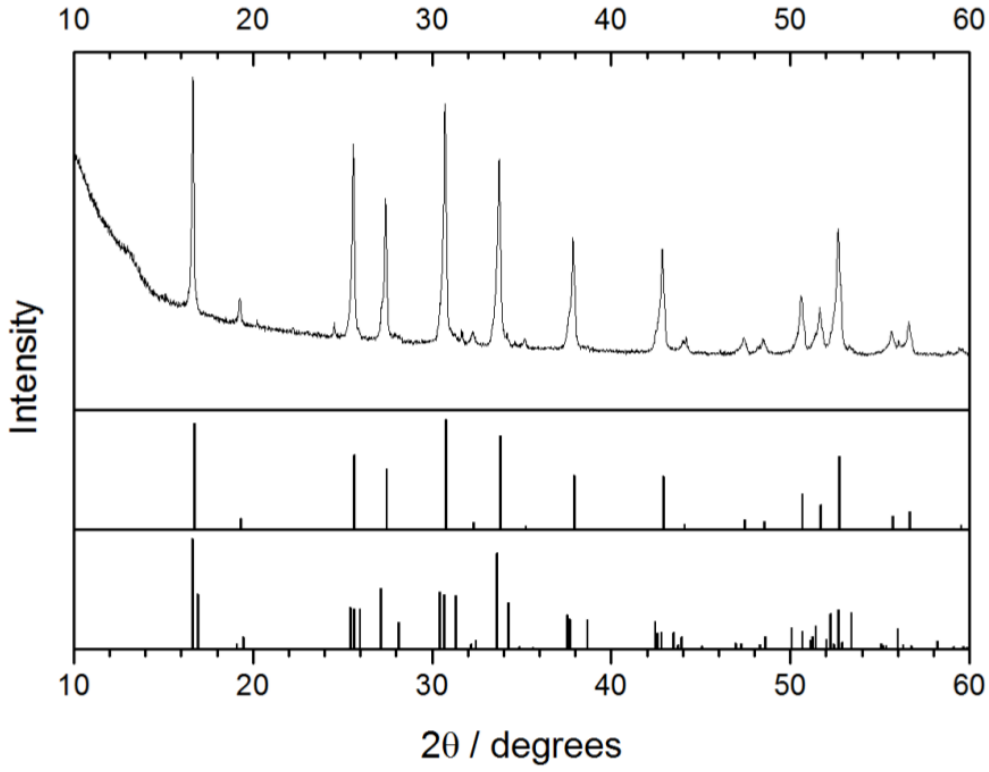

Figure 40. (top) XRD pattern of LLZ compared to reference peaks for (middle) cubic lithium garnet (JCPDS 080-4947) and (botom) tetragonal lithium garnet (JCPDS 078-6709).

Scalable production of thin garnet films involves casting an organic tape with the garnet ceramic in suspension and sintering this tape to burn off the ceramic and achieve the final desired microstructure.

5.1 - Development of tapecasting protocol

As laid out in Figure 41a, the tapecasting process involves the production of a slurry comprising organics and ceramic for the purpose of casting into a thin, flexible film. The advantages of tapecasting include scalability, high green body density, and the ability to repeatably form desired shapes and sizes for the final device.

Tapes begin with the synthesis of pure cubic phase garnet. Solid state reaction is used to synthesize the garnet beginning by milling stoichiometric amounts of ZrO_2 and dried La_2O_3 with 25% excess $LiOH\text{-}H_2O$ in isopropanol. The milled material is dried at 100 ºC and heated to 900 ºC for 4 hours. After milling again in isopropanol, the garnet is ready for use in a tapecasting slurry.

Milled garnet powder is added to toluene and isopropanol. A small amount of fish oil is added as a dispersant. After 24 hours of milling, polyvinyl butyral (PVB) and benzyl butyl phthalate (BBP) are added as binder and plasticizer respectively. The structures of PVB and BBP are shown in Figure 41b and Figure 41c, respectively. The materials used in this slurry are standard use in industry. This final slurry composition is milled for another 24 hours before tapecasting. It was determined that to obtain a sufficiently inviscid tape, roughly double the solvent was required compared to solid oxide fuel cell tape recipes. Furthermore, roughly 30% extra plasticizer was required to achieve flexible films.

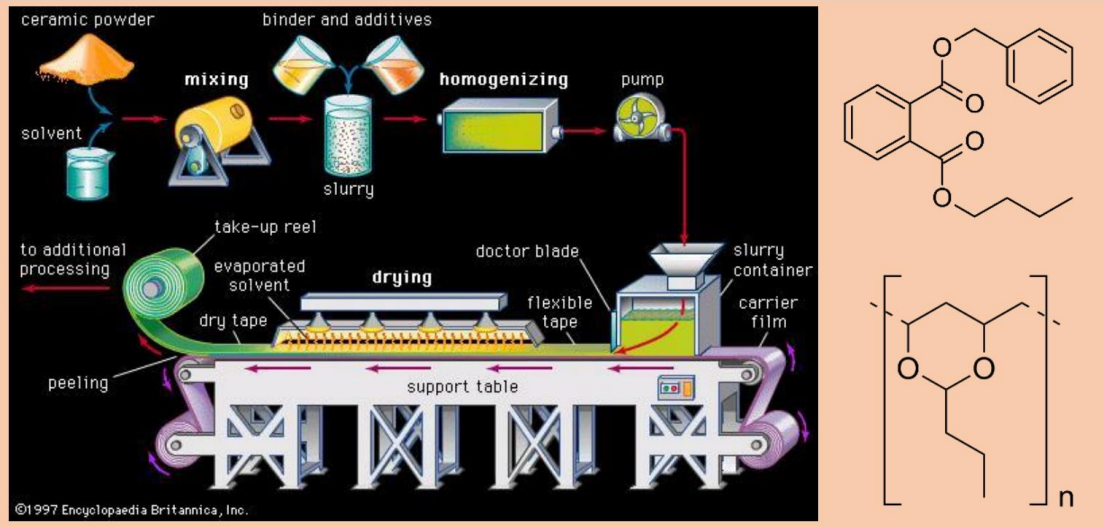

Figure 41. (a) Tapecasting process as depicted in Encyclopedia Britannica and (b) plasticizer benzyl butyl phthalate (BBP), and (c) binder polyvinyl butyral (PVB).

It was determined that to obtain a sufficiently inviscid tape, roughly double the solvent was required compared to solid oxide fuel cell tape recipes. Furthermore, roughly 30% extra plasticizer was required to achieve flexible films. The mass ratios of materials are given in Table 23.

Material	***Mass:Garnet mass***
Garnet	1
Isopropanol	1.1
Toluene	1.1
Fish oil	0.02
PVB	0.24
BBP	0.27

Table 23. Composition of tape slurry

Various properties of the resulting tapes are demonstrated in Figure 42a-f. Cast tapes are free of bubbles due to the proper viscosity and de-gassing conditions as seen in Figure 42a. Figure 42b shows that the tapes are properly flexible, with high plasticity due to an appropriate ratio of ceramic, binder and plasticizer. This property is essential in successfully laminating layers of tape. Figure 42c shows three layers of tape laminated together. These layers are a 150 um thick $Li_7La_3Zr_2O_{12}$, a 20 um thick $Li_7La_{2.75}Ca_{0.25}Zr_{1.75}Nb_{0.25}O_{12}$ layer and another 150 um $Li_7La_3Zr_2O_{12}$ layer, to be sintered into the desired porous-dense-porous structure. Also a consequence of proper tape plasticity, Figure 42d shows that circles can be punched out of tapes before sintering for the fabrication of 1" button cells. Due to shrinkage in the furnace, this triple layer sinters into a 0.8" diameter cell with a total thickness around 100 um, shown in Figure 42e and Figure 42f. This is close to the target thickness.

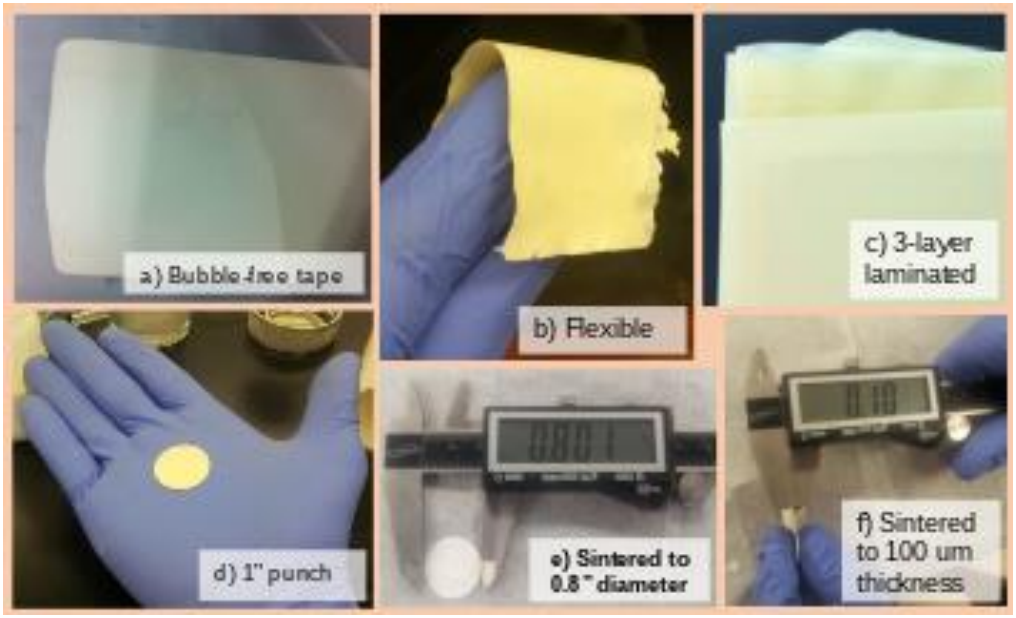

Figure 42. Demonstrated properties of tapes as cast and sintered.

X-ray diffraction of the sintered cells revealed that garnet phase was completely lost during sintering, as seen in Figure 43. The only phases present are La2Zr2O7 and La2O3, indicating lithium deficiency.

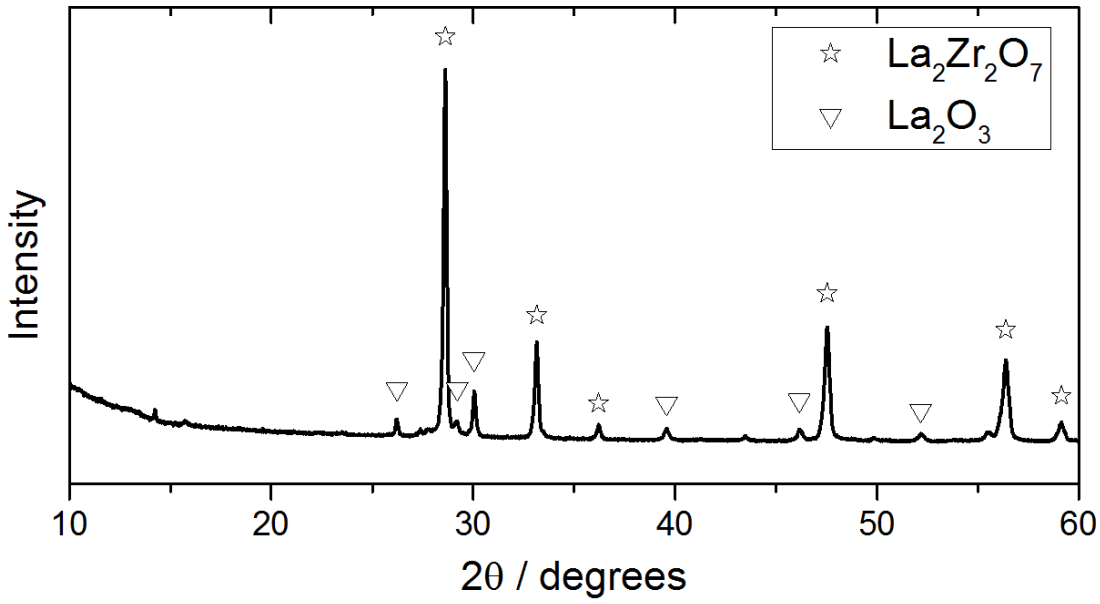

Figure 43. XRD of LLZ tape sintered at 1150 °C for 1 hour.

5.2 - Investigation of phase loss in sintered tape

Initial attempts to increase lithium retention included increasing lithium concentration in the initial weigh-out, decreasing sintering time, and decreasing sintering temperature. When none of these attempts showed any improvement, it was suspected that a reaction between the garnet and a polar component of the slurry was occurring, as garnets are susceptible to reaction in a polar environment. This was tested by extracting the garnet from an unsintered tape and measuring the X-ray diffraction pattern. Extraction was performed by milling a cast tape in toluene and isopropanol for two days to return the tape into slurry form. This slurry was placed onto a vacuum filter and washed with copious amounts of toluene and isopropanol.

The diffraction pattern of the resulting garnet can be seen at the top of Figure 44. While the garnet batch used to produce this tape was tetragonal, the pattern matches that of the starting material garnet, indicating no reaction occurred.

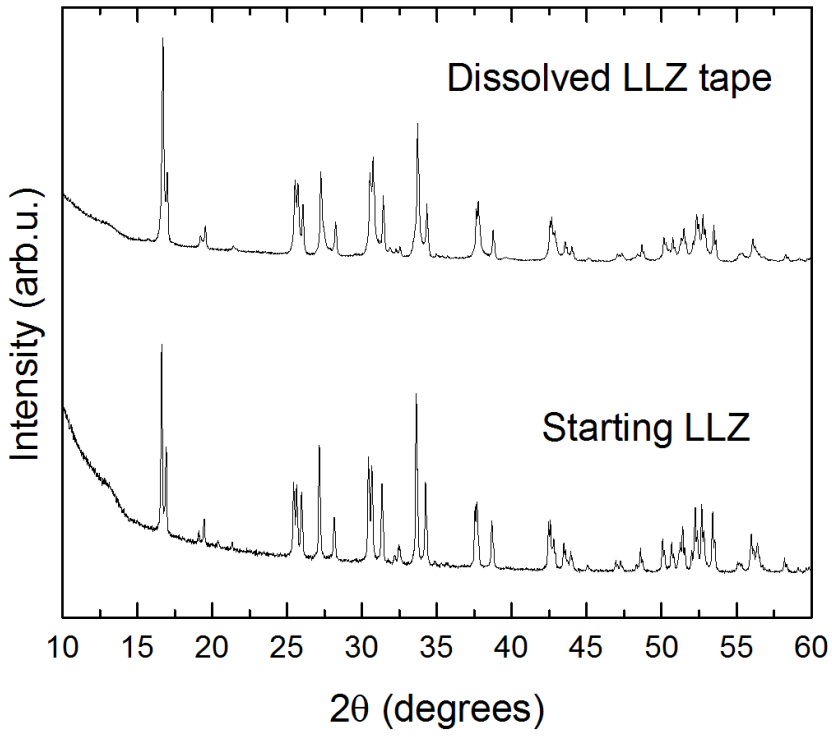

Figure 44. XRD of garnet extracted from LLZ tape (top) compared to the starting material garnet used for making the tape (bottom)

It was next suspected that a reaction was occurring during the burnout phase, from room temperature to 500 ºC, where most of the organics oxidize. Significant work was done to investigate the possibility that various slurry components were reacting with the garnet as the temperature increased during burnout. Various leads were followed due to increased reaction in some samples versus others, though resolving these issues never conclusively resulted in retention of the garnet phase. By comparing the conditions of the multiple experiments it was realized that the samples

tested on rainy days may have shown more reaction. It was hypothesized that the humidity in the air reacts at elevated temperature with the garnet.

An experiment was designed to test this hypothesis. Figure 45 shows a diagram and photograph of the experimental setup. Various gases were flowed over LLZ during heating in a furnace to 500 ºC, a 30 minute hold, and cooling to room temperature. Test gases included dry synthetic air (79% N_2, 21% O_2), synthetic air bubbled through room temperature water, dry CO_2, and CO_2 bubbled through room temperature water. CO_2 was included as a test gas because CO_2 is created in the combustion of organics, and could react with garnet on its own or in conjunction with water. This same reasoning is why CO_2-free synthetic air was chosen for the air test.

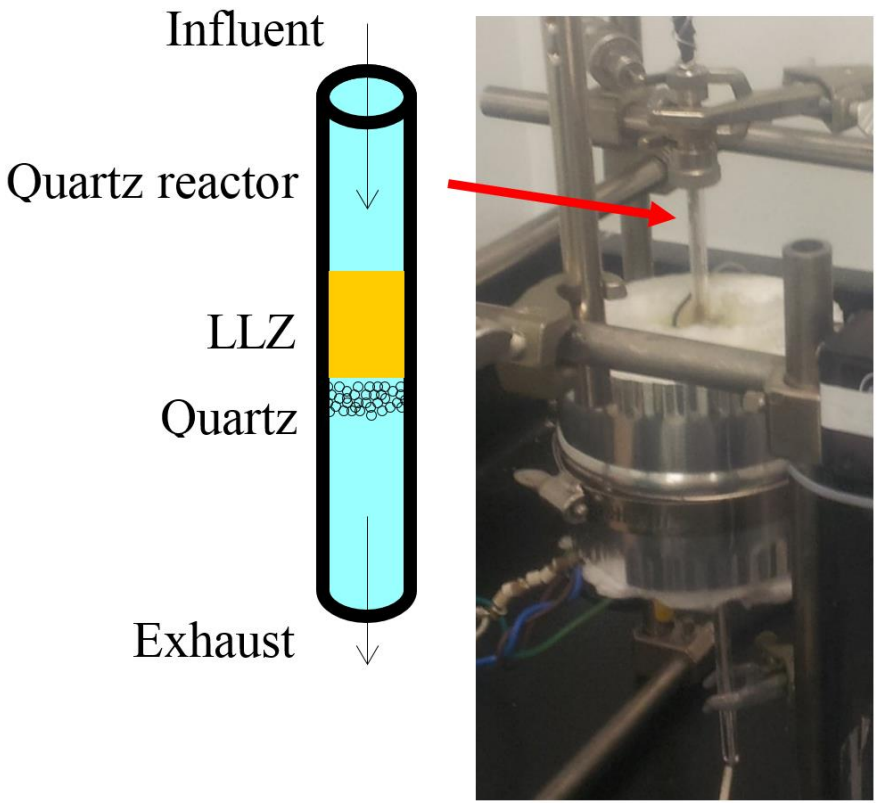

Figure 45. Diagram (left) and photograph (right) of reactor setup used for testing LLZ under varying gas conditions.

The results of this experiment are given in Figure 46, comparing the X-ray diffraction patterns of the resulting samples with the unreacted LLZ. Figure 46a shows no change in phase between the initial pure-phase garnet and that heated in dry air. Similarly, Figure 46b shows no change in phase between initial pure-phase garnet and that heated in dry CO_2. However, when the air is bubbled through room temperature water, picking up about 3% water by mass, the garnet phase is nearly completely gone. This implies that the humidity is what damaged the garnet phase. Interestingly, the wet CO_2 showed very little reaction, though there was some peak splitting. This could be explained by the CO_2 picking up significantly less water, or the CO_2 could have some protective effect. Succinctly, humidity is damaging to the garnet phase and CO_2 may or may not be protective, but is likely not damaging.

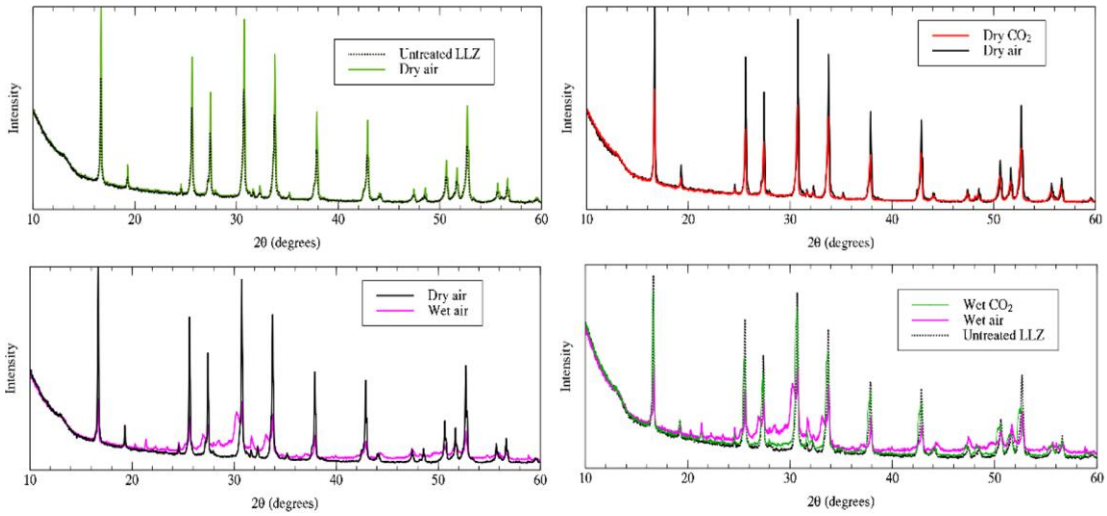

Figure 46. XRD of LLZ garnet heated to 500 °C in (a) dry synthetic air, (b) dry CO2, (c) wet synthetic air, and (d) wet CO2.

The results of this experiment were tested by taking a cast tape through the burnout phase under dry compressed air (not synthetic air), heating to 500 °C, and

holding for 30 minutes, then cooling. Figure 47 shows the X-ray diffraction pattern resulting from this sample, indicating that pure garnet phase was maintained and that the low temperature reaction issue had been resolved.

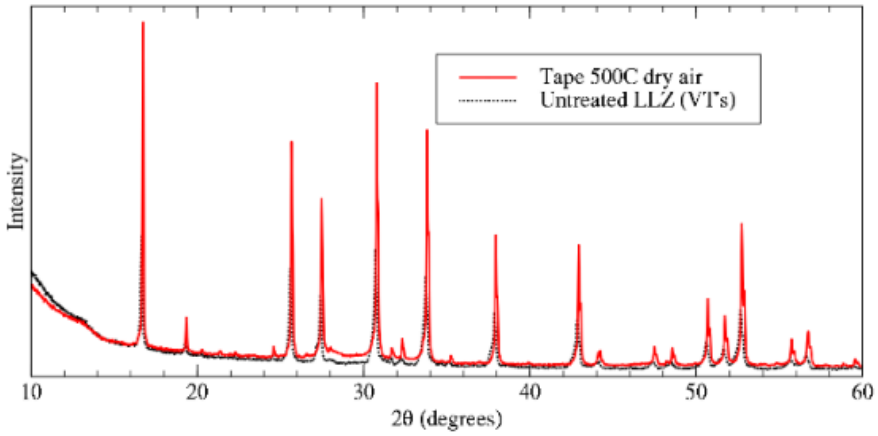

Figure 47. XRD of LLZ tape heated to 500 °C under dry compressed air.

Figure 48 shows a photograph of the assembly that was heated in the furnace. Garnet powder was spread on a porous alumina plate and covered by a sacrificial garnet tape. After the tape disc is placed on the assembly, another sacrificial tape, power and porous alumina plate are put on top. This assembly is meant to press the tape so it remains flat during sintering, while increasing the vapor pressure of Li_2O. The sacrificial tape is easier to separate from the sintered disc than if the powder touched directly.

Figure 48. Photograph of the garnet disc ready for sintering on a porous Al2O3 plate, covered in garnet powder, sacrificial garnet tape, and the target tape disc.

However, when tapes were sintered to 1150 ºC, the garnet phase was again lost, as seen in Figure 49. While very small garnet peaks remained, indicating ~2% garnet phase in the sample, lithium deficient phases were dominant. It is important to note that no aluminum-containing phases were detected. This indicates that the loss of garnet phase is likely due to loss of lithium and not due to an excess of aluminum diffusing from the alumina crucible. Decreasing the sintering temperature by 100 ºC to 1050 ºC increased the proportion of garnet phase in the sample to ~45%. Not only is this phase purity insufficient but is also tetragonal garnet, which is significantly less conductive.

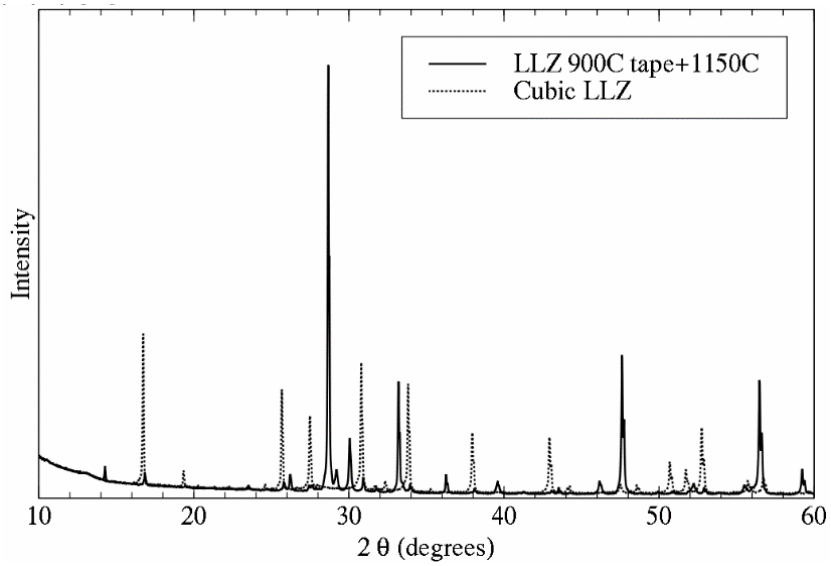

Figure 49. XRD of garnet tape as sintered at 1150 °C

Because it is believed that the volatile species is Li_2O, it was hypothesized that sintering under N_2 would decrease the creation of Li_2O and therefore less lithium would volatilize. The results of this shown in Figure 50a indicate that N_2 sintering at 1050 ºC produces a cubic garnet that is less peak shifted than the air sintered tape at the same temperature, indicating that the N_2 helped reduce lithium volatilization. Furthermore, it can be seen in the sharp 29º peak of Figure 50b that the N_2 sintering significantly reduced the proportion of the impurity phase $La_2Zr_2O_7$.

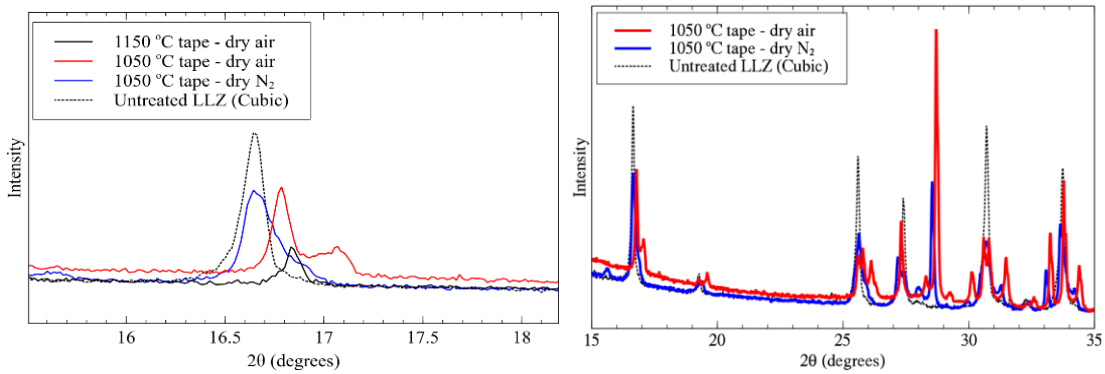

Figure 50. XRD of various sintering conditions of LLZ tape. (a) Close-in view showing a major garnet peak and (b) larger view showing the difference between N2 sintering and air.

After only one hour at the sintering temperature of LLZ (1150°C), only about 2% garnet phase remained. Reducing the sintering temperature by 100°C showed a dramatic improvement to 45% final garnet phase. This indicates that a volatilization of lithium, which would be worse at higher temperatures, is likely the cause of phase loss. To achieve impurity-free garnet, further measures were studied to improve lithium retention.

To account for the specific species of lithium volatilizing from the garnet, various gas conditions were tested. The most likely volatile lithium species, listed in Table 24, are LiOH, Li_2CO_3, Li_2O, and Li_3N. The resulting purity after sintering under CO_2, O_2, N_2, Ar or dry air atmosphere would indicate which reaction is problematic. It is important to point out that under any atmosphere, Li_2O volatilization from the lattice is also a possibility. The various sintering gases and their expected reaction products are given in the table below. Wet atmosphere production of LiOH was not tested and assumed to be problematic due to our previous results indicating significant phase loss at low temperature under humid air.

Sintering gas	*Possible lithium species formed*
CO_2	Li_2CO_3
O_2	Li_2O
N_2	Li_3N
Ar	None
Dry air	Li_2CO_3, Li_2O, Li_3N

Table 24. Possible lithium species formed in various furnace atmospheres.

The sintering profile for the reaction is given in Figure 51. Example sintering profile of a garnet tape.. After a low temperature air burn out stage, the sintering gas is flowed into the tube furnace continued to run throughout the ramp up, hold time and ramp down.

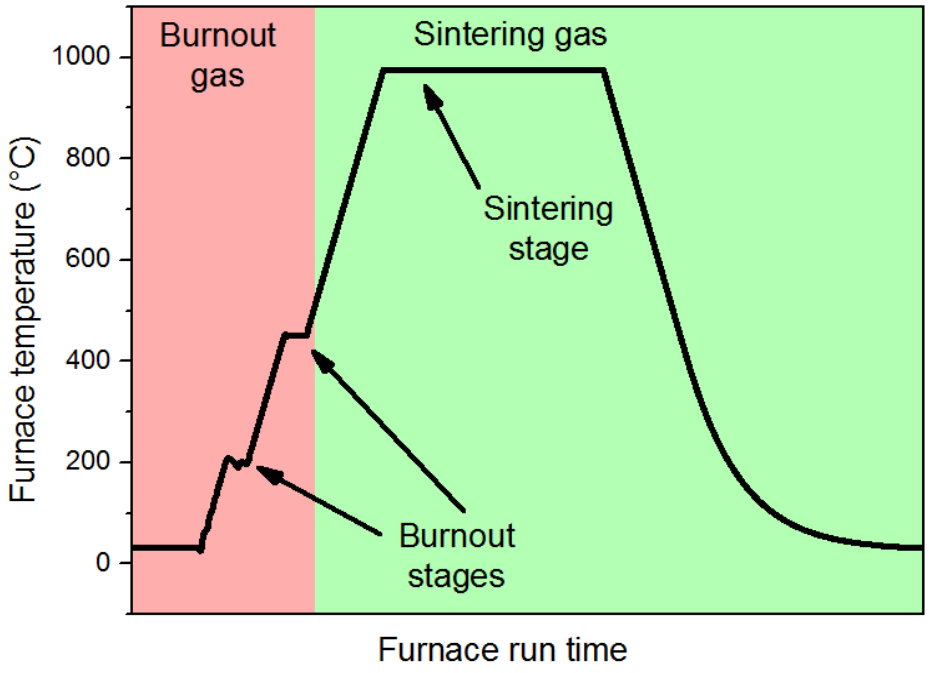

Figure 51. Example sintering profile of a garnet tape.

The X-ray diffraction patterns of the resulting sintered garnet tapes are given in Figure 52. The results of this study show garnet phase retention when sintered in argon or O_2, but significant presence of lithium deficient phases in CO_2, N_2, and dry air. This suggests the formation and volatilization of Li_2CO_3 and Li_3N from the garnet lattice. The garnet phase formed in the O_2 and argon environments is the tetragonal form of garnet phase.

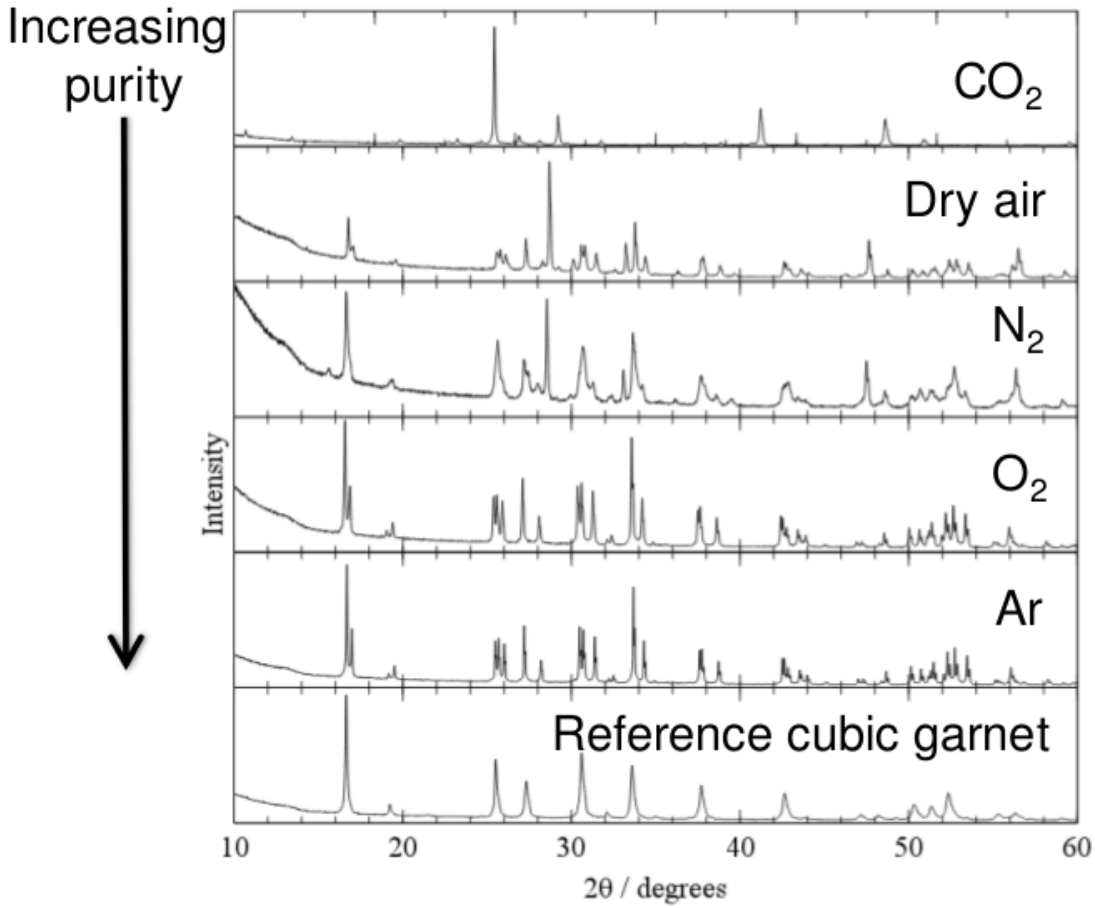

Figure 52. X-ray diffraction patterns of $Li_7La_3Zr_2O_{12}$ tapes sintered at 1050 °C in test gases. Test gases are (from top to bottom) CO_2, dry air, N_2, O_2, and Ar. These diffraction patterns are compared to a reference pattern of cubic garnet.

The tetragonal phase of garnet has been shown to have two to three orders of magnitude lower conductivity than the cubic phase. For this reason, further work was done to achieve cubic phase. Literature has shown that aluminum doping in the garnet from the alumina crucible increases the stability of the cubic phase. It is possible to increase aluminum doping and increase sintering density by lengthening the sintering time. This requires more measures to protect against lithium volatilization.

We theorized that the air burn out phase leaves surface carbonates on the garnet lattice, which volatilize at the sintering temperature. If the binder is instead burnt out in O_2, formation of surface carbonates would be minimized, preserving the integrity of the garnet surface. It may also be possible that after O_2 sintering, surface Li_2CO_3 is converted to Li_2O is formed which would be less volatile than the Li_2CO_3, thus taking longer to degrade before exposing the garnet surface and allowing lattice lithium to be lost.

This was tested by burning out the tape in either air then sintering for two hours or O_2 then sintering for five hours. The X-ray diffraction patterns of these samples are shown in Figure 53. First, it can be seen in the air burnout that increasing the sintering time from one hour to two hours allowed the lattice to form the cubic garnet phase. It can also be seen that the $La_2Zr_2O_7$ peak at 29 degrees, indicating a lithium deficiency, is large in the air burnout with only a two hour hold, whereas the peak is very small in the sample treated with a five hour hold after O_2 burnout. O_2 burn out followed by five hour argon sintering at 1050 °C produced nearly pure cubic garnet phase with sintering conditions which are reasonable for LLZ.

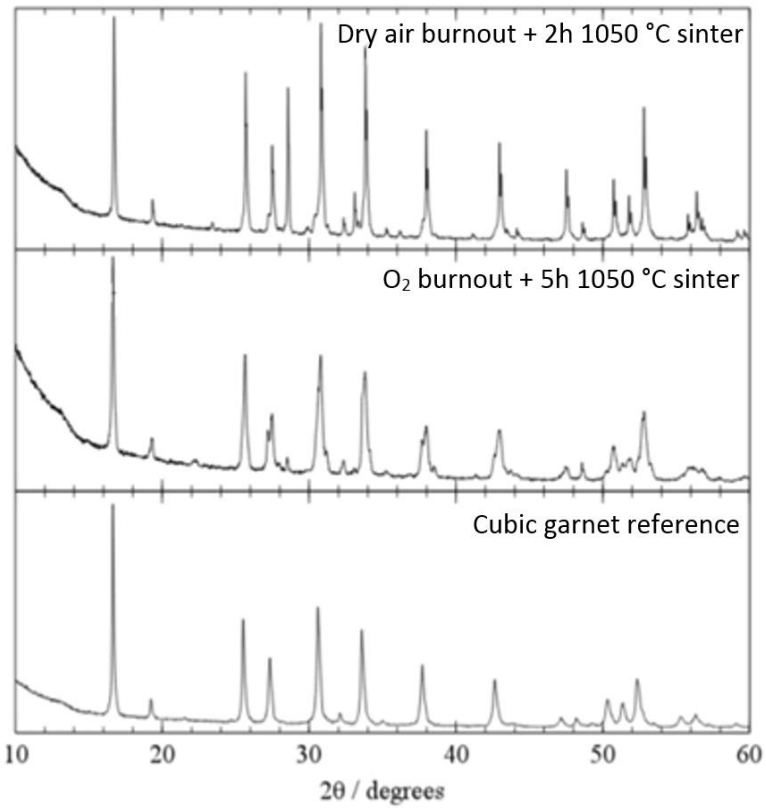

Figure 53. X-ray diffraction pattern of LLZ tapes after 1050 °C sintering compared to a cubic garnet reference.

5.3 - Achieving high sintering density

An SEM image of the tape microstructure formed by the five hour hold and O_2 burnout is presented in Figure 54. This image demonstrates that the three tapes were well laminated, as the scaffold shows no cracking between layers. Furthermore, it achieves the desired structure of a porous-dense-porous triple layer.

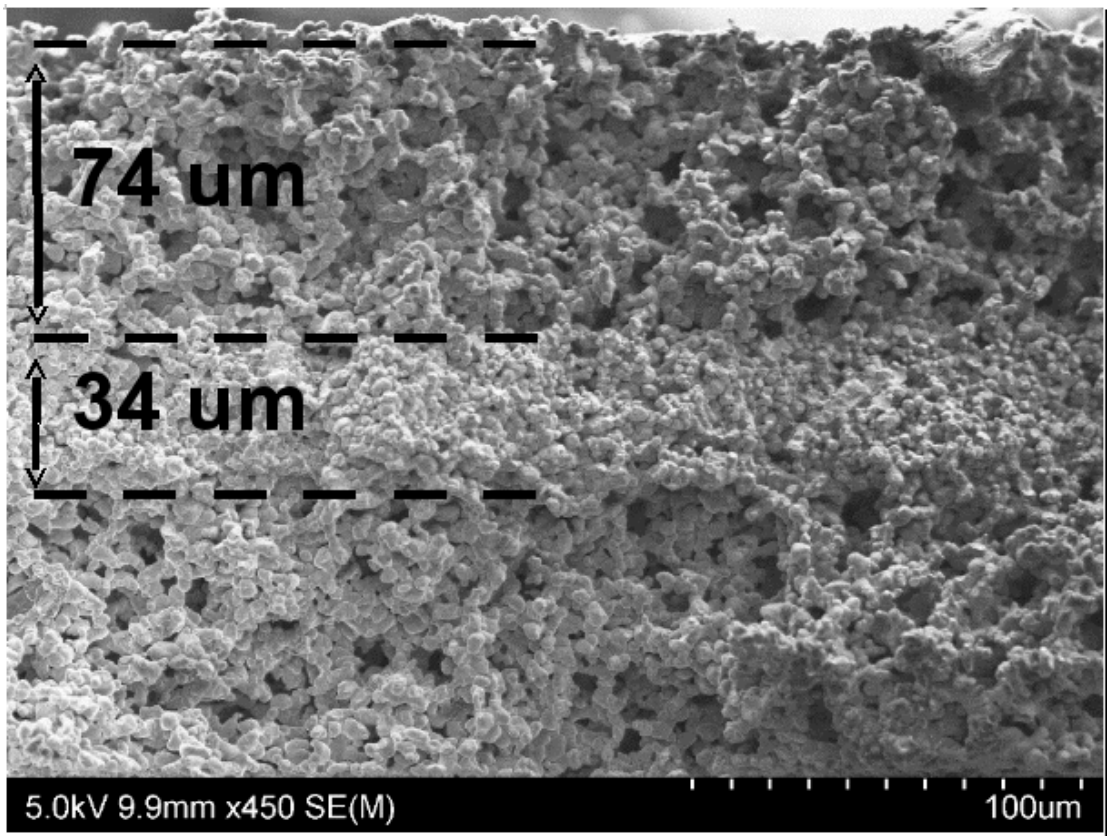

Figure 54. SEM image of LLZ microstructure after O_2 burnout then sintering at 975 °C in Ar.

However, the porosity of the dense layer is too high. Well-established ceramics processing techniques were attempted to further densify the center layer. Li_3BO_3 and Al_2O_3 sintering aids have been shown in literature to significantly decrease the sintering temperature and increase sintered density in lithium garnets without decreasing conductivity but were our tests were unsuccessful. A new lithium garnet member, $Li_{6.75}La_{2.75}Ca_{0.25}Zr_{1.5}Nb_{0.5}O_{12}$ (LLCZN), was used which has a high conductivity ($6x10^{-4}$ S/cm) and low sintering temperature (1050 °C).

Additionally, smaller particle size LLCZN was synthesized via extended ball milling and an added ball milling step with smaller (2mm) grinding media. Smaller

particle size, thus higher surface area, powders sinter more readily, as this decreases the high surface energy associated with the high surface area. Significant amounts of sub-micron sized LLCZN powder was needed due to the large amount of powder needed to prepare tapes.

The typical size distribution of garnet powder prepared milled overnight in 5 mm media is in the range of 2 to 5 μm diameter. An SEM picture of a batch of sub-micron sized powder is shown in Figure 55. According to dynamic light scattering, the average particle size is in the 400 nm range. Brunauer-Emmett-Teller (BET) analysis shows surface area of 20 m^2/g, which is a high surface area for ceramics. SEM imaging shows many particles in the 200-500 nm range, but also some particles as small as 25 nm.

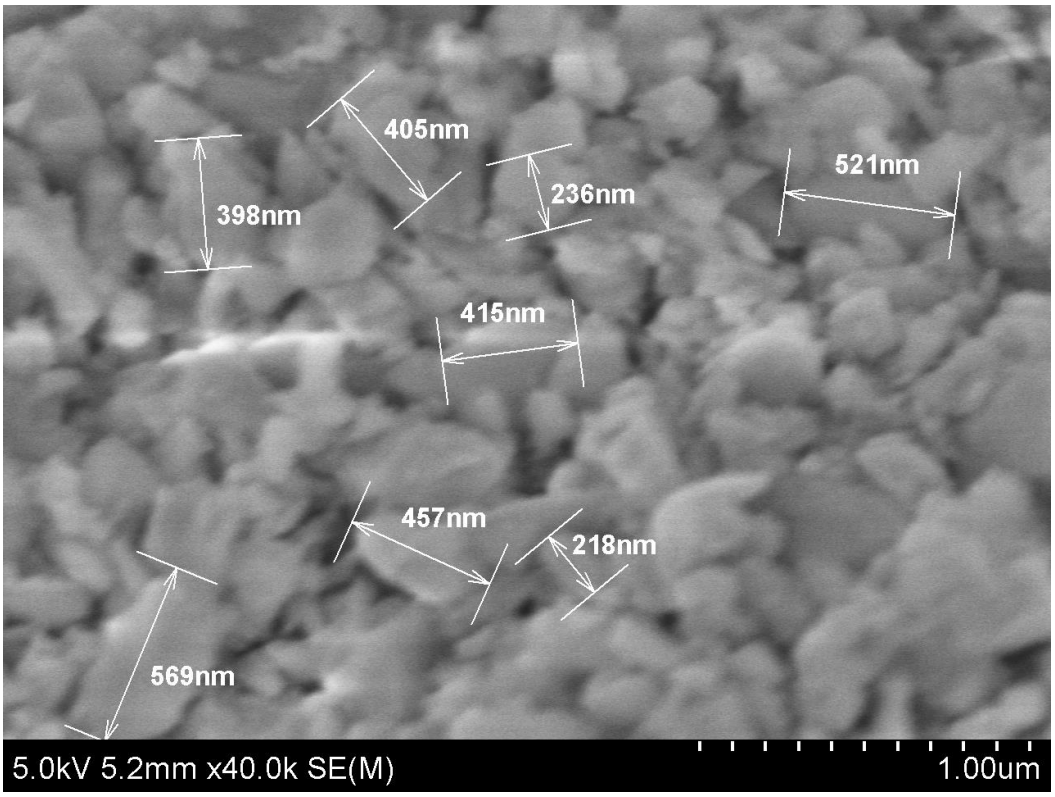

Figure 55. SEM image of $Li_{6.75}La_{2.75}Ca_{0.25}Zr_{1.5}Nb_{0.5}O_{12}$ after milling for 3 days with 5 mm grinding media and 18 days of milling with 2 mm grinding media.

A pellet of this powder was pressed uniaxially at 176 MPa and a Theta 1200C dilatometer was used to measure the sinterability. The contraction of the pellet was measured from room temperature to 1100°C at a scan rate of 1C/minute. Figure 56 shows the results of this study, indicating that sintering occurs above 700°C, highlighted in blue. It is likely that the dropoff at 980°C is due to a combination of sintering and lithium loss, highlighted in red. This result suggests an ideal sintering temperature around 950°C-980°C, as high as possible before significant lithium loss. This represents a significant decrease in sintering temperature from the published 1050°C, which should also lead to significantly lower lithium loss.

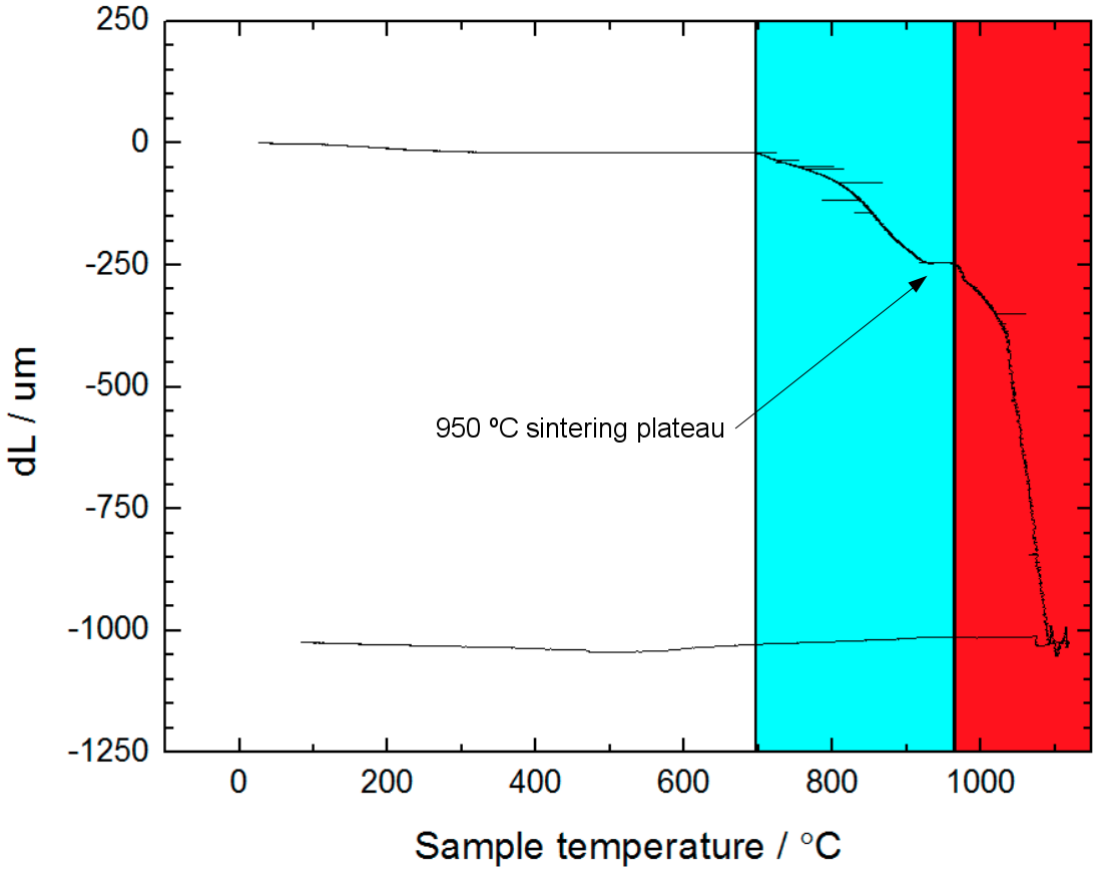

Figure 56. Pellet shrinkage at 1°C/minute ramp rate in Theta 1200C Dilatometer. The blue area is highlighted as a likely region for good sintering. The red area is highlighted as a likely region of rapid lithium loss.

The solid state submicron powder synthesis allowed for tapes to be cast for low temperature sintering. A triple layer tape was prepared with submicron powder LLCZN and sintered based on the results of the dilatometer study. This tape was presintered at 200°C, 450°C, then 650°C in oxygen for 30 minutes at each temperature then sintered at 950°C for 5 hours in argon. Figure 57 shows an SEM image of a fractured cross of this sintered triple layer demonstrating a high density center layer with two thicker porous layers on each side. This sintering density in lithium garnets is usually only achieved in hot-pressed samples[93,100].

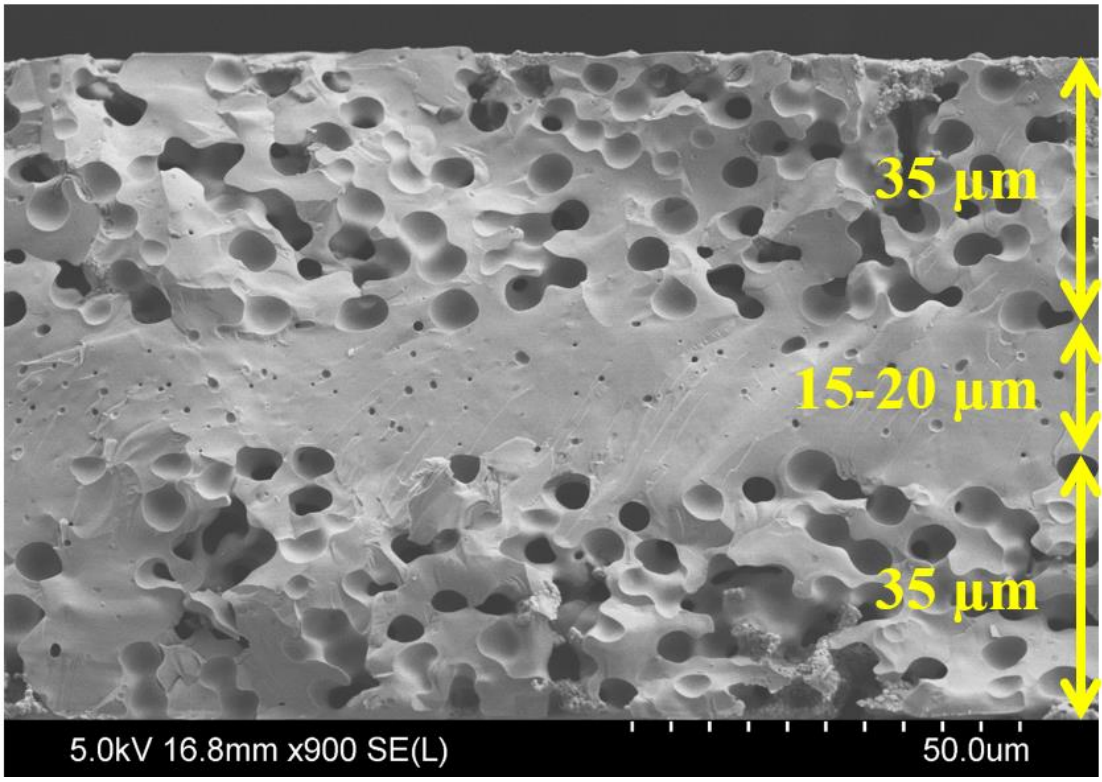

Figure 57. SEM image of a triple layer LLCZN garnet sintered at 950C for 5 hours in argon.

5.4 - Repeatability of trilayer sintering & process improvements

Reproducing this sintering density was difficult. Using what was believed to be the exact same process in the same furnace, many samples after the one shown in Figure 57 failed to sinter and looked more like the sample in Figure 54.

5.4.1 - Furnace consistency

A possible source of inconsistency in fabrication is the temperature of the furnace during sintering. While the temperature is well controlled using a thermocouple and a PID controller connected to the heating elements, the thermocouple placement is outside the sample tube containing the sintering body. Compounding this, gas flow is controlled with a volumetric flow controller at room temperature. To confirm internal temperature, a second thermocouple was inserted as close to the sample as possible. Gas integrity was maintained via a swagelok fitting around the thermocouple sheath. This furnace setup can be seen in Figure 58.

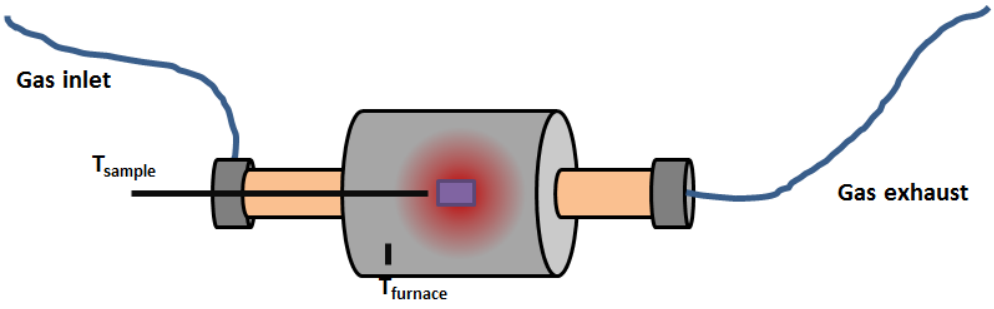

Figure 58. Diagram of the furnace setup currently being used to sinter trilayers. Thermocouple placement and gas flow is indicated, with the sample represented by a blue rectangle.

The furnace temperature and sample temperature were recorded for two identical runs and are reported in Figure 59, with Run 1 shown in solid lines and Run 2 shown in dashed lines. Note that the furnace is controlled with the "Furnace Temp", and not the "Sample Temp". It can be seen that the furnace was not able to maintain the exact profile even at the controller thermocouple. Furthermore, the sample temperature is at least 20 °C below the controller temperature and varied 30-40 °C between runs.

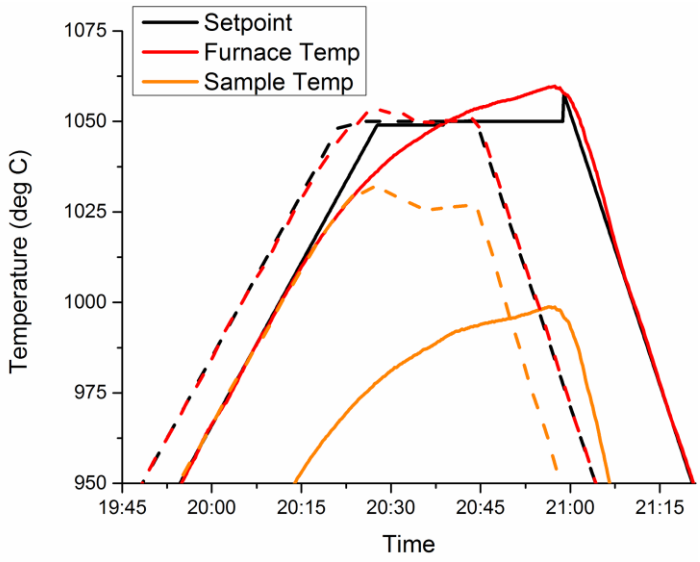

Figure 59. Plot of furnace temperature over time near the hold temperature of two trilayer sintering runs. The temperature at the "Furnace" thermocouple and the "Sample" thermocouple is shown with the working setpoint on the controller.

These issues were rectified in several ways. The PID had been tuned to 550 °C (roughly the halfway point between room temperature and hold temperature) in order to give it the best control over the entire range. Unfortunately, this had the drawback of giving the subpar control at the hold temperature. Gain scheduling was implemented which allowed for different tuning parameters in different operating

regions. This gave the greatest performance at all temperatures. The software was also adapted to allow handing off control of the furnace to the “Sample Temp” thermocouple in order to assure the most accurate sintering temperatures.

5.4.2 - Importance of powderbed

We also identified changes in lithium content as an important source of variability. While tapes cannot be completely buried in a powderbed in order to protect the tape from curling, a thin layer of powder is still used to retard the volatility of lithium from the lattice. It seems that this powderbed affects not only the phase purity, but also the sinterability of the material. This effect was investigated on samples sintered in the same crucible in the same furnace run. Two circular punches of green tape, shown on the left in Figure 60, were pre-sintered uncovered on an alumina plate at 650 °C in O_2 for four hours. These were removed from the furnace and immediately put into a crucible, either with or without garnet powderbed only millimeters apart. The crucible was then covered by an alumina plate and returned to the furnace. The furnace was heated to 1100 °C under argon flow, then held for 5 hours with the argon stagnant in the furnace to further improve lithium retention. The sample sintered in a powerbed (Figure 60 middle) is larger and a lighter color than the sample lacking a powderbed, indicating better sintering without a powerbed.

Figure 60. Photograph of three layer laminated garnet tape before pre-sintering (left), after pre-sintering exposed and sintering in argon at 1100 °C for 5 hours with powderbed (middle), without powderbed(right). The sintered samples shown were next to each other in the same crucible during sintering.

This result indicates that the difficulty in consistently replicating the dense layer could be attributed to a strong influence of variations in thickness and density of powderbed packing. The influence of lithium volatility conditions can be mitigated by further decreasing the sintering temperature of the garnet.

One hypothesis for this focused on the powderbed coating each trilayer. The importance of the powderbed in sintering variation had been previously established but we had not discovered the full extent of this effect. To perform a study on the effect of powderbed, we placed four trilayer tapes from the tape batch on the same alumina plate. These cells were covered in powderbeds from two LLCZN synthesis batches, one powderbed with LLCZN mixed with Al_2O_3 to investigate Al-doping effect, and one without powderbed. Batches were synthesized by various members of the team and were labelled via the operator's unique labelling systems. These were sintered in the same furnace run at 1000 °C for 1 hour in Ar, after a burnout stage in O_2. It can be seen in Figure 61 that significantly more shrinkage occurred in the cell

using the YG001 powderbed, indicating proper sintering. This was further confirmed by SEM.

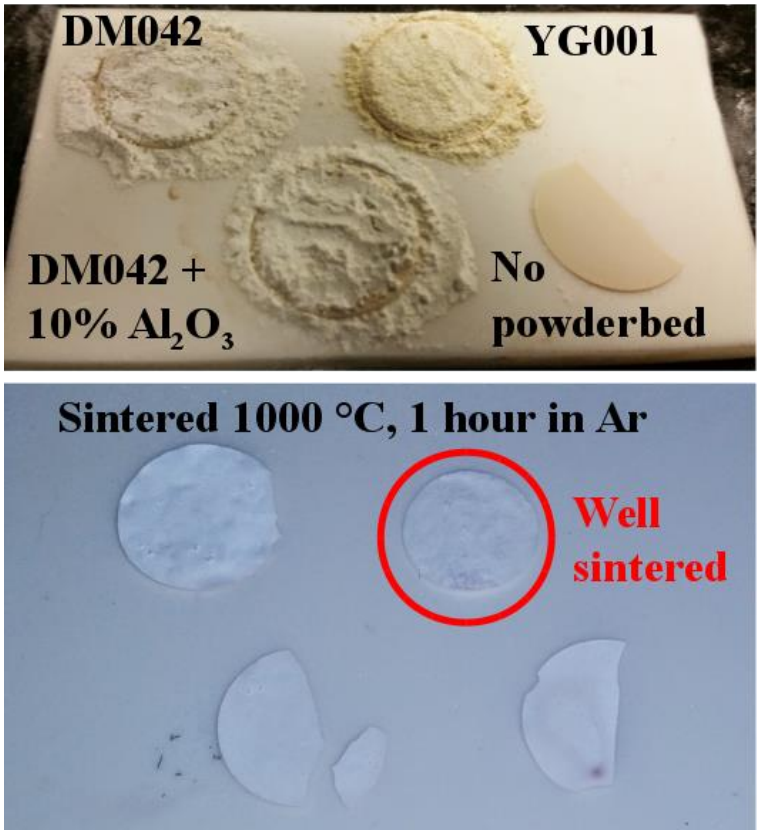

Figure 61. Photographs of trilayers set up for sintering (top) and after sintering (bottom). The sample covered in the YG001 powderbed sintered well and is circled in the bottom image.

5.4.3 - Powderbed lattice parameter

As the original purpose of powderbeds is to confer some protection from lithium volatility in the sintering structure, it could be possible that variations in powderbed lithium content were affecting sintering. However, we did not and still do not (as of writing) have full access to elemental characterization facilities that can quantify lithium content. Garnet lattice parameters derived from Rietveld refinement

performed with TOPAS software on powder X-ray diffraction results have been used as a proxy for lithium content, as all things being equal, higher lithium content likely leads to a larger lattice parameter. Table 25 shows the refinement results on various batches of powderbed used in sintering garnets.

Powder synthesis batch	Stoichiometry	Lattice parameter (Å)	Sintered well as powderbed?
YW001	$Li_7La_{2.75}Ca_{0.25}Zr_{1.75}Nb_{0.25}O_{12}$	13.062	Yes
YG002	$Li_7La_{2.75}Ca_{0.25}Zr_{1.75}Nb_{0.25}O_{12}$	13.035	Yes
DM020	$Li_{6.75}La_{2.75}Ca_{0.25}Zr_{1.5}Nb_{0.5}O_{12}$	13.032	Yes
GH003	$Li_{6.75}La_{2.75}Ca_{0.25}Zr_{1.5}Nb_{0.5}O_{12}$	13.027	Yes
YG002 re-calcined	$Li_7La_{2.75}Ca_{0.25}Zr_{1.75}Nb_{0.25}O_{12}$	12.955	No
DM049	$Li_{6.75}La_{2.75}Ca_{0.25}Zr_{1.5}Nb_{0.5}O_{12}$	12.923	No
DM042	$Li_{6.75}La_{2.75}Ca_{0.25}Zr_{1.5}Nb_{0.5}O_{12}$	12.916	No
DM030	$Li_{6.75}La_{2.75}Ca_{0.25}Zr_{1.5}Nb_{0.5}O_{12}$	12.907	No

Table 25. Summary of the various powderbed batches used for sintering trilayer garnet sorted by lattice parameter. Rows are colored according to whether the powderbed promoted sintering (green) or not (red).

The powderbed batches that led to successful sintering are highlighted in green and the batches that led to poor sintering are highlighted in red. It can be seen that the larger lattice parameter batches proved to be good powderbeds, supporting the hypothesis that high lithium content in the powderbed is important for sintering garnet trilayers.

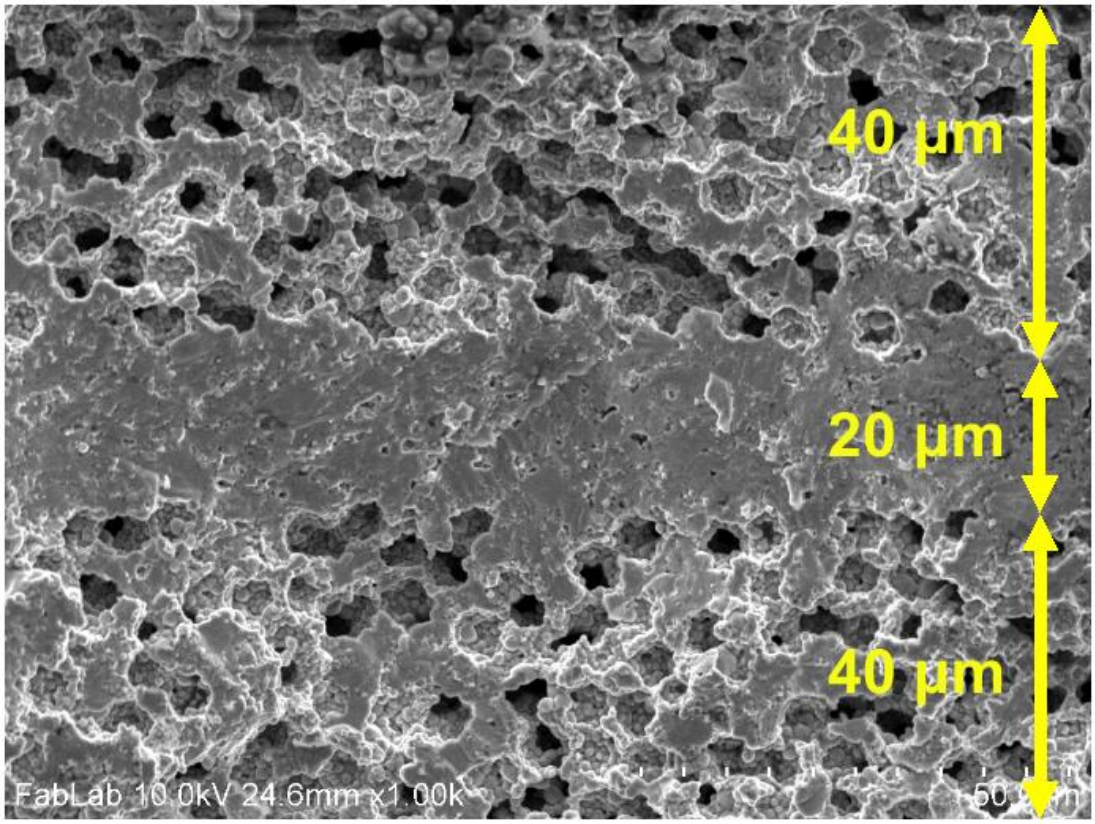

Figure 62. SEM image of a triple layer LLCZN garnet sintered at 1000 °C for 30 minutes in argon.

Reproducibility of garnet trilayer fabrication begins with consistent garnet synthesis. For this reason, garnet synthesis has been characterized at every step. Specifically, we were interested in discovering the cause of lattice parameter variation, as it has been determined that high lattice parameter garnet is required for high density sintering.

A 100 gram batch of $Li_{6.75}La_{2.75}Ca_{0.25}Zr_{1.5}Nb_{0.5}O_{12}$ was produced. After calcining, as sample was taken for XRD before and after ball milling. A diagram of this process and the resulting XRD patterns can be seen in Figure 63. It can be seen that the lattice parameter increased by roughly 10 pm. Lattice parameter change with

ball mass does have some precedent in literature[110,111]. This amount of lattice parameter increase after ball milling was subsequently measured in several samples ruling out an aberrant batch. It is currently unclear what is causing the expansion, but a mass gain was also associated with this lattice parameter. The mass of the powder was measured before ball milling in anhydrous isopropanol and after milling and drying at 100 ºC for 24 hours. A mass gain of about 10% was measured. Neither effect was seen in a dry milled sample or a sample soaked but not milled in isopropanol, which may indicate a reaction milling-driven between garnet and isopropanol. Future work should include studies to identify any surface phases which may have formed. X-ray photoelectron spectroscopy (XPS) would identify compositional and bonding changes. Raman, UV-VIS, or FTIR spectroscopy may also give some information on surface group which may have formed.

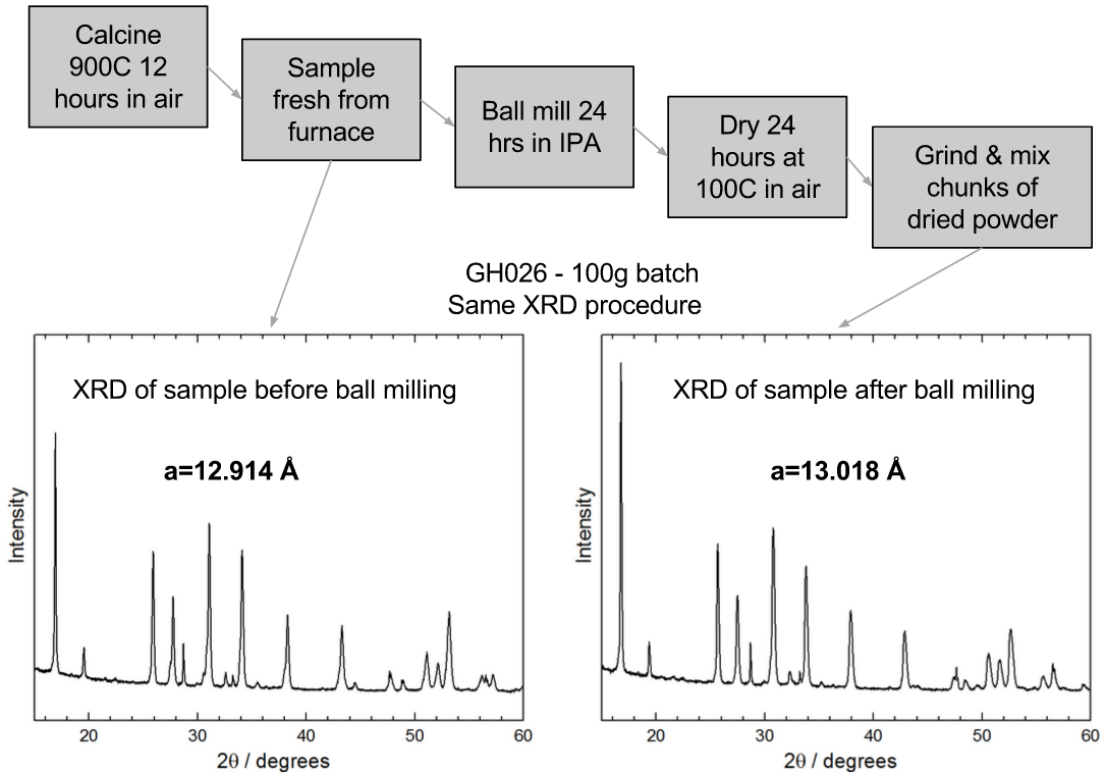

Figure 63. Diagram of synthesis process (top), XRD of 100g LLCZN batch before milling (bottom left) and after milling (bottom right).

The zoomed peaks in Figure 64 show that this is not a fitting artifact or systematic error in the XRD, as the garnet peaks shift whereas the impurity peaks do not. Clearly the $La_2Zr_2O_7$ phase is not being affected by milling while the garnet phase is affected.

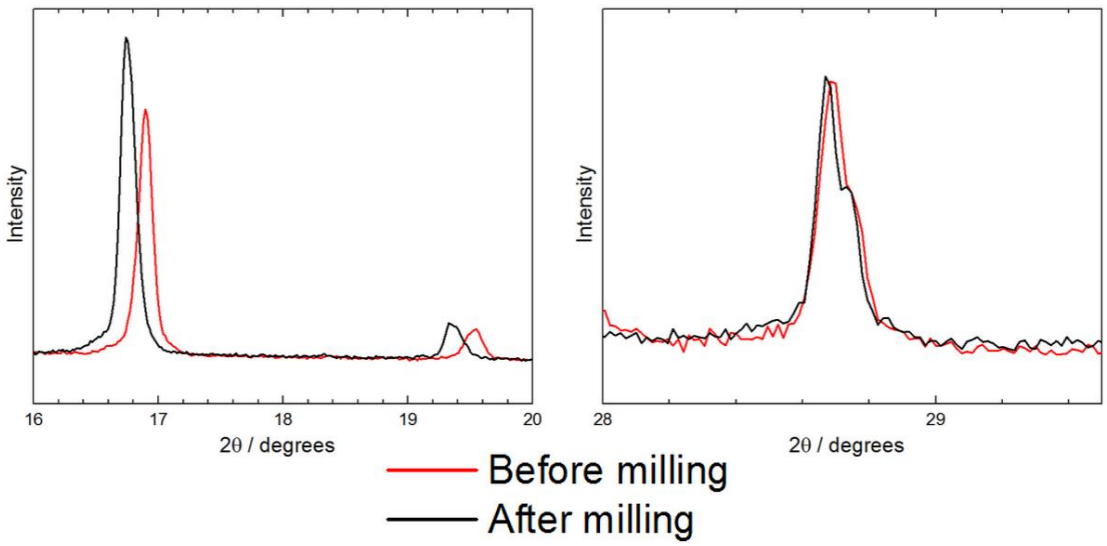

Figure 64. X-ray diffraction patterns of LLCZN batch before milling (red) and after milling (black), with zoomed views showing some characteristic garnet peaks (left) and LZO impurity peaks (right).

In the same vein, scale up of material synthesis allows the focus to remain on fabrication consistency. As larger batches of powder can produce more batches of tape, inconsistencies in the resultant trilayers can be isolated to fabrication processes instead of tape batch. The 100 gram batch in Figure 63 showed a larger than usual amount of $La_2Zr_2O_7$. Figure 65 shows the XRD after calcining the same conditions, 12 hours at 900C, and ball milling for a 500 gram batch. This pattern shows a very strong peak at 29 degrees, indicating significant presence of $La_2Zr_2O_7$. The presence of this phase can sometimes indicate lithium deficiency. However it is unlikely that a larger batch would lose more lithium than a smaller batch, as the larger batch has a significantly lower surface area to volume ratio. To test the possibility that the reaction was only partially complete, the same powder was recalcined and remilled, but resulted in further degradation of the garnet phase and growth of the $La_2Zr_2O_7$ phase. It is still unknown why larger batches produce less pure garnet.

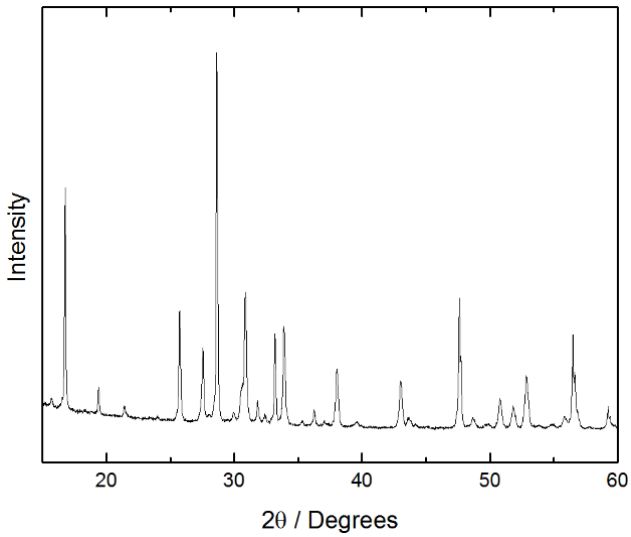

Figure 65. XRD pattern of 500g batch of LLCZN after calcining and milling.

5.4.5 - Tapecasting particle size effect

At one point, trilayer cells began to crumble in the furnace during sintering, despite no intentional changes in the process. One such cell can be seen in Figure 66.

Figure 66. Photograph of sintered trilayer cell.

This problem was isolated to the batch of tape produced - one tape batch using one batch of garnet powder worked and another tape batch using another batch of

garnet powder did not work. Unfortunately, the garnet powder batches at the time were not large enough to make multiple tapes from the same batch, so isolating one variable was difficult in this case. Therefore, the powders and tape were characterized as much as possible at each stage. The garnet powder batches were characterized with XRD, DLS and BET. XRD and SEM was performed on tapes were performed on green tapes, presintered cell punchouts and presintered then sintered cells using the same powderbed.

Through DLS and BET, it was determined that the particle size in the garnet powder used in the "bad" tapes was roughly 25% smaller with about 15% more surface area. This affects the ideal tapecasting recipe, as smaller particles require more solvent, binder, dispersant and fish oil, due to the higher surface area.

The results of the XRD and Rietveld refinements are shown Figure 67. Interestingly, both tapes showed significant $La_2Zr_2O_7$ impurity phase (labelled "LZO") after presintering, which reabsorbs into the garnet phase during sintering. However, both batches are reasonably similar, indicating that phase was not the problem.

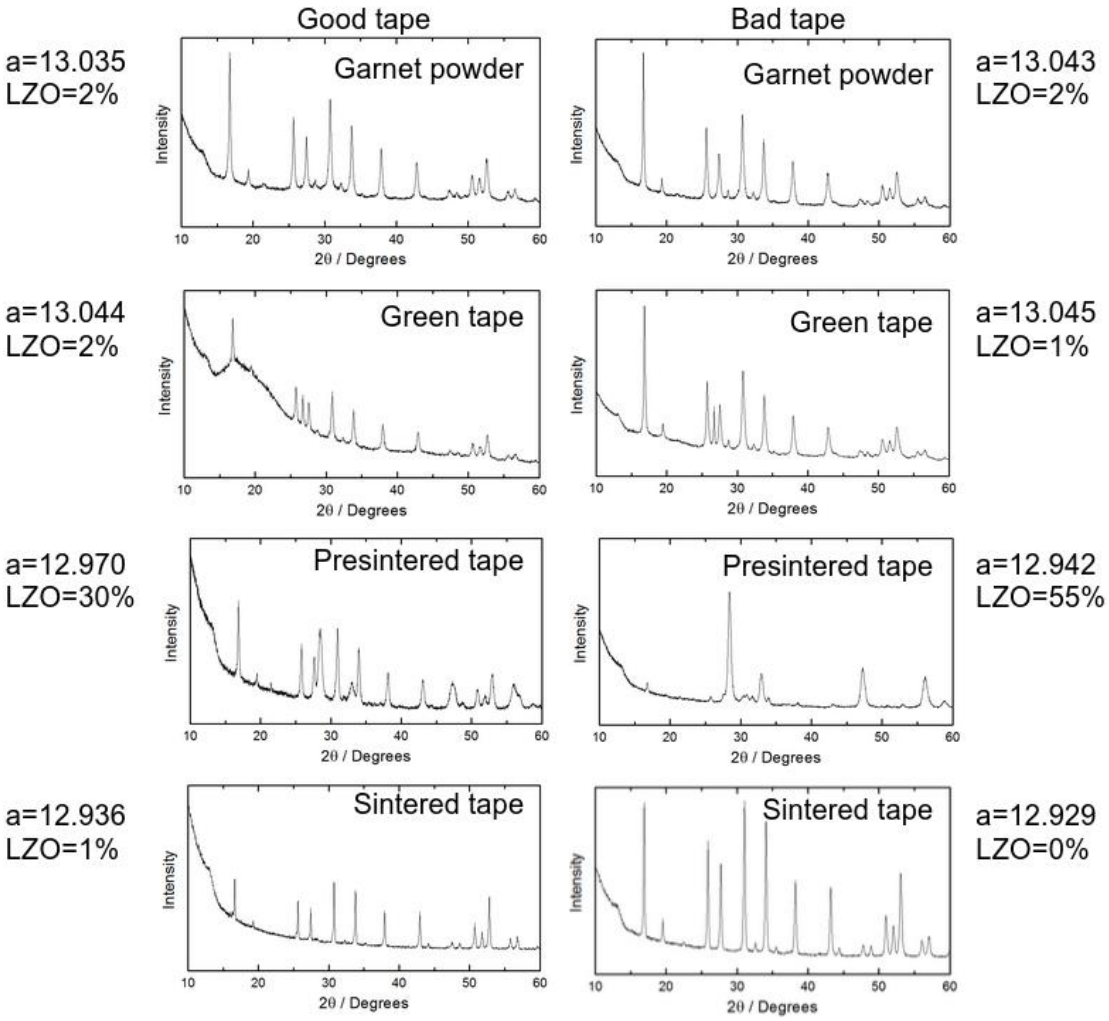

Figure 67. XRD of two batches of garnet tape throughout the fabrication process.

SEM images of the tapes at each stage of fabrication can be seen in Figure 68. There does not seem to be any obvious difference until the sintered cells.

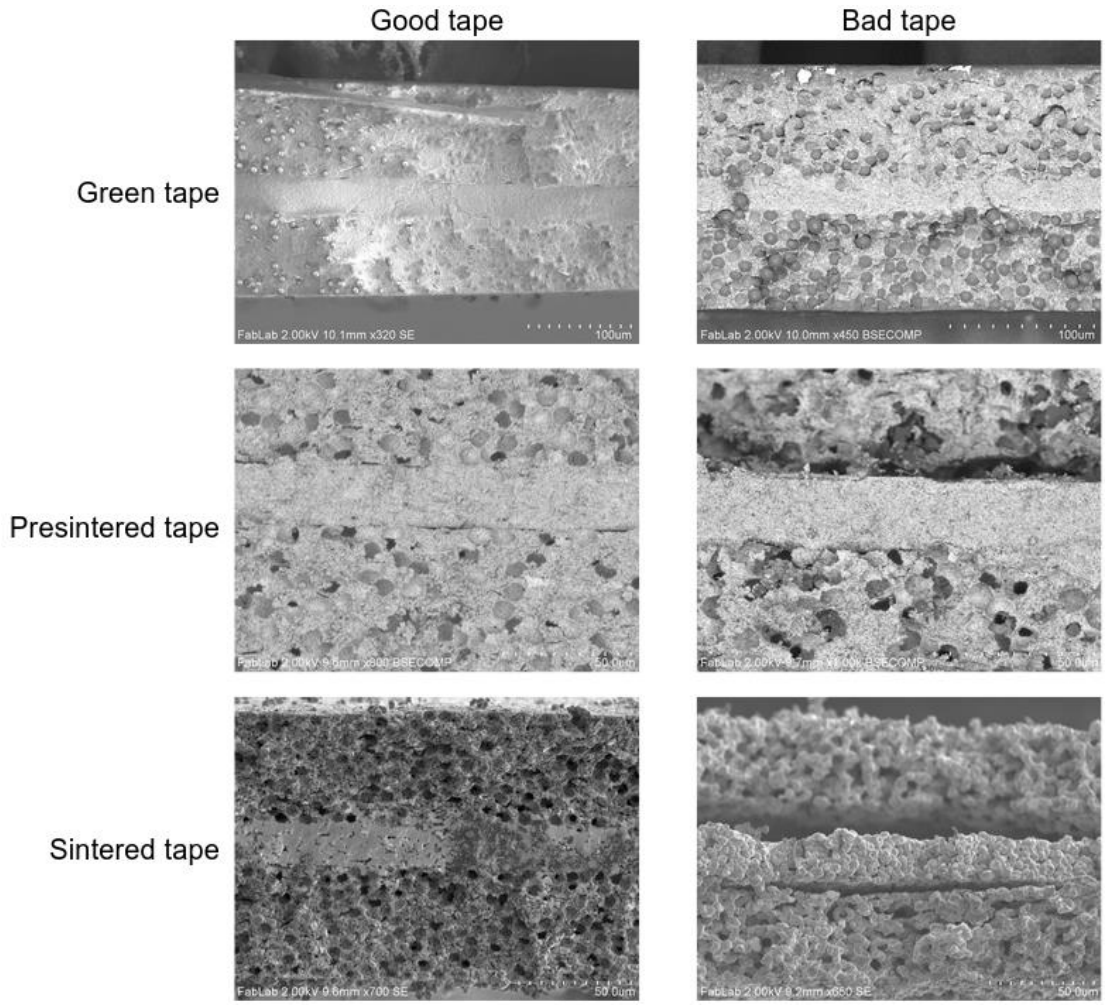

Figure 68. SEM images of two tapes as green tapes, after presintering and after sintering

From these results, it was hypothesized that the problem arose from the changing particle size. It was noted that the tape slurry of the "bad" batch had formed a gel after the addition of PVB, likely due to the smaller particle size of the powder. This was originally not considered problematic, as addition of more solvent quickly returned the slurry to the proper liquid consistency. To test this, the same recipe was prepared but with the additional solvent added before adding PVB. As an added data point, an old recipe for a much older successful tape mixed using the small particle

size batch of powder. The tape slurry with increased solvent casted successfully and the older recipe formed a gel, confirming the hypothesis. Since this discovery, tape slurries using new garnet batches were checked frequently after the addition of PVB and solvent was added if needed before gel was formed.

5.4.5 - Impact of aluminum and lithium content

Lithium garnet powder is normally calcined in Al_2O_3 crucibles. After several calcination uses, these crucibles change color slightly, possibly indicating that the Al_2O_3 has been partially lithiated. This could influence the rate of aluminum diffusion into the garnet powder or the rate of lithium diffusion out of the garnet. The effect of lithium and aluminum content on garnet has been characterized in other compositions but never on this composition. Previous studies on lithium and aluminum content have not considered the potential dependence of these two factors on each other. If lithium volatilizes from the lattice during calcination, this may increase the driving force for aluminum to enter the lattice, as sites become available. Conversely, as aluminum enters the lattice from the crucible, it is possible that lithium is pushed out to maintain charge neutrality. A study was developed to investigate these effects, diagrammed in Figure 69. As shown, LLCZN compositions with varying amounts of excess lithium hydroxide were calcined in an Al_2O_3 crucible and LLCZN compositions with varying amounts of Al_2O_3 added were calcined in an MgO crucible.

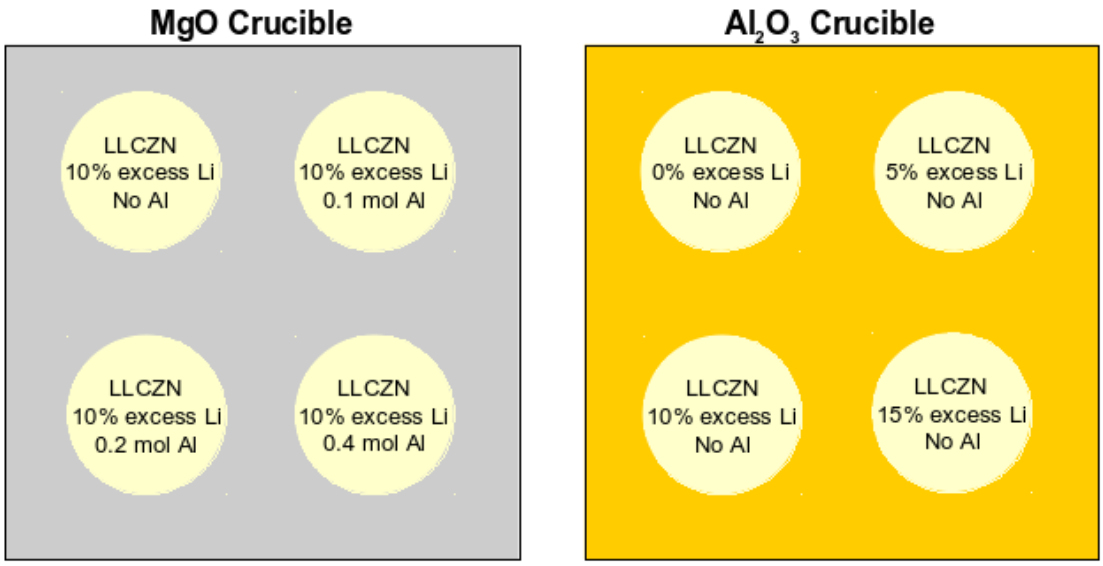

Figure 69. Experimental design to determine effect of lithium and aluminum content during calcination.

A composition study using inductively coupled plasma mass spectrometry (ICP-MS) or optical emission spectrometry (ICP-OES). Unfortunately, both machines intended for in this study continue to be inoperable and elemental composition results are not complete. However, XRD was done on some samples before milling and all samples after milling for 24 hours. It can be seen that there seems to be little if any correlation between lattice parameter due to Al_2O_3 or LiOH in weigh out. Lattice parameter was much more significantly affected by ball milling, which confirms earlier results.

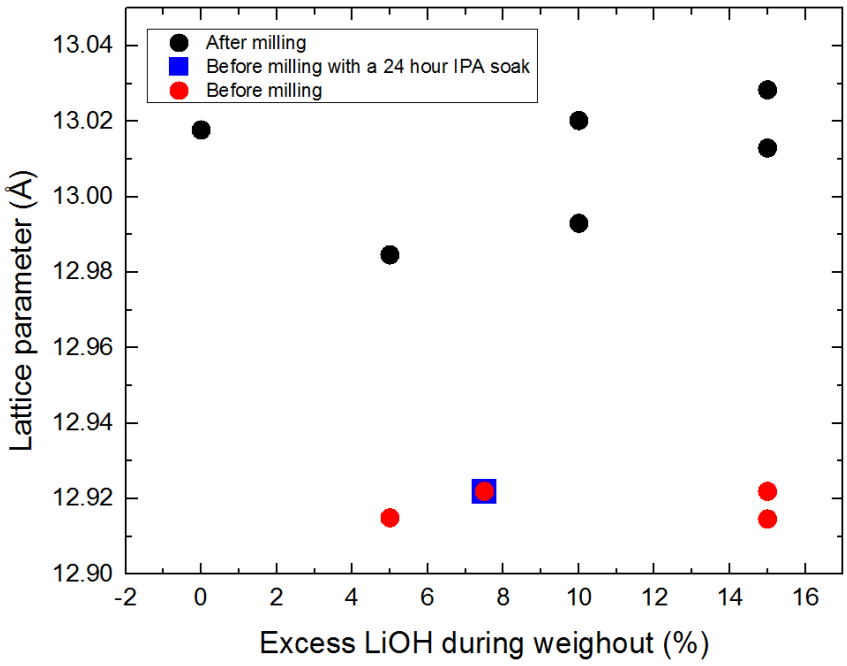

Figure 70. Lattice parameter vs. excess LiOH of samples sintered in Al_2O_3 crucible.

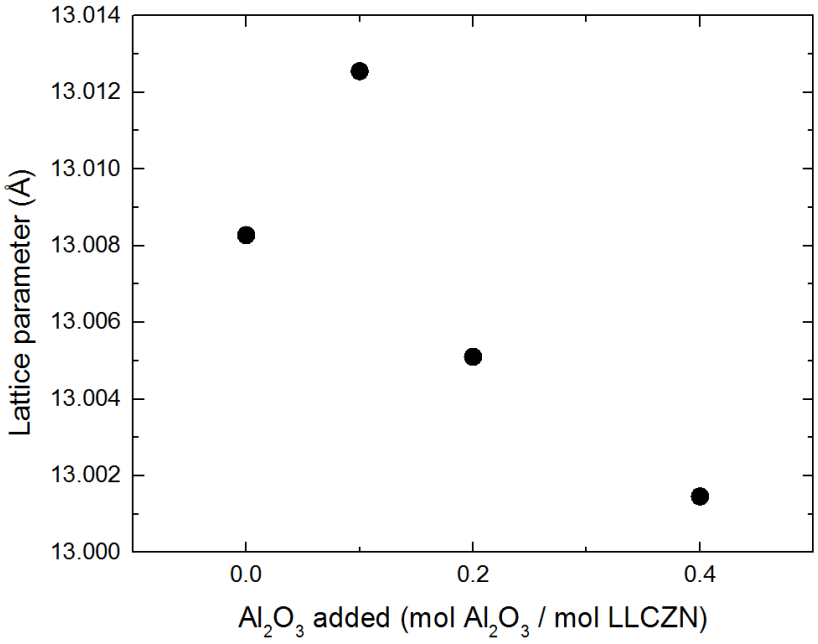

Figure 71. Lattice parameter vs. added Al_2O_3 of samples sintered in MgO crucible.

5.4 - Improvement of porosity interconnectivity

Experiments were performed to increase the degree of open porosity in the trilayer. Only interconnected pores with an electronic path to the current collector will be electrochemically active. Furthermore, only pores with sufficiently sized connections are able to be filled with electrode material. In an effort to improve interconnectivity of the pores, we have tested graphite as a pore former based on the results of SOFC publications showing excellent microstructure for this purpose. Graphite does not finish burning out until above 800 °C, which preserves the integrity of the pores and allows a continual off-gassing which forces the connections in the pores to stay open. Graphite also allows for better pore former mixing in the slurry because, unlike the PMMA spheres we had been using, graphite is completely insoluble in toluene, one of the solvents used for tapecasting. This allows a much earlier addition of pore former to the slurry, enabling full distribution of the pore former. The resulting sintered tape can be seen in Figure 72, after sintering at 950 °C for 5 hours in O_2.

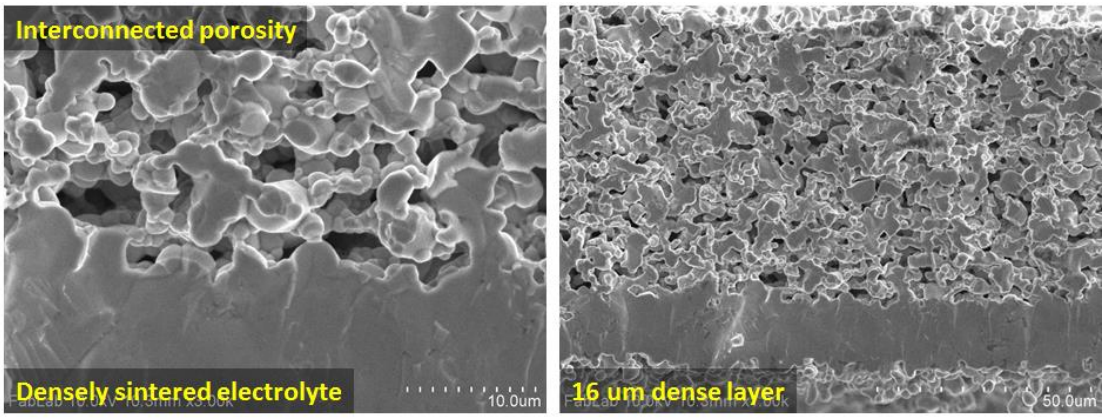

Figure 72. SEM images of sintered trilayers using new graphite pore former recipe showing excellent sintering and fully interconnected pores.

This microstructure represents nearly 100% open porosity amongst a continuous garnet structure. As an added benefit, the dense layers of trilayer tapes with graphite pore former seem to sinter better than tapes with PMMA pore former. This may be due to the delayed burnout of the pore former helping to retain lithium during sintering.

5.5 - Nondestructive impedance measurement of sintered trilayers

An apparatus for nondestructive impedance measurement of lithium garnet cells was built to ensure trilayers were conductive before use in a battery. The apparatus was designed to apply a firm, repeatable compression on soft conductive carbon sponges sandwiching a sintered garnet triple layer. The depth of the hole in the plastic apparatus is sized precisely to allow the carbon sponges to rise roughly 1 mm above the wall of the hole, providing roughly 1 mm of compression on each carbon sponge when the apparatus is fully assembled and tightened. Behind the carbon sponges are stainless steel current collectors connected to silver wires, allowing a four wire impedance measurement. A schematic of this setup can be seen in Figure 73a. A photograph of the apparatus can be seen open in Figure 73b and assembled in Figure 73c.

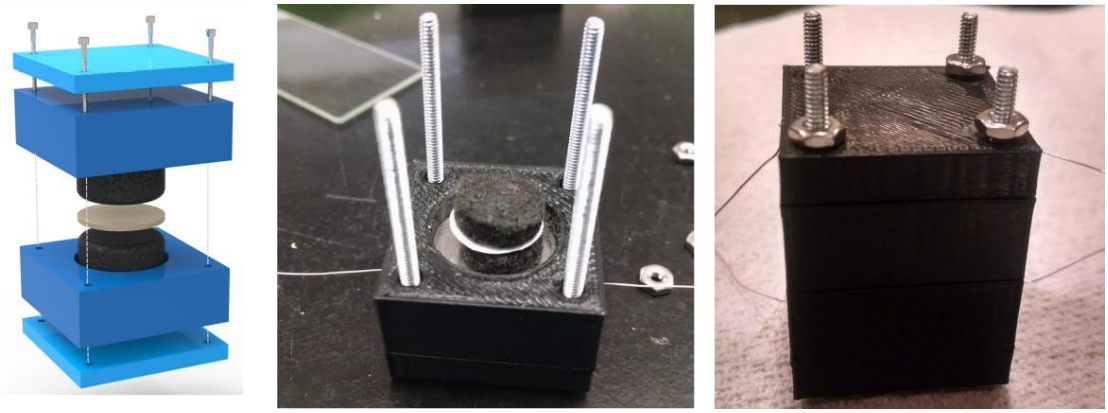

Figure 73. Nondestructive impedance measurement apparatus (a) diagram and (b) photograph open and (c) assembled.

Assembling the apparatus without a triple layer allows the measurement of a null impedance. The null impedance for the apparatus at room temperature can be seen in Figure 74a. This null is used for measurements of triple layers. The impedance measurements of a triple layer left in air for several weeks and a fresh one are shown in Figure 74b. It can be seen that the fresh cell is higher conductivity than the aged cell.

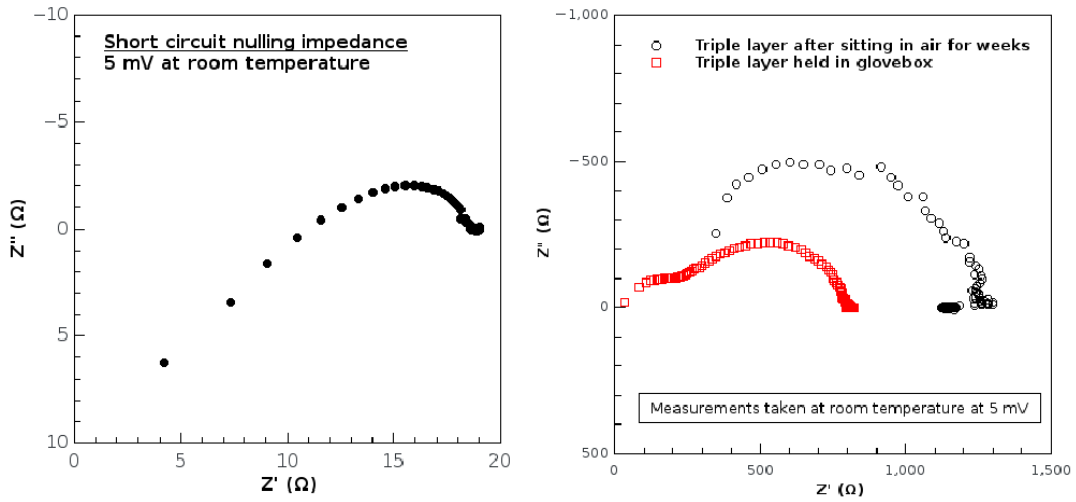

Figure 74. Impedance spectra of (a) apparatus short circuit null and (b) aged and fresh triple layers.

Figure 75 shows a photograph of an uncracked cell after impedance testing in the apparatus. While some tested cells cracked, the stronger, flatter ones survived. In addition to nondestructive impedance measurements, this provides an initial benchmark for cell strength and flatness as well.

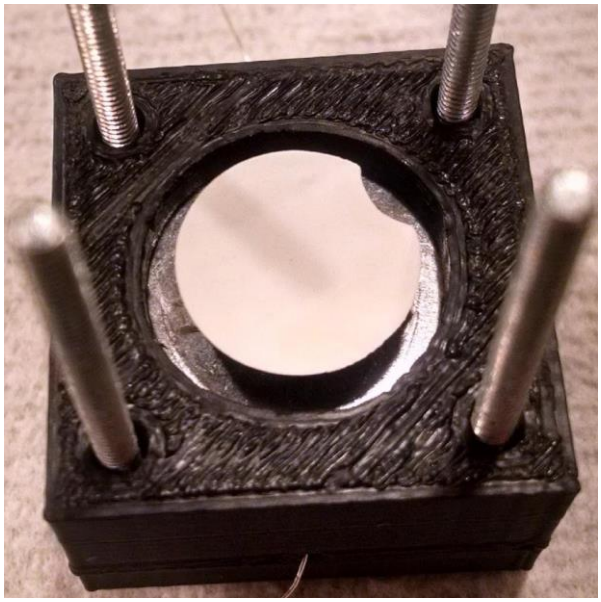

Figure 75. Photograph of intact triple layer garnet after nondestructive impedance testing.

5.5 - Measuring & improving flatness of trilayers

Flatness of the trilayer is an important metric for the fabrication of our solid state batteries. A flatter cell is significantly more resistant to compressive forces, allowing more forceful infiltration of electrodes and higher pressure from current collector contact. It also allows closer stacking of cells in stacks.

In the pursuit of flatter cells, we first had to develop a nondestructive flatness measurement. The Keyence LK-H082 Ultra High-Speed/High-Accuracy Laser Displacement Sensor attachment of UMERC's new 3D printer is capable of measuring sample topology with resolution better than 20 um in the x and y directions and about 1 um in the z direction. We have started using this device to measure the topology of our sintered 1 cm diameter trilayers.

The first scan, shown as a colormap in Figure 76, represents a grid scan of a cell sintered on a dense Al_2O_3 plate with a light powderbed on top and bottom, covered by a porous Al_2O_3 block. The inset shows a photograph of the same cell. The thickness of the cell is calculated by cutting out the background of the scan using an increasing cutoff until the shape of the trilayer is affected. The accuracy of this method has been confirmed with SEM to within about 10-15 um. All data analysis for these measurements has been performed in MATLAB.

It can be seen in Figure 76 that the cell is 120 um with a peak height of 802 um. At this point, it is important to begin developing a measure for flatness. In this vein, there are several approaches that may be useful:

- Difference: $Peak\ height\ -Thickness$
- Normalized Difference: $\frac{Peak\ height\ -Thickness}{Thickness}$
- Standard Deviation: $Standard\ deviation\ of\ laser\ scan\ values$
- Relative Standard Deviation: $\frac{Standard\ deviation}{Thickness}$

As we test cells, we are correlating these results to the processing conditions and survival in the impedance measurement. It remains to be seen which of these metrics is the most useful for indicating the ability of the cell to withstand a compressive force or stack compactly.

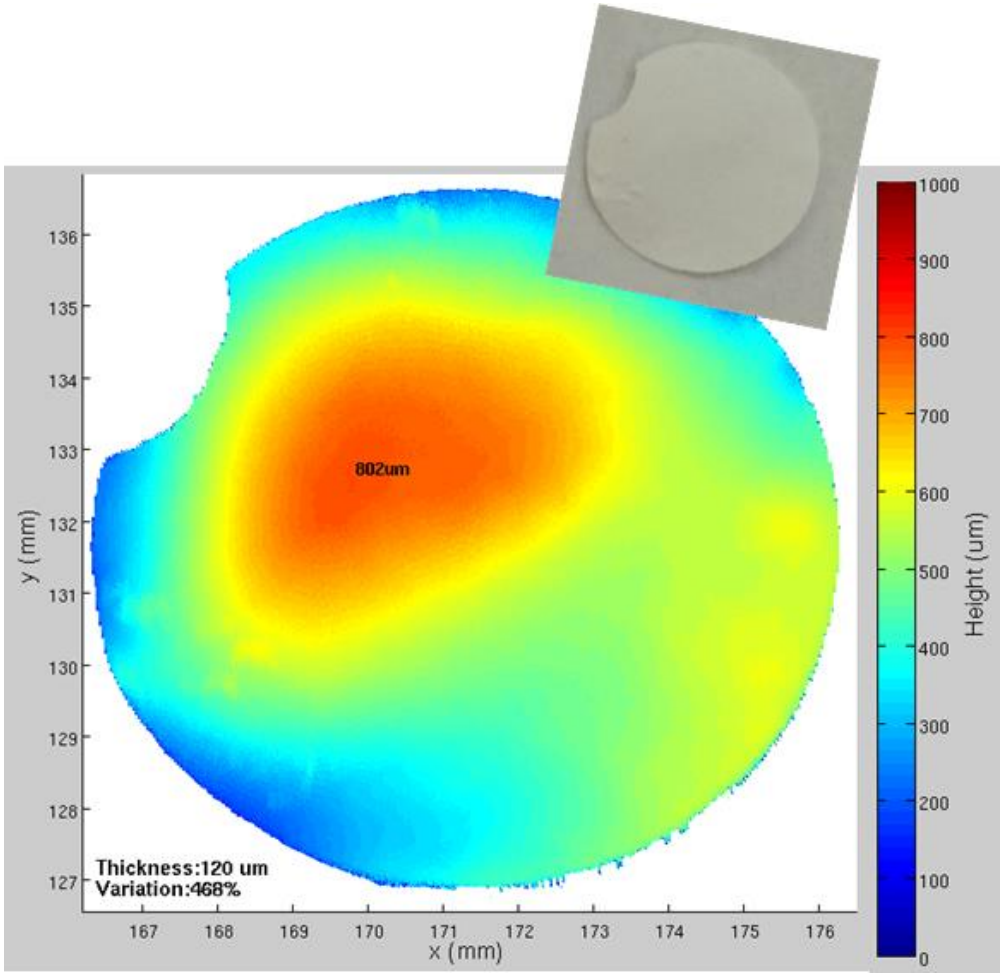

Figure 76. Colormap of grid scanned trilayer sintered with starting point sintering setup.

In order to obtain an accurate measure, the z height of the sample holder must be absolutely zeroed and leveled. This is difficult to achieve by leveling the sample holder but can be achieved by removing the background during data analysis. The

data points of the grid scan can be separated and assigned to trilayer or background layers. A curve can be fit to the background layer, representing the sample holder, to extrapolate the location of the sample holder beneath the sample. This curve is used to subtract the background from the trilayer data points. The fitting of the background data can be seen in Figure 77. This operation is performed for every trilayer scanned. Also apparent are the outliers created via edge effects in the scanning. These points are removed with a high and low cutoff of data points, which is performed computationally for each cell after scanning.

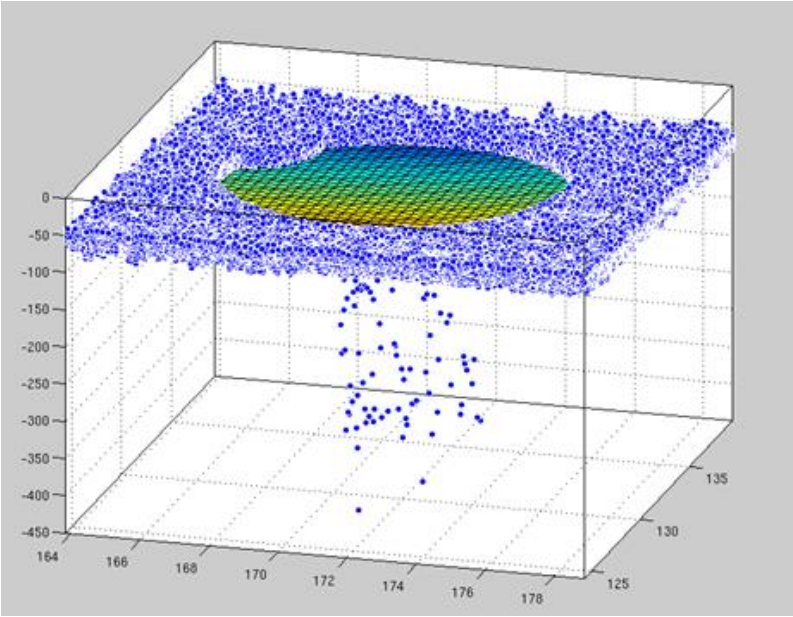

Figure 77. 3D plot of a grid scan background and the curve fit to the background.

It was theorized that one cause of poor flatness is uneven sintering due to variations in packing in the powderbed. This was tested by sintering two trilayers simultaneously, one with a full powderbed and one with a partial powderbed. The grid scans of these cells are shown in Figure 78 on the right and left, respectively. The part of the cell without powderbed (circled in red) is clearly raised and causes a 46%

relative standard deviation. This confirms the hypothesis and indicates that a more consistent powderbed may lead to even flatter cells.

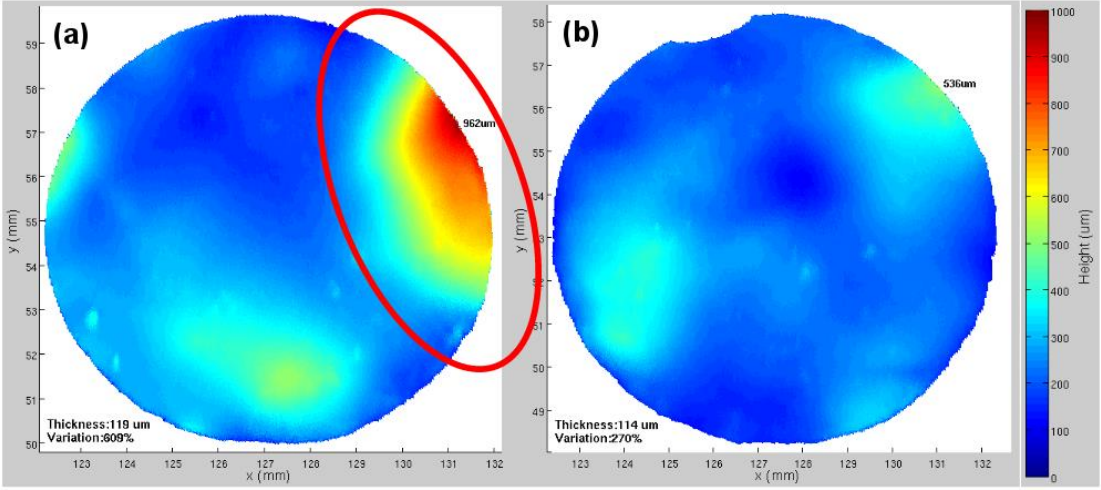

Figure 78. Colormap of grid scans of two cells sintered in the same furnace run with a partial powderbed (a) and a full powderbed (b).

We attempted to fabricate flatter cells in two ways. For the first cell, shown on the left of Figure 79, the powderbed was hand ground with mortar and pestle before use, breaking up agglomerates and allowing a more consistent powderbed to be laid out. For the second cell, an equivalent amount of powder was pressed into two pellets, which were sandwiched around the cell with a small amount of powder around the gaps between the pellets. Both of these cells sintered much more consistently than previous cells, showing 17% and 29% normalized difference, respectively.

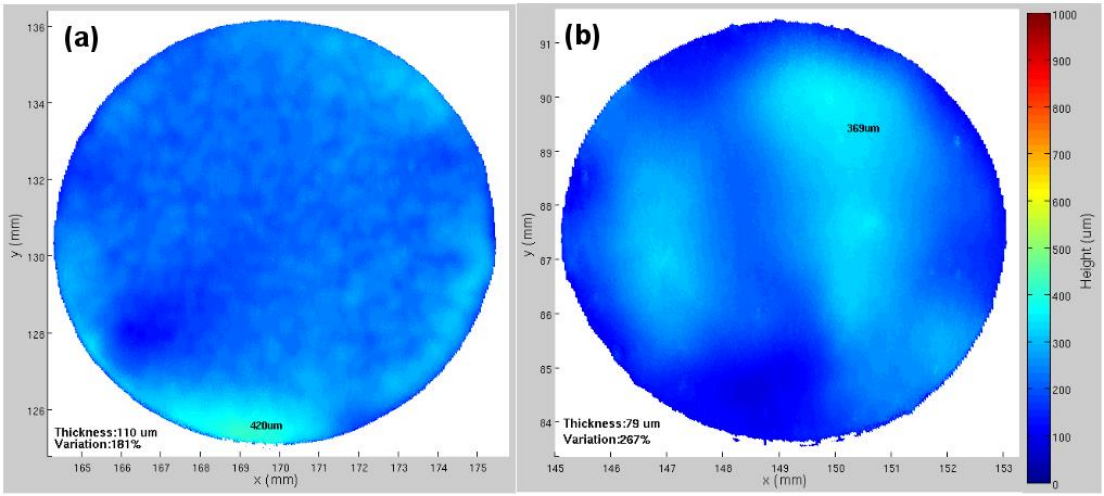

Figure 79. Colormap of grid scans of two cells sintered (a) a freshly ground powderbed and (b) a pelletized powderbed.

As mentioned previously, the current thickness variation calculation may be inadequate for properly quantifying flatness for our purposes. The standard deviation of the grid scan z values can be calculated to determine a thickness-independent metric. Again, though, this method has limitations. The average variation in cell flatness is likely less important than the maximum deviation, as this is the most likely to cause cracking. The absolute difference between peak height and thickness of the cell is more representative of the worst point of the cell and the most likely to fracture and interfere with stacking. One last relevant metric is the relative standard deviation, or the standard deviation divided by the mean. Again, this gives a percentage, but is now in terms of the variability versus thickness of the cell. All these calculations are presented in Table 26, sorted by figure order. Data cells are colored according to rank in column from lightest to darkest representing best to worst.

Note	Eqn. 1 Value	Difference	Standard Deviation	Relative Standard Deviation
Initial conditions	468%	682 um	139 um	27%
Partial powderbed	609%	843 um	143 um	46%
Full powderbed	270%	422 um	65 um	27%
Ground powderbed	181%	310 um	41 um	17%
Pelletized powderbed	267%	290 um	66 um	29%

Table 26. Flatness of various trilayer scans as calculated by various methods. Cells are colored according to their rank in the column with lightest representing the most flat and darkest representing the least flat.

Another more nuanced approach may be to look at the gradient of the grid scan, as this will show the areas of greatest curvature, which are also the likeliest points of fracture in compression. The gradients of the previously shown grid scans are plotted in Figure 80.

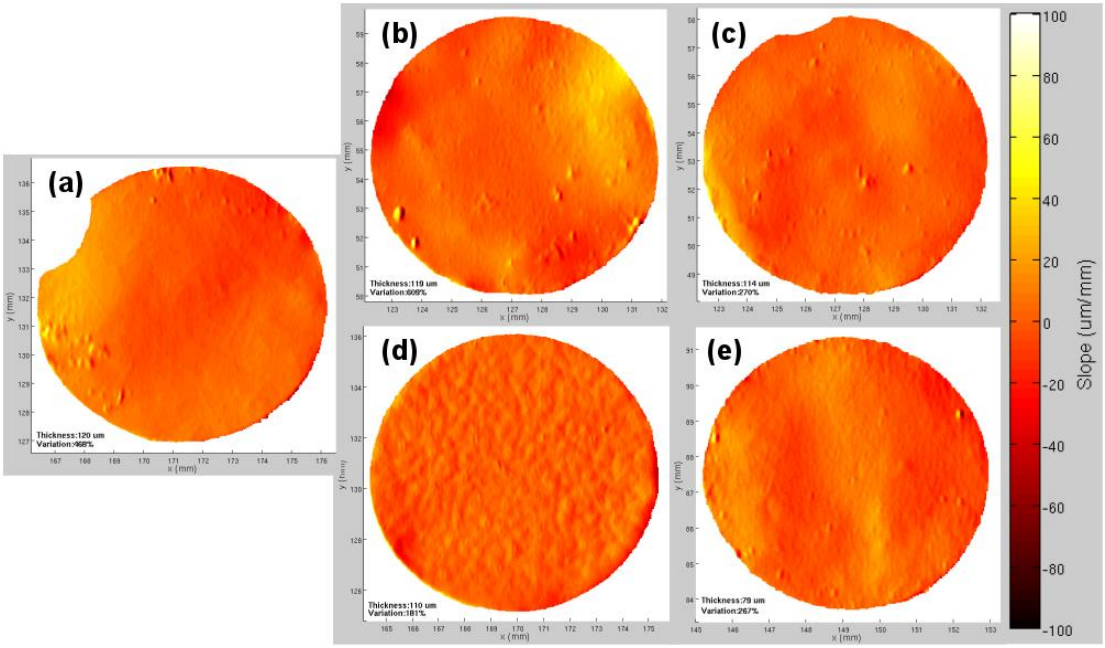

Figure 80. Plots of the gradients of the previously shown grid scans in Figures (a) 4, (b) 6a, (c) 6b, (d) 7a, (e) 7b.

Cell flatness improvements continued. Figure 81 shows a sampling of cells ordered chronologically. Most cells produced now are under 20% RSD.

	Variation Thickness	Difference (um)	Standard Deviation (um)	Relative Standard Deviation
Cell 1	468%	682	139	27%
Cell 2	609%	843	143	46%
Cell 3	270%	422	65	27%
Cell 4	181%	310	41	17%
Cell 5	267%	290	66	29%
Cell 6	231%	282	47	19%
Cell 7	143%	196	33	15%

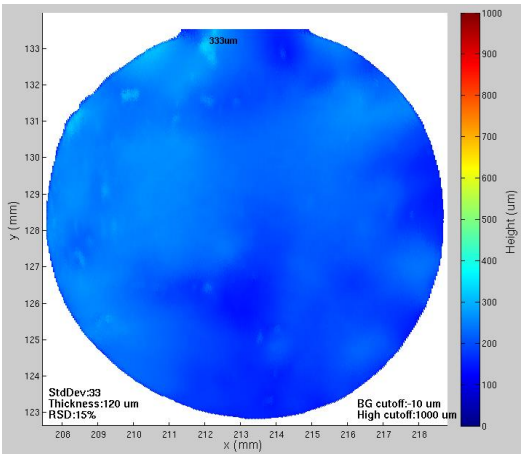

Figure 81. (left) Table of various cell flatness measures ordered chronologically and (right) a colormap of the scan for Cell 7.

Chapter 6: Fabrication and Testing of Li-Garnet Symmetric Cell and Battery

In this Chapter, a solid electrolyte architecture as designed in Chapter 4 and developed in Chapter 5 is constructed based on a $Li_{6.75}La_{2.75}Ca_{0.25}Zr_{1.5}Nb_{0.5}O_{12}$ (LLCZN) electrolyte. The demonstrated cell breaks through the barriers imposed by conventional polished planar discs of solid electrolytes. Specifically, a porous-dense-porous trilayer structure was fabricated by tape casting, a roll-to-roll technique conducive to high volume manufacturing. The high density and thin center layer (< 20 μm) effectively blocks dendrites even over hundreds of cycles. The microstructured porous layers, serving as electrode supports, are demonstrated to increase the interfacial surface area available to the electrodes. Together, the resistance of the LLCZN trilayer was measured at an average of 7.6 ohm-cm^2 in a symmetric lithium cell, significantly lower than any other reported literature results. Building on these results, a full cell with a lithium metal anode, LLCZN trilayer electrolyte, and $LiCoO_2$ cathode was cycled 100 cycles without decay and an average ASR of 117 ohm-cm^2. After cycling, the cell was held at open circuit for 24 hours without any voltage fade, demonstrating the absence of a dendrite or short-circuit of any type. These results show a promising path to commercially viable, intrinsically safe lithium batteries with energy densities of >300 Wh/kg and > 1000 Wh/L.

6.1 - Introduction

Since their inception, Li-ion batteries have transformed the market for energy storage. Li-ion technology has a proven track record of delivering high power, high

capacity energy storage devices with extended lifetimes. Indeed, nearly all portable electronic devices use Li-ion batteries, and a majority of electric vehicles use them as well. However, excessively large battery packs are still required for electric vehicles to have acceptable range, and costs remain prohibitively high for most consumers. Currently, Li-ion batteries are limited in energy density, and so more cells are needed to compensate. Despite 25 years of development, commercial Li-ion batteries still do not use the most enticing electrode, lithium metal, which has the highest energy density of any anode for lithium batteries. A lithium anode has an exceptionally high capacity at 3860 mAh g^{-1}, over 10 times higher than a standard graphite electrode at 330 mAh g^{-1}. A lithium metal anode is light and 100% active mass since binders and conductive additives are not needed. However, lithium metal cannot be used with traditional liquid electrolytes because dendrites form on the lithium metal during charging, which eventually penetrate the separator and short circuit the battery, resulting in catastrophic failure.

On the cathode side of the battery, several high voltage materials have been developed over the last decade which could significantly increase battery energy density as well. Once again, commercial development of these cathodes has been hindered by the liquid electrolyte due to insufficient stability at voltages higher than 4.5V[5,112]. A great deal of research effort has been dedicated to finding a new liquid or polymer electrolyte which can satisfy the myriad required properties for Li-ion batteries while increasing the voltage stability window, but few tangible results have made it to market. Indeed, the primary lithium salt used in the liquid electrolyte,

lithium hexafluorophosphate ($LiPF_6$), has remained unchanged since Li-ion batteries were first sold, despite being extremely hazardous, overly sensitive to trace moisture, and difficult to produce and recycle.

Relying on a liquid electrolyte for Li-ion batteries has other limitations as well. For one, liquid electrolytes are composed of organic solvents which are volatile and flammable. The standard electrolyte mixture of carbonate solvents with $LiPF_6$ is reactive, and if heated, can experience a thermal runaway reaction exacerbated by certain electrode materials, causing rupture and possible explosion of the cell. Thus, heavy temperature control systems are required in electric vehicles increasing the weight and cost.

Many researchers have therefore turned their efforts to investigating and developing lithium conductive solid-state electrolytes. Solid electrolytes have the potential to make the first major leap in Li-ion technology since its introduction in 1991 by Sony Corporation. Solid electrolytes, such as $Li_{6.75}La_{2.75}Ca_{0.25}Zr_{1.5}Nb_{0.5}O_{12}$ (LLCZN) and related lithium garnets, are completely nonvolatile by nature, and cannot burn like liquid electrolytes. They are not adversely affected by temperature changes or long-term storage. LLCZN garnet in particular is stable to lithium metal, and has been shown to be electrochemically stable above 6V[30,113,114], which could mean an LLCZN solid electrolyte is the missing link which enables high voltage, high capacity lithium batteries which are intrinsically safe.

Solid state electrolytes do have formidable obstacles on the path to commercial deployment. First, most solid lithium conductors have a lower ionic conductivity than liquid electrolytes at ambient temperatures. Over the last decade, researchers have gone from discovering lithium conducting garnets[24] to much improved compositions with ionic conductivities[30] greater than 1 mS cm^{-1}. While this is a dramatic improvement, the conductivity remains lower than a standard electrolyte with typical conductivity values in the range of 10 mS cm^{-1}. Furthermore, few researchers have found success fabricating high density LLCZN electrolytes less than 200 μms thick. In conjunction with the lower conductivity, the rate of Li^+ cation migration across the long pathway of the thick cell is limited, increasing resistance and reducing power capability. Compounding this issue, a solid electrolyte relies on solid-solid contact with the anode and cathode materials, limiting the points for Li^+ cation transfer from the electrolyte to electrode. This has proven to cause high interfacial impedance, similarly limiting the battery performance. For example, area-specific resistance[49] (ASR) values for LLCZN-lithium metal interfaces have been reported from 109 to 960 ohm-cm^2, compared to ~20 ohms-cm^2 for a full cell commercial Li-ion battery[115].

The authors have developed a method to fabricate a unique "trilayer" architecture of LLCZN garnet, shown in Figure 82, which enables repeated and high efficiency full cell cycling of a solid state Li-ion battery by addressing the features that cause high resistance. The trilayer is produced by a low-cost, easily scalable tapecasting process. At the center of the trilayer design is the thin, but highly dense

center layer. The high density prohibits lithium dendrite formation through the cell and ensures the ionic conductivity is maximized. This layer is less than 20 μm thick, which makes the total resistance of the electrolyte similar to even the most conductive liquid electrolytes. On opposite sides of the dense layer are two porous layers which serve as ionically conductive porous supports for electrodes. The layers also act as supporting structures for the dense layer, increasing its strength. Crucially, these porous layers maximize the contact area with the electrodes, dramatically reducing the interfacial impedance. Ultimately, what has been achieved is a high energy density solid-state lithium battery which can be inexpensively manufactured via traditional methods. It is inherently safe and can be applied in battery packs without the need for cooling systems to prevent thermal runaway or fire-protection systems in case of catastrophic failure. Furthermore, its unprecedented electrochemical stability simultaneously enables the use of a lithium metal anode and high voltage cathodes, paving the way for new battery chemistries beyond conventional Li-ion.

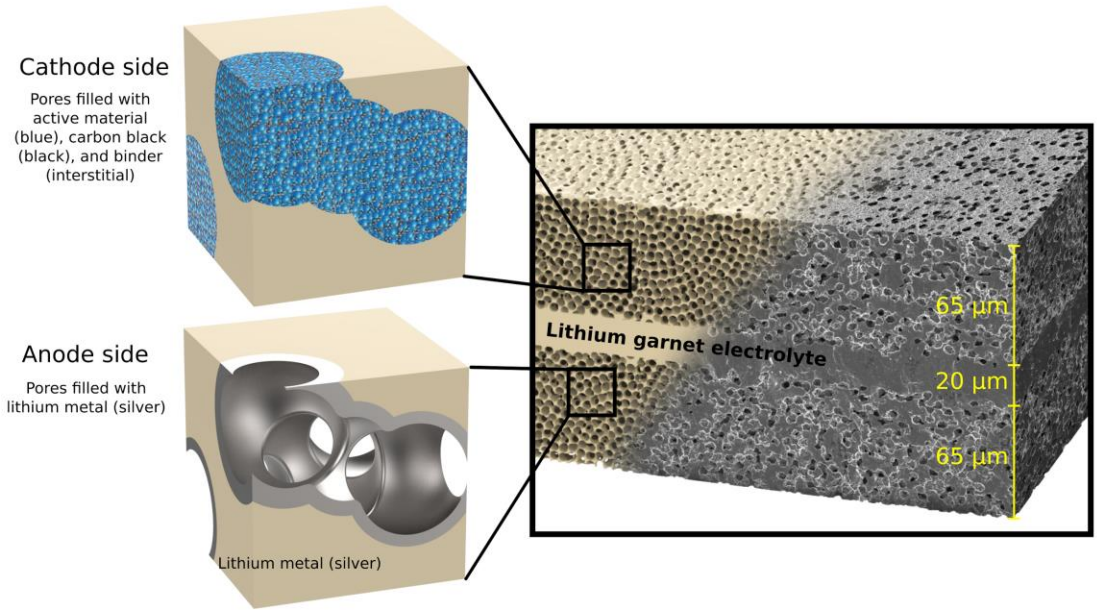

Figure 82. Schematic of lithium garnet 3D solid state cell design as fabricated.

6.2 - Results and Discussion

In order to produce a solid state cell with rate performance competitive with or exceeding traditional cells, the ASR of the cell must be around that of a commercially available 18650 cell (20 ohms-cm^2)[115]. This means that the ASR of the electrolyte alone must be significantly lower to leave headroom for other resistances in the cell. The dependence of the ASR on the center layer thickness for a garnet electrolyte with a typical conductivity between 10^{-4} and 10^{-3} S/cm is shown in Figure 83a. To achieve this goal, trilayer garnet structures were fabricated with a ~20 um thick dense layer.

The capacity of a cell utilizing a planar solid electrolyte, regardless of thickness, would be quite small due to depletion of active material at the interface and limited point contacts causing a bottleneck for Li^+ migration between the electrode

and electrolyte. Indeed, these deleterious effects have been consistently observed when full cells of LLCZN pellets have been fabricated in the literature. Consistently low capacity and low cycle life have been reported due in part to the planar geometry. To maximize capacity and suppress interfacial impedance, a porous network is preferred to drastically increase contact area with the electrode - Figure 83b demonstrates the anode capacity as a function of solid electrolyte support porosity when filled with lithium metal as one example electrode. Based on this, initial trilayers were fabricated with porous layers of ~50% porosity and 40 um thickness to surpass the capacity of a graphitic anode including electrolyte and binder. The lithium loading with the current fabrication process is 4.8 mAh/cm^2 and further optimization will lead to higher porosities and thus higher capacity.

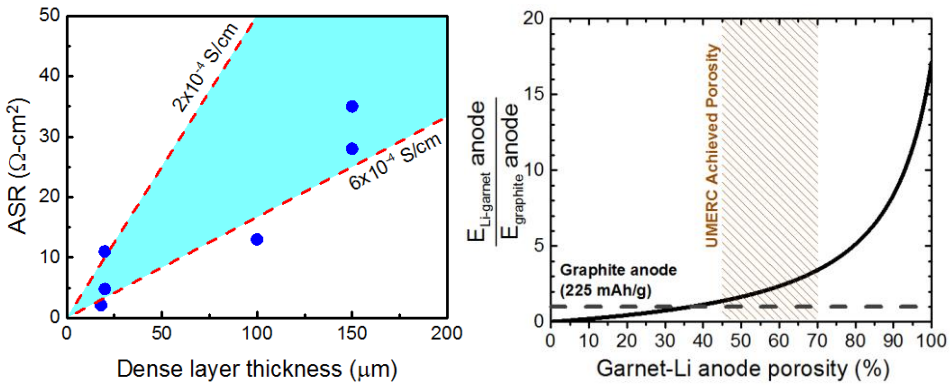

Figure 83. Charts of (a) area specific resistance of lithium garnet by separator thickness and whole-anode capacity of composite garnet-lithium structure.

To fabricate this trilayer structure, the well-established method of tapecasting was used. Tapecasting is a low cost, roll-to-roll method of forming ceramic green bodies by mixing the starting material with a binder(s), plasticizer(s), and solvent(s), and then casting it onto a removable film using a blade at an adjustable height to

control thickness. The resulting flexible tape can achieve significantly higher green body density compared to isostatic pressing, which tremendously improves the sintered density (> 99%). Achieving high sintering density has previously been challenging with lithium garnets and has been a subject of significant study[27,29,116–118]. Different tapes (e.g. tapes with and without porogens) can also be laminated together by simple hot-pressing, creating multilayer structures. Thus, tapecasting allows for tuning of the sintered structure porosity and thickness, such that the final product can be easily tailored to modify pore size/shape, distribution, and surface area to accommodate different electrode characteristics.

SEM images of LLCZN solid electrolyte trilayers after sintering are shown in Figure 84 to demonstrate that porosity can be controlled by varying porogen content to achieve a wide range of design porosities. The 20 μm center layer is highly densified and seamlessly connected to two 40 μm thick layers of porous LLCZN. The high density of the center layer is essential for preventing electrode contact and lithium dendrite growth, while ensuring maximum ionic conductivity. The porous layers comprise a three-dimensional interconnected pore network leading to the surface of the sample, which is essential for maintaining a connected pathway to the current collector. The LLCZN forming this scaffold remains highly dense as well to increase the structural integrity and maintain Li^+ cation conduction pathways across the cell. The overall trilayer structure is exceptionally thin (~100 μm) to minimize the ASR and excess mass, but is also strong enough to be easily handled.

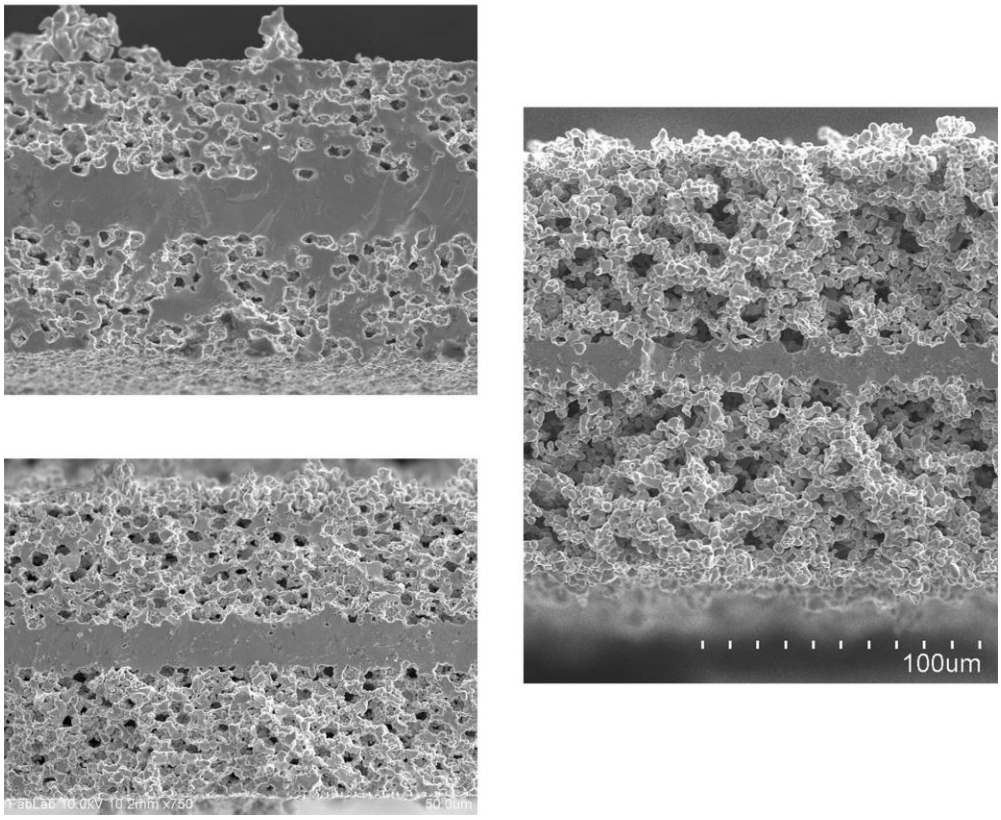

Figure 84. SEM of sintered lithium garnet trilayers at varying porosities and layer thickness, showing the tunability of the tape casting method.

One of the key motivations for using an LLCZN solid electrolyte is its inherent stability to lithium metal. To demonstrate the superior stability of LLCZN to lithium, and compare performance of the garnet trilayer structure to traditional LLCZN electrolyte pellets, the trilayers were prepared for galvanostatic cycling in a lithium-symmetric cell. The porous layers were both infiltrated with molten lithium after ALD surface treatment to enable lithium wetting[50]. The trilayer was then sealed in a coin cell and galvanostatically cycled at various current densities. As seen in Figure 86a, this cell exhibits the surprising ability to cycle at a high current density of up to 10 mA/cm^2, the highest current density achieved for LLCZN to date. For

longer term cycling, the current was reduced to 2.5 mA/cm^2 and cycled for 100 hours, incrementing the depth of discharge as cycling continued. The ASR and voltage response to increasing cycling depths is plotted in Figure 85b. Remarkably, no cycling-related degradation occurred, as the ASR held consistently between 6-8 ohm-cm^2 at all current densities. The ASR experienced a rapid rise only after deep cycling (> 4.9 mAh cm^{-2}), which stripped lithium away from the current collector, causing a loss of connectivity. Interestingly, the theoretical capacity of the ~50% porous layer filled with lithium metal is 4.2 mAh cm^{-2}, indicating that some of the lithium plating and stripping could be occurring beyond the porous layers. This fact opens up the possibility that the cell thickness could be increased if design parameters dictate. A thicker cell is highly desirable as this will increase areal capacity and overall energy density of the full cells.

At the end of cycling, the cell was polarized one direction for an extended time, and then disassembled prior to SEM analysis. Figure 85c and Figure 85d show the symmetric cell trilayer with lithium metal clearly visible within the pores as a smooth, conformal coating. This dark coating is largely only visible on one side of the trilayer, due the last polarization step at the termination of cycling, confirming the presence of metallic lithium. In addition, no dendrites were observed crossing the dense LLCZN boundary in the imaging analysis, showing that LLCZN garnet as thin as 20 μm can reliably block dendrites, even at high current densities.

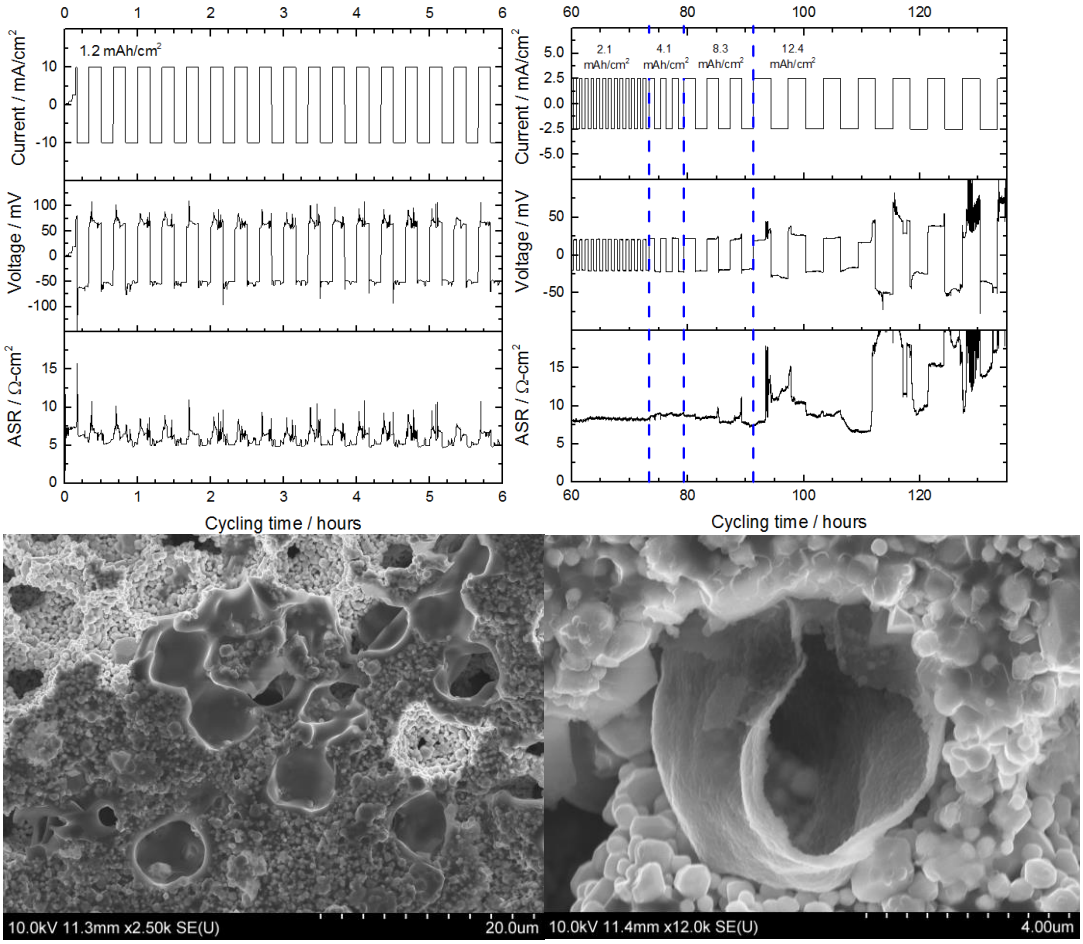

Figure 85. Galvanostatic cycling of lithium garnet triple layers (a) at 10 mA/cm2, (b) at 2.5 mA/cm2 to increasing depths of discharge. SEM of (c) lithium filled pores post-cycling and (d) a close-up of a lithium-filled pore.

Using another LLCZN trilayer, a full cell solid-state battery was assembled by melting lithium onto one side of the trilayer, and applying a cathode mixture to the other side. The cathode was mixed with a polymer electrolyte composed of PVDF-HFP copolymer to promote adhesion to the garnet material. After the mixture was dried on the surface of the garnet, a small amount of standard electrolyte was added to swell the polymer electrolyte mixture, and the full cell was sealed in a coin cell case. As shown in Figure 86a, this cell demonstrated stable cycling with close to 100%

coulombic efficiency and 50 mAh/g on a cathode-mass basis. Remarkably, the cell retained nearly all of its initial capacity over 100 cycles. After 100 cycles, the cell was charged to 4.1 V and allowed to rest for 24 hours, during which time the cell only discharged 0.14 V (0.065 V is due to relaxation from high polarization due to fast cycling, i.e, the ohmic drop), demonstrating that there was no electronic path between electrodes.

This trilayer design shows tremendous promise for the development of high power, high energy density batteries. The results shown here demonstrate the overcoming of many of the most difficult challenges in solid state batteries: the interfacial impedance has been decreased to a negligible level, allowing lithium ion transport through the electrolyte at 10 mA/cm^2 without any cycling decay or dendrite penetration. Significantly higher electrode loading has also been enabled by extending the electrolyte into the third dimension with the porous garnet scaffold. In doing so, a solid-state battery was created with a higher capacity and electrode loading than has been previously achieved, with nearly zero anodic or electrolyte cycling fatigue. Perhaps the most exciting aspect of this discovery is the possibilities it opens for future chemistries. Many high voltage cathode chemistries are not able to be used due to the breakdown of $LiPF_6$ liquid electrolytes above 4.5 V, even with state-of-the-art additives[5,112]. A selection of cathodes are shown in Figure 86b, highlighting the promise of increased cathode flexibility associated with moving to a higher voltage electrolyte. The higher voltage stability of lithium garnet not only allows full cycling of common high voltage cathodes, but it also enables the development of previously unusable predicted cathode chemistries, examples of

which are shown in red circles. All of these chemistries benefit from the removal of electrode dissolution concerns, including sulfur cathodes (polysulfide dissolution)[19] and Mn-containing cathodes (Mn dissolution)[18].

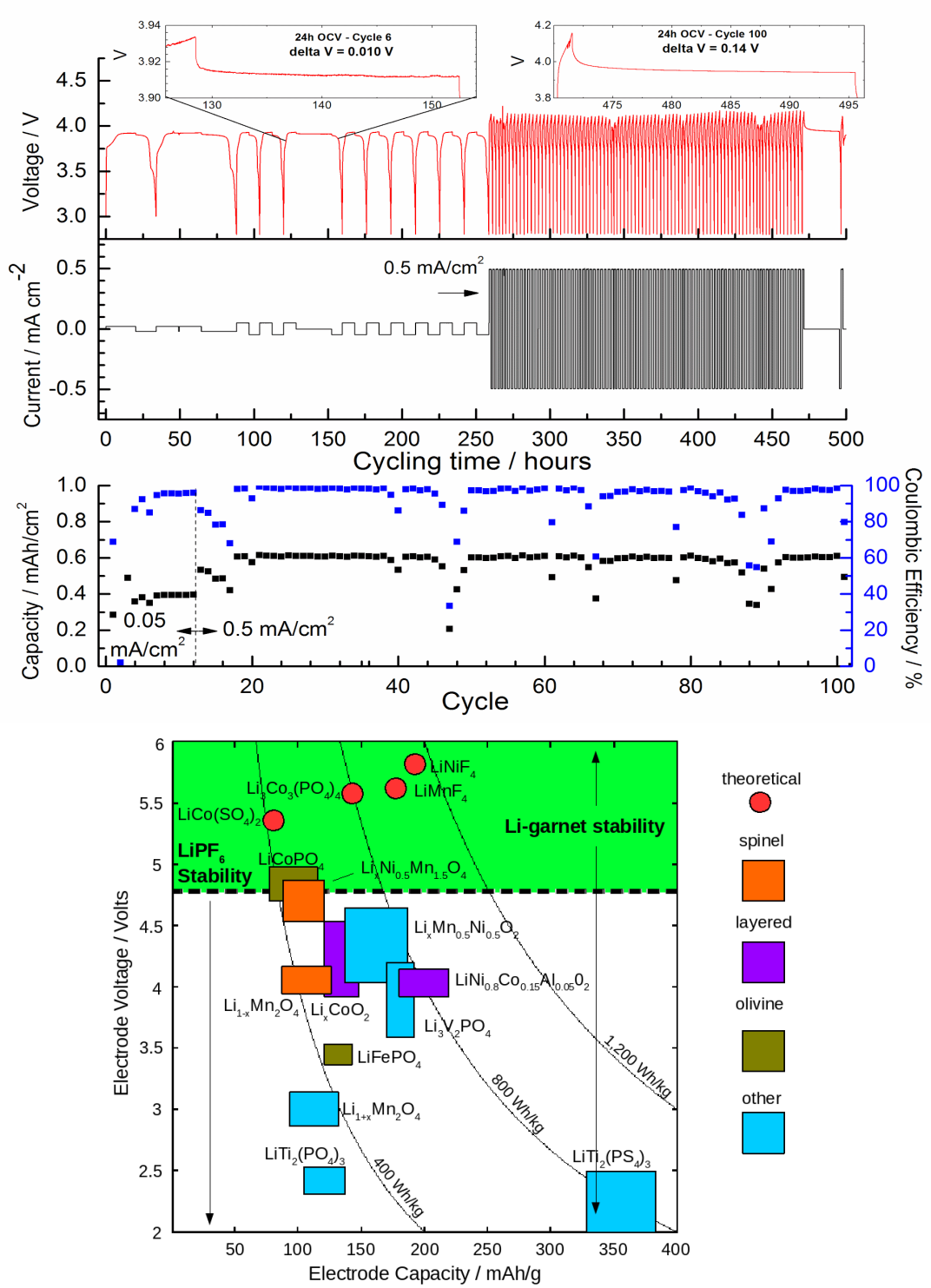

Figure 86. (a) Cycling of a lithium garnet cell with a lithium metal anode and $LiCoO_2$ cathode. (b) Capacity and voltage of a selection of existing and predicted cathodes compared to the voltage window of lithium garnet and $LiPF_6$ electrolytes. Cathodes are color coded based on phase by layered (purple), olivine (olive), spinel (orange) and other (blue). Predicted cathodes are shown in red circles.

Future work will focus on demonstration of the high energy density and cycle life capability of this technology. Using the high energy density cathodes available today, the authors predict these scale-ready scaffolds will support whole-cell energy densities beyond 300 Wh/kg and 1000 Wh/L ($LiNi_{0.8}Co_{0.15}Al_{0.05}O_2$ cathode) or 400 Wh/kg and 1000 Wh/l (sulfur cathode).

6.3 - Conclusions

LLCZN solid electrolytes are known to have an exceptionally wide electrochemical stability window, enabling the use of both high capacity lithium metal anode and high voltage cathode materials that are incompatible with today's standard liquid electrolytes. High impedance and poor electrode contact are major obstacles slowing the development of true all solid-state lithium batteries that promise to be the next leap in lithium battery technology. The fabrication of thin, LLCZN trilayer architectures is the first step in that leap. The porosity of the two supporting porous layers multiplies the contact area with the electrodes, making 100% of the electrode capacity accessible. The high density but exceptionally thin center layer creates a short conduction pathway for Li^+ cations, minimizing the contribution to the cell impedance. Critically, the dense center layer has proven to stop dendrite formation across the cell, allowing full cell batteries to last for hundreds of cycles with excellent capacity retention.

6.4 - Methodology

6.4.1 - Garnet Synthesis

$Li_{6.75}La_{2.75}Ca_{0.25}Zr_{1.5}Nb_{0.5}O_{12}$ was prepared in air by solid state reaction weighing stoichiometric amounts of La_2O_3 (GFS Chemicals, 99.9%), $CaCO_3$ (Carolina, Laboratory Grade), ZrO_2, (Inframat Advanced Materials), Nb_2O_5 (Alfa Aesar, 99.9%) and 10% excess anhydrous LiOH (Alfa Aesar, 98%). La_2O_3 was pretreated at 950°C for 12h; all other materials were used as-received. Raw materials were milled for 24 hours with 5 mm diameter yttria-stabilized zirconia (YSZ) grinding media in isopropanol then calcined at 900°C for 12 hours. Calcined powder was hand ground to pulverize large chunks, then milled in isopropanol for 3 days with 5 mm diameter YSZ grinding media followed by 8 days of milling in isopropanol with 2 mm diameter YSZ grinding media. The particle size of the resulting garnet powder was measured by a Horiba LA-950 laser particle size analyzer. Surface area of the garnet powder was measured by BET in a Micromeritics ASAP 2020. Phase characterization was performed using a Bruker D8 at University of Maryland's X-ray Crystallography Center for powder X-ray diffraction.

6.4.2 - Tapecasting

Garnet slurries for tape casting were prepared using isopropanol, toluene, fish oil, benzyl butyl phthalate, polyvinyl butyral, and the prepared LLCZN, with 10 or 15 μm cross-linked PMMA spheres and graphite used as porogens. Tapes were laminated at 80°C for 30 minutes to form multilayer structures. 1.6 cm diameter circles were punched from the laminated tapes for sintering.

6.4.3 - Trilayer garnet structure fabrication

Trilayer punch-outs were placed on a light layer of the mother powder on an alumina block. Mother powder was also placed on top of the trilayer punchouts. The punchouts were held flat by a porous alumina block. This assembly was placed into a tube furnace and heated in a flow of oxygen up to the sintering temperature, with holds at 250°C, 450°C, and 650°C to allow for binder burnout. Gas flow was stopped when the sintering temperature of 950°C was reached and the temperature was held for 5 hours before cooling, at which point gas flow was resumed.

6.4.4 - Cell assembly

Immediately after removal from the furnace, the sintered bodies were transferred to an argon environment, then taken to a Beneq TFS500 atomic layer deposition (ALD) chamber. In order to further improve lithium wetting and decrease interfacial impedance, Al_2O_3 of 5 nm thickness was deposited via ALD using trimethylaluminum and water as precursors at an operating temperature of 150°C. After ALD, an assembly of stainless steel current collectors, lithium metal and prepared garnet trilayer (Figure 87) was heated on a hot plate at 350°C in an argon glovebox (< 1.0 ppm H_2O, O_2) to impregnate lithium into the porous layers and create a symmetric cell. After cooling, this assembly was sealed in a 2032 button cell for testing outside the glovebox.

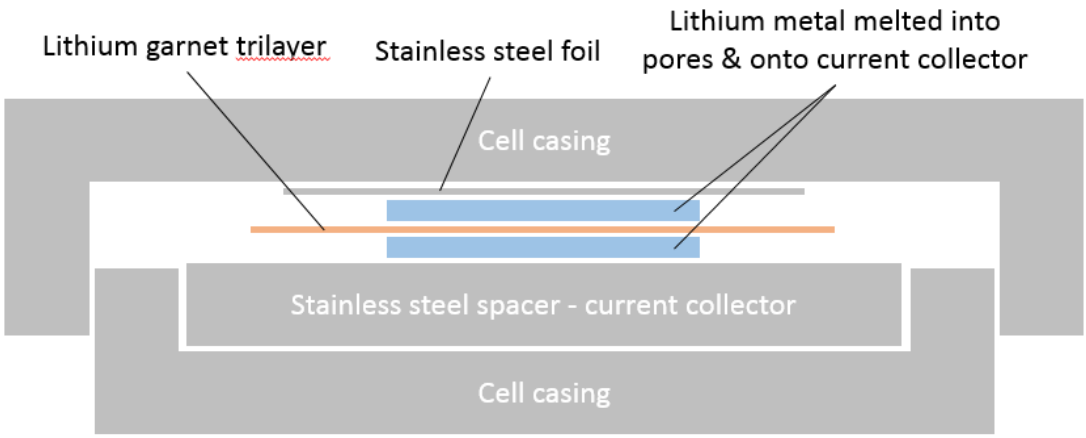

Figure 87. Diagram of lithium garnet trilayer assembled into symmetric cell in button cell case.

6.4.5 - Electrochemical Measurements

Electrochemical impedance spectroscopy (EIS) was performed from 10 MHz to 100 mHz with 5 mV amplitude between 0°C and 50°C using a Solartron 1260. Galvanostatic cycling was performed using an Arbin BT2043.

6.4.6 - Imaging

Electron microscopy was performed in the University of Maryland FabLab and AIMLab using a Hitachi S-3400 and a Hitachi SU-70. Image analysis was performed with ImageJ.

Chapter 7: Conclusion & Contribution to Field

The work in this dissertation began with funding from the U.S. Department of Energy Office of Electricity Delivery & Energy Reliability as a collaboration with Sandia National Laboratories to develop high conductivity NASICON-type electrolytes. This led to the development of new NASICON compositions including $Na_4ZrAlSi_2PO_{12}$ with a conductivity of 1.9x10-3 S/cm and later $Na_{3.4}Zr_{1.8}Zn_{0.2}Si_2PO_{12}$ with a conductivity of $3.75x10^{-3}$ S/cm.

Work with lithium garnets began with the one year visiting professorship of their inventor, Dr. Thangadurai. Together, we developed and studied new garnet compositions with higher lithium content than had previously been reported. This work, along with the battery design detailed in Chapter 4 set the basis for winning an ARPA-E seedling grant to for proof of principle of the technology.

With ARPA-E's support, we developed the procedures necessary to fabricate the trilayer garnet structure, leading to the assembly of batteries with the garnet structure as its electrolyte. This required investigation of a multitude of previously unknown factors in garnet synthesis and sintering. These discoveries led to more consistent garnet synthesis, tape casting, sintering, and sintered cell flatness. Once trilayers were ready, lithium cycling was demonstrated with low resistance in a symmetric lithium configuration. Batteries produced with garnet trilayers have lasted over 100 cycles with no fatigue and are ready for commercial development and scale up.

7.1 - Summary of Technological Contribution

Major technological developments in this dissertation were pursuant to the fabrication of a commercially viable solid state battery. Solid state Na^+ battery technology was advanced with the development of record conductivity NASICON. After refining the design for a lithium garnet-based solid state battery was a procedure for trilayer garnet fabrication was developed and patented. This became the essential component of our team's world first scalable, high rate solid state battery with high cathode loading.

7.2 - Summary of Scientific Contribution

The development of a high performance solid state battery required significant study of the underlying mechanisms behind lithium synthesis and sintering. Raman spectroscopy on super-lithiated garnet phases gave evidence to advance the understanding of the lower conductivity of low temperature garnet phases. Low-relative-humidity furnace reactions were discovered, as well as high temperature gas reactions which lead to increased lithium loss during sintering. Dilatometry was used to determine actual sintering temperature of lithium garnet sub-micron powder. Crumbling trilayers were resolved with better understanding of rheological properties of lithium garnet tape slurries.

7.3 - Future Direction of the Battery

This technology has won significant follow-on funding to develop further into a viable product. ARPA-E is supporting the spin out of this technology through Ion Storage Systems, LLC a company founded by our team. Further development currently ongoing is scaling up to larger format cells, implementation of scalable

ordered porosity to improve performance, further improvements to electrode infiltration, and working towards specific client application demands.

Appendix A: Peer Reviewed Publications and Patents

A.1 - First author publications

Hitz, G. T., Wachsman, E. D. & Thangadurai, V. Highly Li-Stuffed Garnet-Type $Li_{7+x}La_3Zr_{2-x}Y_xO_{12}$. *J. Electrochem. Soc.* **160,** A1248–A1255 (2013).

Hitz, G.T. *et al*. Scalable Fabrication of High-Power All Solid-State Lithium Batteries Using Unique Lithium Garnet Architecture. *To be Submitted.*

A.2 - Co-author publications

Lee, K. T. *et al.* Highly functional nano-scale stabilized bismuth oxides via reverse strike co-precipitation for solid oxide fuel cells. *J. Mater. Chem. A* **1,** 6199 (2013).

Zhu, H. et al. Free-standing $Na_{2/3}Fe_{1/2}Mn_{1/2}O_2$@Graphene film for a sodium-ion battery cathode. ACS Appl. Mater. Interfaces 6, 4242–4247 (2014).

Jolley, A. G., Cohn, G., Hitz, G. T. & Wachsman, E. D. Improving the ionic conductivity of NASICON through aliovalent cation substitution of $Na_3Zr_2Si_2PO_{12}$. *Ionics (Kiel).* **21,** 3031–3038 (2015).

Narayanan, S., Hitz, G. T., Wachsman, E. D. & Thangadurai, V. Effect of Excess Li on the Structural and Electrical Properties of Garnet-type $Li_6La_3Ta_{1.5}Y_{0.5}O_{12}$. **162,** 1772–1777 (2015).

A.3 - Patents & patent applications

Wachsman, E. D., Hitz, G. & Lee, K. T. Higher Conductivity NASICON Electrolyte for Room Temperature Solid-State Sodium Ion Batteries. (2014)

Hitz, G., McOwen, D. & Wachsman, E. D. Ceramic Ion Conducting Structures and Methods of Fabricating Same and Use of Same. (2015).

Appendix B - Building a temperature logging, environmentally controlled furnace

In the development of the fabrication procedure for sintered garnet trilayers, significant variation was seen from batch to batch. In order to control and track as many variables as possible, a Thermolyne 21100 tube furnace (Figure 88) was modified with gas caps automated controls for furnace temperature and multiple atmospheres. The temperature is recorded at two thermocouples, one inside the tube as close as possible to the sample and another thermocouple built into the furnace outside the tube. Near sintering the temperature, the furnace is controlled with the thermocouple near the sample. Gas is controlled via two solenoid valves leading to a rotameter (Figure 89). The system is controlled with an Arduino Nano connected to the computer via USB shown in Figure 90. The user controls the furnace with a purpose-written LabView program shown in Figure 91, choosing hold temperatures, stage atmospheres and ramp rates.

Figure 88. Photograph of modified Thermolyne 21100 furnace

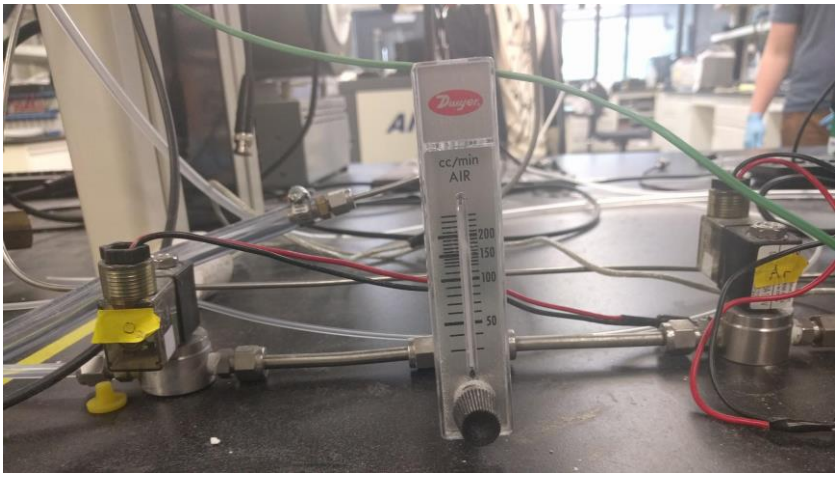

Figure 89. Photograph of solenoid valves and rotameter used for gas flow control

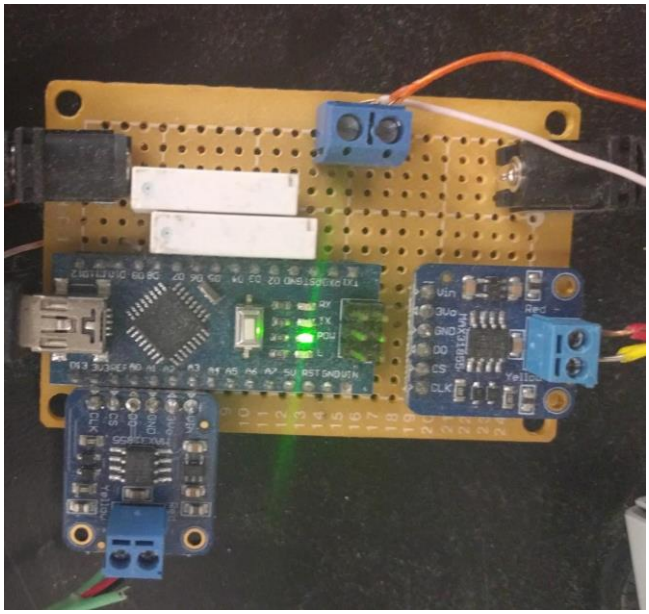

Figure 90. Photograph of Arduino Nano unit for reading thermocouples, controlling furnace temperature and controlling gas flow solenoids.

Figure 91. Screenshot of furnace controller software in LabView

Appendix C - MATLAB code for Analysis of 3D Grid Scans

```
padding = 0.1; %the padding around the cell in the graph
c_axis = [0 500]; %the colormap range in um
thickness = 80; %the thickness of the cell in um
highcut1 = 450; %the cutoff to remove artifactual spikes

%This imports the data file and removes the junk at the end. It
%also converts the z-height from mm to um

fileID = fopen('<file directory>/<filename>.x');
scanIn = textscan(fileID,'%f %f %f
        %s','Delimiter',';','TreatAsEmpty',',','HeaderLines',4);
fclose(fileID);
scanIn = cell2mat(scanIn(1,1:3)); %changes data format
found = find(isnan(scanIn),1); %finds the beginning of the junk data
scanIn = scanIn(1:found-3,:); %removes the junk data
scanIn(:,3) = scanIn(:,3)*1000; %converts z-height mm to um

bg = scanIn;
scan = scanIn;

%This calculates and graphs the background height of the sample
%holder. It automatically chooses a height cutoff that gets the best
%fitting.
lowcut = -140:10:200; %defines the z-height range in microns to test cutoff between
        data and background height.

for i  = 1:length(lowcut) %runs through the fitting for all cutoffs
   bg = scanIn(any(scanIn(:,3)<lowcut(i),2),:); %checks how many data points are in
        the background with the current cutoff
   if length(bg) > 0.1*length(scan) %checks if a reasonable number of points are in
        the background
      [sf, fitted(i)] = fit([bg(:,1),bg(:,2)],bg(:,3),'poly11'); %fits a surface to the data
      gof(i) = fitted(i).adjrsquare; %stores the goodness of fit
   end
end

[bestfit, bestfitindex] = max(gof); %finds the best fit and which cutoff gave that fit

bg = scanIn(any(scanIn(:,3)<lowcut(bestfitindex),2),:); %sets the background to the
        one with the best cutoff
[sf, check] = fit([bg(:,1),bg(:,2)],bg(:,3),'poly23'); %fits the data again with the best
        cutoff
```

```
figure
plot(sf,[bg(:,1),bg(:,2)],bg(:,3)) %plots the fitting - make sure to doublecheck this by
        eye
view([90 0]) %sets the starting viewing angle


scan(:,3) = scan(:,3)-feval(sf,scan(:,[1,2])); %subtracts the background z-height from
        the scan data
scan(~all([any(scan(:,3)>thickness,2), any(scan(:,3)<highcut1,2)],2),3) = NaN;
        %removes the z-height for any scan data that is background or artifact
%scan(:,3) = scan(:,3)-feval(sf,scan(:,[1,2])); %subtracts the background z-height
        from the scan data

rangetest = scan(~any(isnan(scan(:,3)),2),:); %makes a searchable array using only
        the trilayer data

xmin1 = min(rangetest(:,1)); %finds minimum x-value of trilayer
[xmax1, xmaxi1] = max(rangetest(:,1)); %finds maximum x-value of trilayer
ymin1 = min(rangetest(:,2));%finds minimum y-value of trilayer
[ymax1, ymaxi1] = max(rangetest(:,2));%finds maximum y-value of trilayer
zmin1 = min(scan(:,3));%finds minimum z-value of trilayer
[zmax1, peakrow] = max(scan(:,3));%finds maximum z-value of trilayer and its
        location

if xmax1-xmin1 > ymax1-ymin1 %finding the graphing range to use square axes
   diff1 = xmax1-xmin1;
else
   diff1 = ymax1-ymin1;
end

percent_variation1 = 100*((zmax1-thickness)/(thickness)-1); %calculating percent
        variation
stddev = std(scan(any(~isnan(scan(:,3)),2),3));
mymean = mean(scan(any(~isnan(scan(:,3)),2),3));

%isox = scan(any(scan(:,1)==2.15539e+02,2),1:3);

%linescan = figure;
%plot(isox(:,2)-isox(1,2),isox(:,3))
%axis equal
%xlabel('y-position / mm')
%ylabel('Z-height / um')
%title('Linescan at x=215.539 mm')

RSD = 100*stddev/mymean;
```

```
tri = delaunay(scan(:,1),scan(:,2)); %calculates a mesh of triangles from the xy data

figure1 = figure;
%set(figure1, 'Position', [100 100 800 800]) %makes the graph big so I can
        screenshot nicely

hold on
trisurf(tri,scan(:,1),scan(:,2),scan(:,3),'LineStyle','none') %graphs the trilayer scan
c = colorbar; %adds a colorbar
ylabel(c,'\fontsize{14}Height (um)') %labels the colorbar
xlabel('\fontsize{14}x (mm)') %labels the x axis
ylabel('\fontsize{14}y (mm)') %labels the y axis
%axis([xmin1-padding xmin1+diff1+padding ymin1-padding ymin1+diff1+padding
        c_axis(1) c_axis(2)]) %sets the range of the axes
caxis([c_axis(1) c_axis(2)]) %sets the range for the colorbar
colormap default;
axis equal
view([0 90]) %sets the view to be a top-down projection
text(xmin1,ymin1+0.2,zmax1,strcat('\bf RSD:  ',num2str(RSD,'%.0f'),'%'),
        'FontSize',12) %adds text to the plot giving the variation of the trilayer
text(xmin1+diff1-2.5,ymin1+0.2,zmax1,strcat('\bf High cutoff:
        ',num2str(highcut1,'%.0f'),' um'), 'FontSize',12) %adds text to the plot giving
        the variation of the trilayer
text(xmin1+diff1-2.5,ymin1+0.5,zmax1,strcat('\bf BG cutoff:
        ',num2str(lowcut(bestfitindex),'%.0f'),' um'), 'FontSize',12) %adds text to the
        plot giving the variation of the trilayer
text(xmin1,ymin1+0.8,zmax1,strcat('\bf StdDev:  ',num2str(stddev,'%.0f')),
        'FontSize',12) %adds text to the plot giving the standard deviation of the
        trilayer
text(scan(peakrow,1)+0.1,scan(peakrow,2)+0.1,scan(peakrow,3),strcat('\bf',num2str(z
        max1,'%.0f'),'um')) %adds text to the plot labelling the peak height
text(xmin1,ymin1+0.5,zmax1,strcat('\bf Thickness:  ',num2str(thickness,'%.0f'),' um'),
        'FontSize',12) %adds text to the plot giving the cell thickness
```

Appendix D - Challenges of TEM on Lithium Garnet

As interfacial resistance is a major concern for lithium garnets, a transmission electron microscopy (TEM) study was done to characterize the garnet surface immediately after sintering. LLCZN trilayers were fabricated using the same procedure developed in Chapter 5 and used in Chapter 6. These trilayers were mounted in cross section, epoxy filled, and polished to less than 100 um thick. This lamella was thinned to electron transparency in an argon ion mill for 30 hours, then immediately transferred to the TEM. It was intended to use electron energy loss spectroscopy (EELS) to characterize elemental composition and bonding states approaching the garnet surface. Selected area electron diffraction (SAED) was also planned in order to characterize the phase and lattice parameter of the near-surface garnet and any surface layers that may have been found.

Unfortunately, when the sample was exposed to the electron beam, it immediately began to change. Figure 92a shows a surface of the garnet in which a surface layer began to separate from the garnet within seconds, before a picture could be taken of the interface. Figure 92b is the same spot a few seconds later, after most of the surface layer was gone. It can be seen that there is a crystalline phase which is likely garnet. Unfortunately, Figure 92c shows that the garnet phase also decayed to an amorphous phase under the electron beam in under one minute. Figure 92d shows that this phase was so dramatic that the part of the sample under the electron beam actually twisted due to internal stresses. This was twisting visible in the live image and did not occur in the whole sample, but only the part in the direct path of the electron beam.

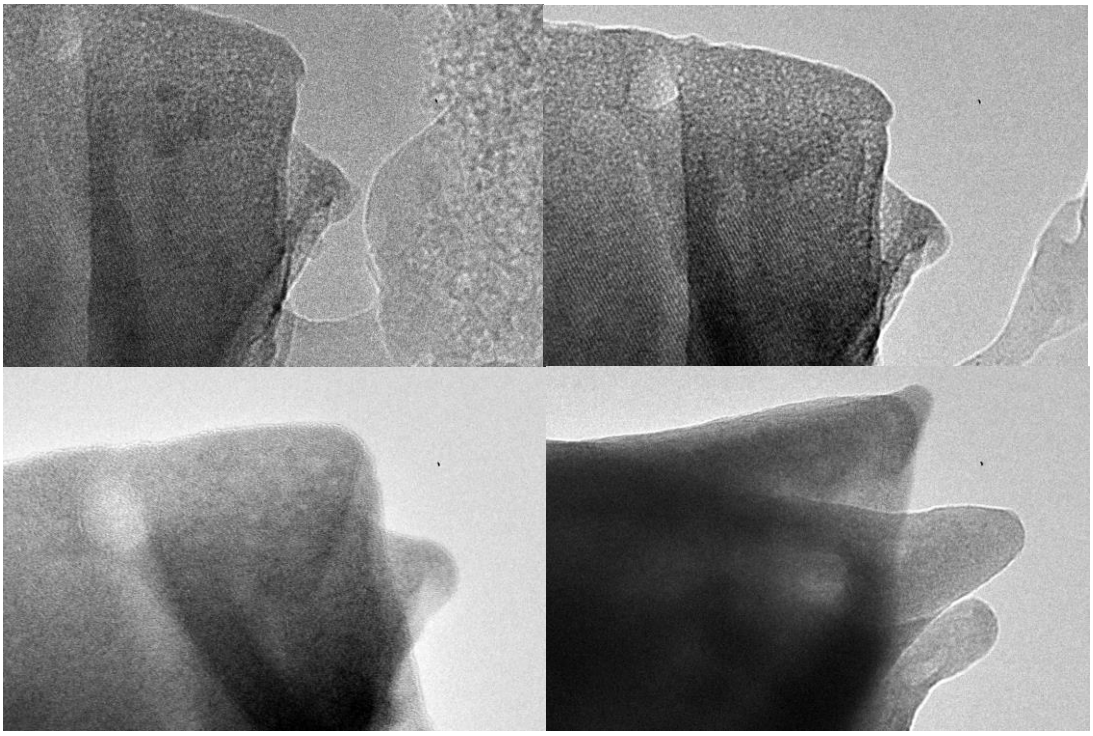

Figure 92. TEM images of LLCZN surface at time (a) ~5 seconds, (b) ~30 seconds, (c) ~1 minute, (d) ~2 minutes.

This rapid degradation ruled out the possibility of acquiring EELS or SAED data but some results were captured. Figure 93 shows a close-up and fast fourier transform of the near-surface garnet lattice fringes. The lattice spacing of the planes spacing indicates a lattice spacing of about 11 Å, which does not match any d-spacings ever observed in garnet in XRD. Normally reported lattice parameters for garnet are in the range of 12.9-13.1 Å, so this could be represent a significant contraction of the lattice near the garnet surface. However, due to the rapid changes due to the TEM beam, it is impossible to rule out that the electron beam did not affect the sample before measurement. More studies are would be required to corroborate this result.

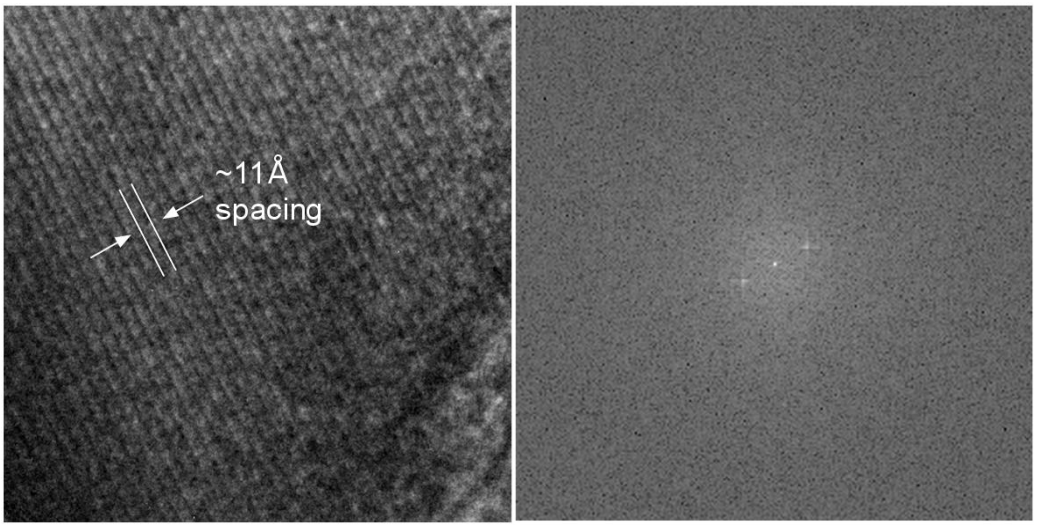

Figure 93. (a) TEM image showing lattice spacing observed in LLCZN sample and (b) fast fourier transform image of this fringe pattern.

Glossary

ALD - atomic layer deposition

EDS - Energy dispersive X-ray spectroscopy

EIS - Electrochemical impedance spectroscopy

LCO - $LiCoO_2$

LFMO - $Li_2FeMn_3O_8$

LLCZN - $Li_{(7-x+y)}La_{3-x}Ca_xZr_{2-y}Nb_yO_{12}$ - In reference to this document, x=0.25 and y=0.25 or 0.5 as noted in text.

LLZ - $Li_7La_3Zr_2O_{12}$

NCA - $LiNi_{0.8}Co_{0.15}Al_{0.05}O_2$

NMC - $LiNi_{0.33}Mn_{0.33}Co_{0.33}O_2$

PXRD - Powder X-ray diffraction

SEM - Scanning electron microscopy

TEM - Transmission electron microscopy

UMERC - University of Maryland Energy Research Center

XRD - X-ray diffraction - In reference to this document, XRD is always “powder X-ray diffraction” or PXRD

Bibliography

1. Block, D., Harrison, J. & Brooker, P. *Electric Vehicle Sales for 2014 and Future Projections*. (2014).
2. Koohi-Kamali, S., Tyagi, V. V., Rahim, N. A., Panwar, N. L. & Mokhlis, H. Emergence of energy storage technologies as the solution for reliable operation of smart power systems: A review. *Renew. Sustain. Energy Rev.* **25,** 135–165 (2013).
3. Chen, H. *et al.* Progress in electrical energy storage system: A critical review. *Prog. Nat. Sci.* **19,** 291–312 (2009).
4. Goodenough, J. B. & Kim, Y. Challenges for Rechargeable Li Batteries. *Chem. Mater.* **22,** 587–603 (2010).
5. Goodenough, J. B. Rechargeable batteries: challenges old and new. *J. Solid State Electrochem.* 2019–2029 (2012). doi:10.1007/s10008-012-1751-2
6. Tarascon, J.-M. M. J.-M. & Armand, M. Issues and challenges facing rechargeable lithium batteries. *Nature* **414,** 359–367 (2001).
7. Whittingham, M. S. History, Evolution, and Future Status of Energy Storage. *Proc. IEEE* **100,** 1518–1534 (2012).
8. Armand, M. & Tarascon, J.-M. Building better batteries. *Nature* **451,** 652–7 (2008).
9. Ciesla, J. Safety considerations for fabricating lithium battery packs. *J. Power Sources* **18,** 101–107 (1986).
10. Palomares, V. *et al.* Na-ion batteries, recent advances and present challenges to become low cost energy storage systems. *Energy Environ. Sci.* **5,** 5884 (2012).
11. Dunn, B., Kamath, H. & Tarascon, J.-M. Electrical energy storage for the grid: a battery of choices. *Science (80-.).* **334,** 928–35 (2011).
12. Strunk, G. Electrochemical Double Layered Capacitor Development and Implementation System. (2014). at <https://kuscholarworks.ku.edu/handle/1808/16831>
13. Aten, C., Michalowski, A., Williams, M., Stamm, C. & Evangelista, P. Soldier Power Operational Benefit Analysis. *Ind. Syst. Eng. Rev.* **3,** 82–90 (2015).
14. GRIDS Program Overview. 1–12 (2010). at <http://arpa-e.energy.gov/sites/default/files/documents/files/GRIDS_ProgramOverview.pdf >
15. Vitins, G. & West, K. Lithium intercalation into layered LiMnO2. *Electrochem. Soc. J.* **144,** 2587–2592 (1997).
16. Blyr, A. *et al.* Self-Discharge of LiMn2O4 / C Li-Ion Cells in Their Discharged State. *J. Electrochem. Soc.* **145,** 194–209 (1998).

17. Smart, M. & Ratnakumar, B. Irreversible Capacities of Graphite in Low • Temperature Electrolytes for Lithium • Ion Batteries. *J. Electrochem. Soc.* **146,** 3963–3969 (1999).

18. Park, Y. J. & Doeff, M. M. Effect of structure on the storage characteristics of manganese oxide electrode materials. *J. Power Sources* **165,** 573–580 (2007).

19. Mikhaylik, Y. V. & Akridge, J. R. Polysulfide Shuttle Study in the Li/S Battery System. *J. Electrochem. Soc.* **151,** A1969 (2004).

20. Julien, C. Technological applications of solid state ionics. *Mater. Sci. Eng. B* **5,** 9–28 (1990).

21. Murugan, R., Thangadurai, V. & Weppner, W. Fast lithium ion conduction in garnet-type Li7La3Zr2O12. *Angew. Chem. Int. Ed. Engl.* **46,** 7778–81 (2007).

22. Oudenhoven, J. F. M., Baggetto, L. & Notten, P. H. L. All-Solid-State Lithium-Ion Microbatteries: A Review of Various Three-Dimensional Concepts. *Adv. Energy Mater.* **1,** 10–33 (2011).

23. Thangadurai, V. & Weppner, W. Li6ALa2Ta2O12 (A = Sr, Ba): Novel Garnet-Like Oxides for Fast Lithium Ion Conduction. *Adv. Funct. Mater.* **15,** 107–112 (2005).

24. Thangadurai, V., Kaack, H. & Weppner, W. J. F. Novel Fast Lithium Ion Conduction in Garnet-Type Li5La3M2O12 (M= Nb, Ta). *J. Am. Ceram. Soc.* **86,** 437–440 (2003).

25. Thangadurai, V., Narayanan, S. & Pinzaru, D. Garnet-type solid-state fast Li ion conductors for Li batteries: critical review. *Chem. Soc. Rev.* (2014). doi:10.1039/c4cs00020j

26. Momma, K. & Izumi, F. VESTA 3 for three-dimensional visualization of crystal, volumetric and morphology data. *J. Appl. Crystallogr.* **44,** 1272–1276 (2011).

27. Geiger, C. a *et al.* Crystal chemistry and stability of 'Li7La3Zr2O12' garnet: a fast lithium-ion conductor. *Inorg. Chem.* **50,** 1089–97 (2011).

28. Tietz, F., Wegener, T., Gerhards, M. T., Giarola, M. & Mariotto, G. Synthesis and Raman micro-spectroscopy investigation of Li7La3Zr2O12. *Solid State Ionics* **230,** 77–82 (2013).

29. Buschmann, H. *et al.* Structure and dynamics of the fast lithium ion conductor 'Li7La3Zr2O12'. *Phys. Chem. Chem. Phys.* **13,** 19378–92 (2011).

30. Li, Y., Han, J.-T., Wang, C.-A., Xie, H. & Goodenough, J. B. Optimizing Li+ conductivity in a garnet framework. *J. Mater. Chem.* **22,** 15357 (2012).

31. METALPRICES.COM: An Argus Media service. at <www.metalprices.com>

32. Nelson, P. a., Gallagher, K. G., Bloom, I. & Dees, D. W. *Modeling the Performance and Cost of Lithium-Ion Batteries for Electric-Drive Vehicles Chemical Sciences and Engineering Division*. (2011).

33. Ong, S. P. *et al.* Voltage, stability and diffusion barrier differences between

sodium-ion and lithium-ion intercalation materials. *Energy Environ. Sci.* 3680–3688 (2011). doi:10.1039/c1ee01782a

34. Fergus, J. W. Ion transport in sodium ion conducting solid electrolytes. *Solid State Ionics* **227,** 102–112 (2012).

35. Goodenough, J. B. & Hong, H. Y. P. Fast Na+-ion transport in skeleton structures. *Mater. Res. Bull.* **I,** 203–220 (1976).

36. Hong, H. Y. P. Crystal structures and crystal chemistry in the system Na1+ xZr2SixP3-xO12. *Mater. Res. Bull.* **I,** 173–182 (1976).

37. Colomban, P. & Mouchon, E. Phase transition in, thermal history and expansion of NASICON, solid solution and lithium derivative ceramics and of SiC (mullite) fibers-NASICON composites. *Solid state ionics* **73,** 209–220 (1994).

38. Von Alpen, U., Bell, M. & Wichelhaus, W. Phase transition in nasicon (Na3Zr2Si2PO12). *Mater. Res. Bull.* **14,** 1317–1322 (1979).

39. Shimazu, K., Yamamoto, Y., Saito, Y. & Nakamura, O. Electrical conductivity and Ti 4+ ion substitution range in NASICON system. *Solid state ionics* **79,** 106–110 (1995).

40. Vogel, E., Cava, R. & Rietman, E. Na+ ion conductivity and crystallographic cell characterization in the Hf-nasicon system Na1+ xHf2SixP3-xO12. *Solid state ionics* **14,** 1–6 (1984).

41. Fuentes, R. O., Figueiredo, F., Marques, F. & Franco, J. Influence of microstructure on the electrical properties of NASICON materials. *Solid State Ionics* **140,** 173–179 (2001).

42. Miyajima, Y., Saito, Y., Matsuoka, M. & Yamamoto, Y. Ionic conductivity of NASICON-type Na< sub> 1+ x</sub> M< sub> x</sub> Zr< sub> 2− x</sub> P< sub> 3</sub> O< sub> 12</sub>(M: Yb, Er, Dy). *Solid State Ionics* **84,** 61–64 (1996).

43. Verissimo, C. *et al.* Ionic conductivity and structural characterization of Na1. 5Nb0. 3Zr1. 5 (PO4) 3 with NASICON-type structure. *Solid state ionics* **100,** 127–134 (1997).

44. Takahashi, T., Kuwabara, K. & Shibata, M. Solid-state ionics-conductivities of Na+ ion conductors based on NASICON. *Solid State Ionics* **1,** 163–175 (1980).

45. Saito, Y., Ado, K., Asai, T., Kageyama, H. & Nakamura, O. Ionic conductivity of NASICON-type conductors Na1.5M0.5Zr1.5(PO4)3 (M: Al 3+, Ga 3+, Cr 3+, Sc 3+, Fe 3+, In 3+, In 3+, Yb 3+, Y 3+). *Solid state ionics* **58,** 327–331 (1992).

46. Rangan, K. K. NASICON-Type Vanadium Phosphate Synthesized by Oxidative. *Society* **4,** 1991–1993 (1992).

47. Zatovsky, I. V. NASICON-type Na(3)V(2)(PO(4))(3). *Acta Crystallogr. Sect. E. Struct. Rep. Online* **66,** i12 (2010).

48. Okada, S., Noguchi, Y., Kobayashi, E. & Yamaki, J. All-Solid-State Sodium-

ion Symmetric Battery with NASICON-type Compounds. in **2,** 2010 (ECS, 2010).

49. Cheng, L. *et al.* The origin of high electrolyte-electrode interfacial resistances in lithium cells containing garnet type solid electrolytes. *Phys. Chem. Chem. Phys.* **16,** 18294–18300 (2014).

50. Han, X. *et al.* Negating Interfacial Impedance in Garnet-Based Solid-State Li-Metal Batteries. *Nat. Mater.*

51. Sudo, R. *et al.* Interface behavior between garnet-type lithium-conducting solid electrolyte and lithium metal. *Solid State Ionics* **262,** 151–154 (2014).

52. Buschmann, H., Berendts, S., Mogwitz, B. & Janek, J. Lithium metal electrode kinetics and ionic conductivity of the solid lithium ion conductors '$Li_7La_3Zr_2O_{12}$' and $Li_{7-x}La_3Zr_{2-x}Ta_xO_{12}$ with garnet-type structur. *J. Power Sources* **206,** 236–244 (2012).

53. Sharafi, A., Meyer, H. M., Nanda, J., Wolfenstine, J. & Sakamoto, J. Characterizing the Li-Li7La3Zr2O12 interface stability and kinetics as a function of temperature and current density. *J. Power Sources* **302,** 135–139 (2016).

54. Yabuuchi, N. *et al.* P2-type Nax[Fe1/2Mn1/2]O2 made from earth-abundant elements for rechargeable Na batteries. *Nat. Mater.* **11,** 1–6 (2012).

55. Arora, P., White, R. & Doyle, M. Capacity Fade Mechanisms and Side Reactions in Lithium Ion Batteries. *J. Electrochem. Soc.* **145,** 3647–3667 (1998).

56. Shin, Y. & Manthiram, a. Influence of the Lattice Parameter Difference between the Two Cubic Phases Formed in the 4 V Region on the Capacity Fading of Spinel Manganese Oxides. *Chem. Mater.* **15,** 2954–2961 (2003).

57. Xu, K. Nonaqueous liquid electrolytes for lithium-based rechargeable batteries. *Chem. Rev.* **104,** 4303–417 (2004).

58. Wang, Q., Sun, J., Yao, X. & Chen, C. 4-Isopropyl Phenyl Diphenyl Phosphate as Flame-Retardant Additive for Lithium-Ion Battery Electrolyte. *Electrochem. Solid-State Lett.* **8,** A467 (2005).

59. Hyung, Y. E., Vissers, D. R. & Amine, K. Flame-retardant additives for lithium-ion batteries. *J. Power Sources* **119-121,** 383–387 (2003).

60. Xiang, H. F., Xu, H. Y., Wang, Z. Z. & Chen, C. H. Dimethyl methylphosphonate (DMMP) as an efficient flame retardant additive for the lithium-ion battery electrolytes. *J. Power Sources* **173,** 562–564 (2007).

61. Noguchi, Y., Kobayashi, E., Plashnitsa, L. S., Okada, S. & Yamaki, J. Fabrication and performances of all solid-state symmetric sodium battery based on NASICON-related compounds. *Electrochim. Acta* **101,** 59–65 (2013).

62. Notten, P. H. L., Roozeboom, F., Niessen, R. a. H. & Baggetto, L. 3-D Integrated All-Solid-State Rechargeable Batteries. *Adv. Mater.* **19,** 4564–4567 (2007).

63. Hayashi, A., Noi, K., Sakuda, A. & Tatsumisago, M. Superionic glass-ceramic electrolytes for room-temperature rechargeable sodium batteries. *Nat. Commun.* **3,** 856 (2012).

64. Bates, J., Lubben, D., Dudney, N. & Hart, F. 5 Volt Plateau in LiMn2O4 Thin Films. *J. Electrochem. Soc.* **142,** 4–6 (1995).

65. Plichta, E. J. & Behl, W. K. A low-temperature electrolyte for lithium and lithium-ion batteries. *J. Power Sources* **88,** 192–196 (2000).

66. Cvjeticanin, N. & Mentus, S. Conductivity, viscosity and IR spectra of Li, Na and Mg perchlorate solutions in propylene carbonate/water mixed solvents. *Phys. Chem. Chem. Phys.* **1,** 5157–5161 (1999).

67. Shimizu, Y., Azuma, Y. & Michishita, S. Sol – gel synthesis of NASICON discs from aqueous solution. **7,** 1487–1490 (1997).

68. Perthuis, H. & Colomban, P. Well densified NASICON type ceramics, elaborated using sol-gel process and sintering at low temperatures. *Mater. Res. Bull.* **19,** 621–631 (1984).

69. Lloyd, I. K., Gupta, T. K. & Hall, B. O. Sintering and characterization of alkaline-earth doped and zirconium-deficient Na3Zr2Si2PO12. *Solid State Ionics* **11,** 39–44 (1983).

70. Miyajima, Y. *et al.* Solubility range and ionic conductivity of large trivalent ion doped. *Solid State Ionics* **124,** 201–211 (1999).

71. Feltz, A. & Barth, S. Preparation and conductivity behaviour of Na3MIIZr(PO4)3, (MII: Mn,Mg,Zn). *Solid State Ionics* **10,** 817–821 (1983).

72. Feist, T., Davies, P. K. & Vogel, E. The energetics of phase transitions in the system Na1+ XZr2SiXP3-XO12, 1.9 < X < 2.5. *Thermochim. Acta* **106,** 57–61 (1986).

73. Bukun, N. Superionic transitions in NASICON-type solid electrolytes. *Ionics (Kiel).* **2,** 63–68 (1996).

74. Von Alpen, U., Bell, M. & Hofer, H. Compositional dependence of the electrochemical and structural parameters in the NASICON system (Na1+ xSixZr2P3-xO12). *Solid State Ionics* **3,** 215–218 (1981).

75. Gasmi, N. *et al.* Comparison of different synthesis methods for Nasicon ceramics. *J. Sol-Gel Sci. Technol.* **4,** 231–237 (1995).

76. Wang, B., Chen, S. C. & Greenblatt, M. The Crystal Structure and Ionic Conductivity of the Ilmenite Polymorph of NaSbO3. *J. Solid State Chem.* **108,** 184–188 (1994).

77. Mazza, D. Modeling Ionic Conductivity in Nasicon Structures. *J. Solid State Chem.* **156,** 154–160 (2001).

78. Kamaya, N. *et al.* A lithium superionic conductor. *Nat. Mater.* **10,** 682–686 (2011).

79. Lu, X., Xia, G. & Lemmon, J. P. Advanced materials for sodium-beta alumina

batteries: Status, challenges and perspectives. *J. Power Sources* **195,** 2431–2442 (2010).

80. Fuentes, R. O., Marques, F. & Franco, J. Synthesis and Properties of NASICON prepared from Different Zirconia-based Precursors. *BOLETIN-SOCIEDAD Esp. Ceram. Y Vidr.* **38,** 631–634 (1999).

81. Fuentes, R. O., Figueiredo, F., Marques, F. M. B. & Franco, J. Processing and electrical properties of NASICON prepared from yttria-doped zirconia precursors. *J. Eur. Ceram. Soc.* **21,** 737–743 (2001).

82. Zhang, S. *et al.* Preparation and characterization of NASICON with a new sol–gel process. *Mater. Lett.* **58,** 226–229 (2004).

83. Ahmad, A., Wheat, T., Kuriakose, A., Canaday, J. & McDonald, A. Dependence of the properties of Nasicons on their composition and processing. *Solid State Ionics* **24,** 89–97 (1987).

84. Robertson, A. & West, A. Review of crystalline lithium-ion conductors suitable for high temperature battery applications. *Solid State Ionics* **104,** 1–11 (1997).

85. Knauth, P. Inorganic solid Li ion conductors: An overview. *Solid State Ionics* **180,** 911–916 (2009).

86. Park, M., Zhang, X., Chung, M., Less, G. B. & Sastry, A. M. A review of conduction phenomena in Li-ion batteries. *J. Power Sources* **195,** 7904–7929 (2010).

87. Yang, M. & Hou, J. Membranes in lithium ion batteries. *Membranes (Basel).* **2,** 367–83 (2012).

88. Adachi, G., Imanaka, N. & Aono, H. Fast Li⊕ Conducting Ceramic Electrolytes. *Adv. Mater.* **8,** 127–135 (1996).

89. Stramare, S., Thangadurai, V. & Weppner, W. Lithium Lanthanum Titanates: A Review. *Chem. Mater.* **15,** 3974–3990 (2003).

90. Inaguma, Y., Liquan, C., Itoh, M. & Nakamura, T. High Ionic Conductivity in Lithium Lanthanum Titanate. *Solid State Commun.* **86,** 689–693 (1993).

91. Thangadurai, V. & Weppner, W. Li6ALa2Nb2O12 (A=Ca, Sr, Ba): A New Class of Fast Lithium Ion Conductors with Garnet-Like Structure. *J. Am. Ceram. Soc.* **88,** 411–418 (2005).

92. Awaka, J., Kijima, N., Hayakawa, H. & Akimoto, J. Synthesis and structure analysis of tetragonal Li7La3Zr2O12 with the garnet-related type structure. *J. Solid State Chem.* **182,** 2046–2052 (2009).

93. Rangasamy, E., Wolfenstine, J. & Sakamoto, J. The role of Al and Li concentration on the formation of cubic garnet solid electrolyte of nominal composition Li7La3Zr2O12. *Solid State Ionics* **206,** 28–32 (2012).

94. Han, J. *et al.* Experimental visualization of lithium conduction pathways in garnet-type Li7La3Zr2O12. *Chem. Commun. (Camb).* **48,** 9840–2 (2012).

95. Callaghan, M. P. O., Powell, A. S., Titman, J. J., Chen, G. Z. & Cussen, E. J. Switching on Fast Lithium Ion Conductivity in Garnets : The Structure and Transport Properties of Li 3 + x Nd 3 Te 2-x Sb x O 12. *Society* **15,** 2360–2369 (2008).

96. Kokal, I., Somer, M., Notten, P. & Hintzen, H. Sol–gel synthesis and lithium ion conductivity of Li7La3Zr2O12 with garnet-related type structure. *Solid State Ionics* **185,** 42–46 (2011).

97. Shannon, R. D. Revised effective ionic radii and systematic studies of interatomic distances in halides and chalcogenides. *Acta Crystallogr. Sect. A* **32,** 751–767 (1976).

98. Łasocha, W. & Lewinski, K. PROSZKI – a system of programs for powder diffraction data analysis. *J. Appl. Crystallogr.* **27,** 437–438 (1994).

99. Xie, H., Li, Y. & Goodenough, J. B. Low-temperature synthesis of Li7La3Zr2O12 with cubic garnet-type structure. *Mater. Res. Bull.* **47,** 1229–1232 (2012).

100. Wolfenstine, J., Rangasamy, E., Allen, J. L. & Sakamoto, J. High conductivity of dense tetragonal Li7La3Zr2O12. *J. Power Sources* **208,** 193–196 (2012).

101. Il'ina, E. a., Andreev, O. L., Antonov, B. D. & Batalov, N. N. Morphology and transport properties of the solid electrolyte Li7La3Zr2O12 prepared by the solid-state and citrate–nitrate methods. *J. Power Sources* **201,** 169–173 (2012).

102. Boyapati, S., Wachsman, E. D. & Jiang, N. Effect of oxygen sublattice ordering on interstitial transport mechanism and conductivity activation energies in phase-stabilized cubic bismuth oxides. *Solid State Ionics* **140,** 149–160 (2001).

103. Cussen, E. J. Structure and ionic conductivity in lithium garnets. *J. Mater. Chem.* **20,** 5167 (2010).

104. Taek Lee, K., Yoon, H. S., Ahn, J. S. & Wachsman, E. D. Bimodally integrated anode functional layer for lower temperature solid oxide fuel cells. *J. Mater. Chem.* **22,** 17113 (2012).

105. Lee, K. T., Vito, N. J., Yoon, H. S. & Wachsman, E. D. Effect of Ni-Gd0.1Ce0.9O1.95 Anode Functional Layer Composition on Performance of Lower Temperature SOFCs. *J. Electrochem. Soc.* **159,** F187–F193 (2012).

106. Lee, K. T. *et al.* Interfacial modification of La0.80Sr0.20MnO3−δ–Er0.4Bi0.6O3 cathodes for high performance lower temperature solid oxide fuel cells. *J. Power Sources* **220,** 324–330 (2012).

107. Lee, K. T., Vito, N. J. & Wachsman, E. D. Comprehensive quantification of Ni-Gd0.1Ce0.9O 1.95 anode functional layer microstructures by three-dimensional reconstruction using a FIB/SEM dual beam system. *J. Power Sources* **228,** 220–228 (2013).

108. Thangadurai, V. & Weppner, W. Effect of sintering on the ionic conductivity of garnet-related structure Li5La3Nb2O12 and In- and K-doped

Li5La3Nb2O12. *J. Solid State Chem.* **179,** 974–984 (2006).

109. Hitz, G. T., Wachsman, E. D. & Thangadurai, V. Highly Li-Stuffed Garnet-Type Li7+xLa3Zr2-xYxO12. *J. Electrochem. Soc.* **160,** A1248–A1255 (2013).

110. Rane, G. K., Welzel, U., Meka, S. R. & Mittemeijer, E. J. Non-monotonic lattice parameter variation with crystallite size in nanocrystalline solids. *Acta Mater.* **61,** 4524–4533 (2013).

111. Banerjee, A., Gupta, R. & Balani, K. Non-monotonic lattice parameter variation in ball-milled ceria. *J. Mater. Sci.* **50,** 6349–6358 (2015).

112. Edström, K., Gustafsson, T. & Thomas, J. O. The cathode–electrolyte interface in the Li-ion battery. *Electrochim. Acta* **50,** 397–403 (2004).

113. Kumazaki, S. *et al.* Electrochemistry Communications High lithium ion conductive Li 7 La 3 Zr 2 O 12 by inclusion of both Al and Si. *Electrochem. commun.* **13,** 509–512 (2011).

114. Ohta, S., Kobayashi, T. & Asaoka, T. High lithium ionic conductivity in the garnet-type oxide Li7−X La3(Zr2−X, NbX)O12 (X=0–2). *J. Power Sources* **196,** 3342–3345 (2011).

115. Muenzel, V. *et al.* A Comparative Testing Study of Commercial 18650-Format Lithium-Ion Battery Cells. *J. Electrochem. Soc.* **162,** A1592–A1600 (2015).

116. Peng, H., Wu, Q. & Xiao, L. Low temperature synthesis of Li5La3Nb2O12 with cubic garnet-type structure by sol–gel process. *J. Sol-Gel Sci. Technol.* **66,** 175–179 (2013).

117. Tadanaga, K. *et al.* Low temperature synthesis of highly ion conductive Li7La3Zr2O12–Li3BO3 composites. *Electrochem. commun.* **33,** 51–54 (2013).

118. Takano, R., Tadanaga, K., Hayashi, A. & Tatsumisago, M. Low temperature synthesis of Al-doped Li7La3Zr2O12 solid electrolyte by a sol–gel process. *Solid State Ionics* **255,** 104–107 (2014).